CENTRO DE INVESTIGACIONES
EN OPTICA, A.C.

Study of the photoconversion efficiency on nanostructured solar cells based on TiO$_2$ films sensitized with QDs and decorated with Au nanoparticles and P3OT

Thesis in partial fulfillment of the requirements for the degree of

Doctor in Sciences (Optics)

by

M. Sc. Isaac Zarazúa Macías

Advisor: Dr. Elder de la Rosa Cruz

León Gto., México   December 2013

Agradecimientos:

Dedicada a: Al amor de mi vida, quien me mantiene cuerdo en esta locura que es la vida

Agradecimientos:

Quiero agradecer profundamente a:

Mis padres, a quienes debo mas que la vida, y me han apoyado en cada paso de mi vida.

A Oscar García, Rosario Miranda, Emilia Bolio y Alfredo Aranda quienes representan a todos aquellos profesores que a lo largo de mi vida académica me han guiado no solo con sus conocimientos, sino con su sabiduría y afecto.

A el Profesor Jesús Mancilla y a la Maestra Ángeles Trujillo quienes al enseñarme el amor por las artes marciales y la música se han vuelto una parte fundamental de mi formación como persona ya que me dieron toda una filosofía de vida, basada en disciplina, perseverancia y lo más importante un gran amor a lo que uno hace tomando en cuenta que en la vida hay mas cosas que solo el estudio.

Agradezco al Dr. Juan Reyes Gómez quien ha sido a la vez profesor, colega y amigo sin el cual este trabajo no hubiera sido posible.

A todos ustedes les agradezco desde lo más profundo de mi corazón ya que sin ustedes yo no seria quien soy ni habría llegado hasta este punto de mi vida.

Abstract

Novel composite titanium dioxide (TiO_2) films of 10 μm thickness have been prepared and characterized with emphasis on evaluating their photovoltaic properties. The films contain TiO_2 nanocrystals (NCs) with anatase crystalline phase deposited on a substrate with a thin conductor oxide film, composited with CdSe quantum dots (QDs), Au nanoparticles (NPs), and poly(3-octylthiophene) (P3OT) in different configurations. In the case of single sensitized films, Au NPs considerably increases the FF of titania films, indicating that such NPs help to the charge carriers transport. P3OT slightly increases the photocurrent and FF of the TiO_2 films, indicating that the polymer may acts as a photogenerator and as a hole conductor giving a relatively good cell performance. However, CdSe QDs sensitized films exhibited the largest photocurrent (237 μA/cm2) giving a photo-conversion efficiency of 0.149%, overcoming the efficiency of the other two materials and giving a four-fold efficiency increase of not sensitized TiO_2 (0.034%). These results are attributed to the ability of QDs to photogenerate charge carriers efficiently giving a great amount of electrons to increase the photocurrent. With the introduction of Au NPs or P3OT into the TiO_2/QDs films, the photocurrent increases up to ~85% and ~150% while the photoconversion efficiency increases by ~167% and ~177%, respectively. An interesting synergistic effect was observed when Au NPs and P3OT were used in conjunction. The configuration of TiO_2/Au/QDs/P3OT film exhibits a photocurrent of 906 μA (an enhancement of ~285%) and the photoconversion efficiency of 0.661% (an enhancement of ~600%) compared to that of TiO_2/QDs films. Such significant enhancement is attributed to the ability of Au NPs to facilitate charge separation and improve electron injection as well as P3OT's ability to inject electrons and enhance hole transport avoiding electron recombination. Such ability when combined with the QD's strong photoabsorption in the visible, lead to the overall increase in photocurrent generation, fill factor, and consequently photoconversion efficiency.

Resumen

Se elaboraron y caracterizaron películas de 10 µm de espesor basadas compuestos novedosos en dióxido de titanio (TiO$_2$), enfocándose particularmente en estudiar y optimizar sus propiedades fotovoltaicas. Las películas se componen de Nanocristales de TiO$_2$ en fase cristalina anataza, depositados sobre substratos de oxido conductor transparente, acomplejados con Puntos cuánticos de seleniuro de cadmio (CdSe QDs), nanoparticulas de oro (Au NPs) y poli 3 octil tiofeno (P3OT) en distintas configuraciones. Al analizar películas sensibilizadas con solo uno de estos materiales, se encontró que las NPs de Au incrementaban considerablemente el Factor de llenado (FF) de las películas de titania, indicando que estas nanopartículas ayudan con el transporte de carga; por otra parte, el P3OT incrementa ligeramente la fotocorriente y el factor de llenado de las películas te TiO$_2$, indicando que este polímero puede trabajar como fotogenerador y como conductor de huecos, dando un relativamente buen desempeño como celda solar; sin embargo, las películas sensibilizadas con QDs de CdSe mostraron la mayor fotocorriente de estas tres celdas (237 µA/cm2), resultando en una eficiencia de 0.149%, superando la eficiencia de los otros dos compuestos y cuadruplicando la eficiencia de el TiO$_2$ sin sensibilizar (0.034%). Este resultado se atribuyó a la gran capacidad de los QDs de fotogenrear portadores de carga, resultando en una gran cantidad de electrones que incrementaron la fotocorriente. Al combinar estos sensibilizantes se encontró que con la adición de NPs de Au o P3OT a las películas de TiO$_2$/QDs la corriente incrementa en un 85% y 150%, mientras que la eficiencia de fotoconverisión incrementa en un 167 y 177 % respectivamente. Se encontró un efecto sinergético interesante al usar los tres compuestos en conjunto. Las películas con la configuración TiO$_2$/Au/QDs/P3OT presentaron una fotocorriente de 906µA (lo que representa un incremento del 285%) y una eficiencia de fotoconverison de 0.661% (un incremento del 600% en comparación con las películas de TiO$_2$/QDs). Este incremento fue atribuido a la habilidad de las NPs de Au para facilitar la separración de portadores de carga mejorando así el transporte de electrones, y la habilidad del P3OT para generar

electrones, facilitar el transporte de huecos y al mismo tiempo evitar las recombinaciones de electrones. Estas habilidades combinadas con la fuerte fotoabsorcion de los QDs resulta en un incremento general en la fotocorriente y el factor de llenado consecuentemente la eficiencia de fotoconversión.

Preface

In the last decade the global energy demand has increased exponentially, at the same time the principal energy source in the planet (oil) is starting to decline. For this reason in recent years the search and development for new clean energy sources have become a very important topic. The present work exposes a series of systematic studies done with novel materials for solar cells and photovoltaic devices, describing from the synthesis of the materials to the characterization techniques, the modeling and the physical interpretation of the measurements. During this research new architectures and models were proposed that resulted in very promising steps in the way to develop cheaper and more efficient solar cells and photovoltaic devices.

This thesis is divided into 7 chapters. Chapter 1 describes the environmental situation that motivates the interesting study of new alternatives for solar cells. It also describes the physical mechanism involved in the photovoltaic energy generation and the principal parameters that evaluate the performance of a solar cell. Finally, the characteristics of some types of nanostructured solar cells are described as well as interesting approaches recently studied to improve the efficiency in solar cells.

Chapter 2 describes a comparative study of the photovoltaic properties of TiO_2 films sensitized with 3 different materials, Gold Nanoparticles (Au NPs), CdSe quantum dots(QDs) and Poly-(3Octil-thiopene) (P3OT). Thedescription ranges from the structural and optical characterization of the basic components of sensitized films to the assembling and electrochemical characterization of devices. The origin of the photocurrent in each device is explained to understand the principal strengths and weakness of each material.

Chapter 3 describes a series of experiments where TiO_2 films were sensitized

with CdSe QDs and simultaneously decorated with Au NPs and P3OT in different configurations with the main purpose of combining the strengths of each material to overcome their weaknesses. In the experimental section of the chapter, it is demonstrated that the right order of material deposition (TiO$_2$/Au/QDs/P3OT) makes possible to increase 6 times the photoconvercion efficiency. The chapter contains a discussion of the physical process of photogeneration and charge carriers transport for each configuration, and how they are corroborated by the experimental results. Such results provide a better understanding of the role of each component to improve the efficiency of the devices under study.

Chapter 4 explains the Electrochemical Impedance Spectroscopy (EIS) of the sensitized films studied in chapter 3 to understand the electronic behavior of the multi-decorated TiO$_2$ films. The chapter starts with a brief explanation of the capacities and advantages of the EIS, followed by an explanation of the obtained impedance spectra. It also discusses different models used to fit the EIS results and explain the charge carriers transport in the films. The chapter is concluded with a complete understanding of how, Au NPs improve the electron transport while P3OT facilitates the hole transport and avoids electron leakage at the same time in TiO$_2$/Au/QDs/P3OT films.

Chapter 5 encompass part of the research done during the predoctoral stay in the Group of Photovoltaics and Optoelectronic Devices in Spain, describing the materials and techniques used to improve the performance of devices by making high quality TiO$_2$ films, electrolytes and counter electrodes. It describes the experiments done to optimize the TiO$_2$ sensitization process with PbS, CdS and ZnS quantum dots by two methods; SILAR and Electrophoresis. In both cases the best conditions to maximize photocurrent and photovoltage without significantly reducing the Fill Factor were found, obtaining remarkably high efficiencies for QDs (η >3.4%).

Chapter 6 exposes the second part of the research done in Spain that was focused in the use of these semiconductor materials to efficiently produce

hydrogen using a tandem array with a dye sensitized solar cell. The chapter briefly explains the advantages of using hydrogen as energy storage method and some of the alternatives that had been explored to produce it. After that, it is described the optimization studies performed to the components of the device explaining the physical and chemical process implied in the hydrogen production. Then, it is shown the characterization result of the tandem device with the evaluation of the final solar to hydrogen production efficiency which was triplicated.

Finally, chapter 7 contains the general conclusions of this work making emphasis in the contributions of this thesis and the principal challenges that must be overcome in future research.

Table of contents

Chapter 3.

Multi-sensitized Solar Cells **30**

Chapter 4.

Impedance Modeling **44**

Chapter 1.
Solar Cells

1.1. Motivation

In the last years, the quest for clean energy sources has taken a big importance because of 3 factors: 1) Oil production: world´s principal energy source, the petroleum, is finite, and several studies indicate that the extraction of this product is already in decrement as M. King Hubbert predicted in 1949 [1]. Several countries had reached its production peak; in particular, Mexico reached it in 2004 with 3.82 million of barrel per day [2]. What is worse, the oil demand has an annual increase of 1.8%. This suggests that in 2025 the oil demand will seriously overcome the oil production. 2) Electric power demand: the actual global power demand is 15 TW which are used 3% in computers, 4% in ventilating, 7% in appliances, 9% in electronics, 10% in heating, 11% in refrigeration, 17% in air conditioning and 30% in lighting [3]. Experts estimate that electric power demand will reach 23 TW in 2050, which means 8 TW extra to cover future demands. 3) The environment: a serious problem that we affront is that many actual energy sources produce enormous amount of pollutant gases, in particular green-house gases as CO_2 whose production reaches 7910 metric tons per year.

According to such panorama, it is required to have energy sources that can substitute the depleting oil, that can provide the extra power requirements in the near future and that are able to be environmentally friendly. There are some alternatives: 1) Mineral carbon: it is more abundant than oil and can provide enough energy for more than 100 years. But it is still finite and has the issue that its useimplies a big production of CO_2 (25 billions of metric tons per year). 2) Nuclear energy: this energy source is relatively clean, producing water vapor as product of the refrigeration process, unfortunately this technology is not risk free

because of the use of radioactive fuels that could cause serious environmental damage in case of a plant breakdown. But the biggest problem is that one nuclear plant can supply approximately 1 GW. Then, to produce 8TW in 2050 it will be necessary to build 1 new plant each day for the next 37years. 3) Wind energy: a very clean energy source, it could provide up to 4 TW by using all wind currents of the earth globe. The problem with this source is to exploit the wind energy from some places, because the wind is not strong enough to move wind turbines, or the wind turbines are technically complicated to place, like over the oceans. 4) Geothermal energy: this source could provide up to 12 TW, however, the actual methods need water vapor to move turbines, and many places with this kind of energy are naturally dry heat sources. Then, it is necessary to find the way to extract the heat of the earth. 5) Biofuels: they consist of fuels made from fresh organic material like Biodiesel from sunflower seeds oil, Bioalcohol from sugar fermentation and Biogas from the decomposition of organic wastes. These sources have the problem of CO_2 production as secondary product, and in some cases they compete with food sources. 6) Solar energy: photovoltaic cells have attracted significant attention recently since solar energy on the earth is 10^4 times more powerful than any other source on the planet and is environmentally friendly [4]. The most common solar cells, silicon cells, have a photoconversion efficiency of 20 % [5]. However, the manufacturing process is expensive and involves the use of toxic chemicals. In the last decade, nanomaterials or nanostructures have emerged as a new and promising alternative for harvesting solar energy [6-9]. There are three types of solar cells based on nanostructured materials. 1) Organic cells based on molecules or semiconductors polymers sensitized with some carbon nanostructure [10-14]; 2) Inorganic cells based on inorganic semiconductor nanomaterials sensitized with another semiconductor or metallic nanoparticles [15-17]; 3) Hybrid cells based on a mixture of organic-inorganic nanostructures taking advantage of the best properties of each component and possible synergetic effects resulting of their combination [18-27].

The use of nanostructured materials for solar cells could reduce production

costs due to the low synthesis temperature and deposition methods, although photoconversion efficiency (η) for such devices is still generally much lower than that of the best silicon-based solar cells. The advantages of nanostructured solar cells include the possibility to manipulate factors like shape and size of the particles to improve the conversion efficiency, making them commercially feasible [6,22,28-32]. One key factor to increase conversion efficiency is to improve both electron and hole mobility to avoid recombination. Another common strategy to improve the photoconversion efficiency is to increase the photcurrent by increasing the photoabsoption increasing the thickness of the active region or the part of the solar spectrum that is used.

1.2. General Principles

1.2.1.   Working Mechanism

The basic design of a solar cell consists in the union of two or more semiconductor materials with different electronic and optical properties. In the particular case of Silicon based solar cells, they are based in the union of silicon doped with an excess of electrons (n type) and other with electron deficiency (p type). As n and p silicon have different Fermi levels, when both materials are joined the valence and conduction bands (B_v and B_c) are deformed as is shown in the purple and red dashed lines in Fig. 1.1. The different concentrations of electrons and electrons deficiencies (holes) induce a migration of electron and holes in the interface of the n and p type material making a concentration gradient of electrons and holes (cyan and blue solid lines in Fig. 1.1). This migration of charges also generates a region in the interface where the materials are not electrically neutral (the depletion zone), being positively charged in the n type material and negatively charged in the p material, generating an electrostatic field in this region.

3
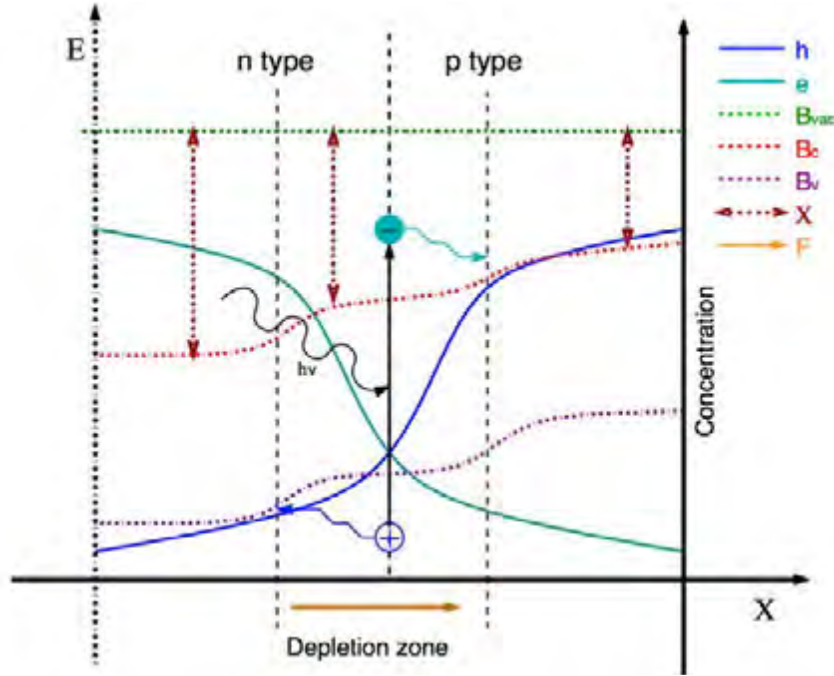
Fig. 1.1. Schematic representation of the energy levels of a silicon solar cell representing: the hole and electron concentration (h and e), the vacuum band (B_{vac}), the conduction band (B_c), the valence band (B_v) the electron affinity (χ) and the electrical force (F).

When a photon with energy higher than the band gap ($\varepsilon_g = B_c - B_v$) impinges the active area an electron is promoted from the B_v to the B_c, leaving an empty space with positive charge in the B_v (a hole). Depending of the kind of solar cell, this electron and hole could be strongly bounded (as exitons in organic cells) o free charges like in silicon cells. Once photogenerated the electron-hole pair, both charge carriers are moved by a group of forces, producing and electron J_e and a hole density current J_h. The net density current of the cell will be described by the addition of the currents as

$$J = J_e + J_h = \mu_e e \Delta E_{F_e} + \mu_h h \Delta E_{F_h},\qquad(1.1)$$

where, μ_e and μ_h are the mobility of electrons and holes respectively; e and h the electron an hole densities; E_{fe} and E_{fh} are the Fermi quasi levels for electrons and

4

holes. The fermi quasi levels are the energies where the probability to have electrons or holes (as corresponds) is 50%. E_{Fe} and E_{Fh} are affected by the conduction and valence band's energy levels densities (N_c and N_v), the presence of electrostatic fields (F), the electron affinity (defined as the energy difference between the vacuum band and the conduction band "$\chi=B_{vac}-B_c$") and the band gap width ($\varepsilon_g=B_c-B_v$). Hence, the electron and hole current densities are described as [33]:

$$J_e = D_e q \Delta(e - e_0) + \mu_e(e - e_0)(qF - \Delta\chi - k_b T \Delta(LnN_c)) \qquad (1.2)$$

$$J_h = -D_h q \Delta(h - h_0) + \mu_h(h-h_0)(qF - \Delta\chi - \Delta\epsilon_g - k_b T \Delta(LnN_v)) \qquad (1.3)$$

where, D_e and D_h are de diffusion constants for electrons and holes respectively, q is the fundamental electron charge, T is the cell temperature, k_b is the Boltzmann constant, e_0 and h_0 are the charge carriers concentrations in the equilibrium state. Then, the current density is influenced basically by two factors, a carrier diffusion process and an effective electric field composed of the field in the depletion zone, the variations in the electron affinity and the variations in the levels density. It is important to stand out that depending on the kind of solar cell one of these driving forces will be dominant. In the case of silicon solar cells (Fig. 1.1), there exist variations in χ due to the deformation of the B_c between the n and p type semiconductors and an electric field in the depletion zone. However, the current in this kind of cells is governed by the diffusion process due to the charge carrier concentration gradient.

Another important factors to consider in solar cells are: The time that an electron takes to return from the B_c to the B_v filling a hole (the recombination time τ_n), and the charge carriers velocity to move inside the cell that in Si cells is determined by the diffusion constants D_i (40 cm^{2}s^{-1} for electrons and 10 cm^{2}s^{-1} for holes [34]). This, in conjunction with the recombination time in Si (several μs) determine the maximum length that the charge carriers can travel inside $L_i = \sqrt{D_i \tau_i}$

the cell ( ) that for Si based cells is approximately 100µm [33]. Recombination time and diffusion constants are different for each material and are objet of study in the design process of new type of solar cells.

1.2.2. Efficiency Characterization

The principal indicator to evaluate a solar cell is the photoconversion efficiency (η), which is defined as the ratio of the electric power extracted from the cell and the incident light power. The experiment to calculate η consists in applying a voltage sweep to the cell under light exposition and measuring the photocurrent response resulting in a J-V curve as the one shown in the red line of Fig. 1.2. In such plot three parameters can be calculated that describe the internal processes in the cell and determine η. These parameters are short circuit current, open circuit voltage and fill factor.
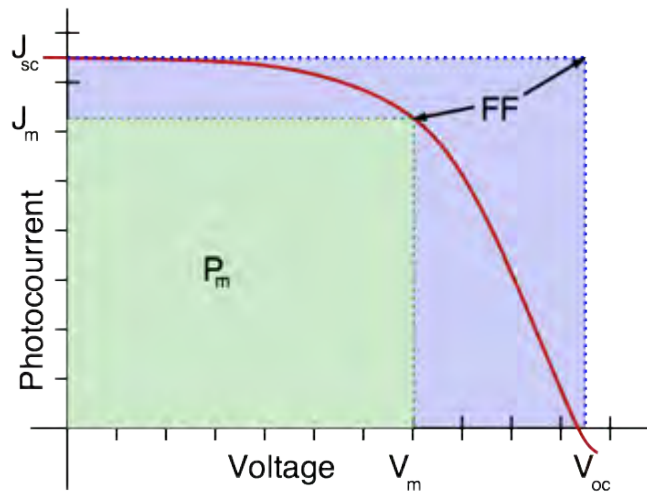

Fig. 1.2. Example of a J-V curve showing the principal parameters to evaluate a solar cell. Short circuit current (J_{sc}), open circuit voltage (V_{oc}), the maximum power (P_m) and fill factor (FF).

Short circuit current.

The short circuit current (J_{sc}) is defined as the current of the cell at "0" Volts (see Fig. 1.2). It is directly related to the external quantum efficiency (QE(E)), i.e. the probablity that a photon with energy E excites an electron to the B_c and the electron is extracted to an external circuit, by the equation

$$J_{sc} = q \int_0^\infty b_s(E) QE(E) dE$$

(1.4)

,

where q is the fundamental electron charge and $b_s(E)$ is the spectral photon flux density (the amount of photons per second per area with energy between E and E+dE that hit the device). Then, the J_{sc} will give an intuitive measure of the photogeneration of the cell, increasing and decreasing at the same time that this process. It is important to point out that J_{sc} depends on both the photoabsorption of the cell and the light spectrum shape (b_s). So, a modification of either the absorption properties of the photogenerator or the light source will affect this parameter. That is the reason why the efficiency characterization is done with a light that emulates the solar power and spectrum at the surface of the earth (usually an arc Xenon lamp). In the other side, there are specific tests like IPCE that allow to measure the QE to better understand the photogeneration process and select our photogenerators, as we will discuss later.

Open circuit voltage:

The Open circuit voltage (V_{oc}) is defined as the voltage necessary to obtain current equal to 0. The V_{oc} is determined by the maximum energy difference that can exist between electrons and holes when extracted from the solar cell. In the case of Si based solar cells, this energy difference is given by E_{Fh} and E_{Fe} at the extraction point of electrons and holes, respectively. In other cases like dye sensitized solar cells, it is determined by the alignment of energy levels of the different materials in

7

the cell. However, this energy difference always will be less than the energy of the band gap i. e. Voc < ε_g /q. Then, if we want to modify the V_{oc} it is necessary to modify the energy levels alignment of the system and band gap, which in turn will affect the other parameters of the cell.

Fill Factor.

To calculate the fill factor (FF) it is necessary to remember that the electric power is defined as the product of current and voltage ($P = J \cdot V$). Then, it could be calculated from the red plot in Fig. 1.2 as the maximum feasible power (P_m) of the cell, that will be obtained at a specific photocourrent (J_m) and voltage (V_m). These tree parameters will define the area, hight and base respectively of the green doted rectangle in Fig. 1.2. While, J_{sc} and V_{oc} define the hight and base of the blue doted rectangle. The FF is defined as de area ratio of the green and blue rectangles, that is:

$$FF = \frac{J_m V_m}{J_{sc} V_{oc}} , \qquad (1.5)$$

The FF indicates how far is the cell to be an ideal system by comparing the ideal power of the cell with the real power obtained due to the energy and electron losses. The FF makes possible to determine the process that makes the cell less or more ideal, this process is described with two kinds of resistance. The series Resistance (R_s), whose increase is related to the increase resistance to the charge carriers flux and will produce potential energy losses in the charge carriers (see Fig. 1.3a). And the Charge transfer resistance also known as Shunt resistance (R_{sh}) whose decrement (Fig. 1.3b) is related to the increase in the current losses by electron hole recombinations, current losses at the contacts or electron leakages at the edges of the device.
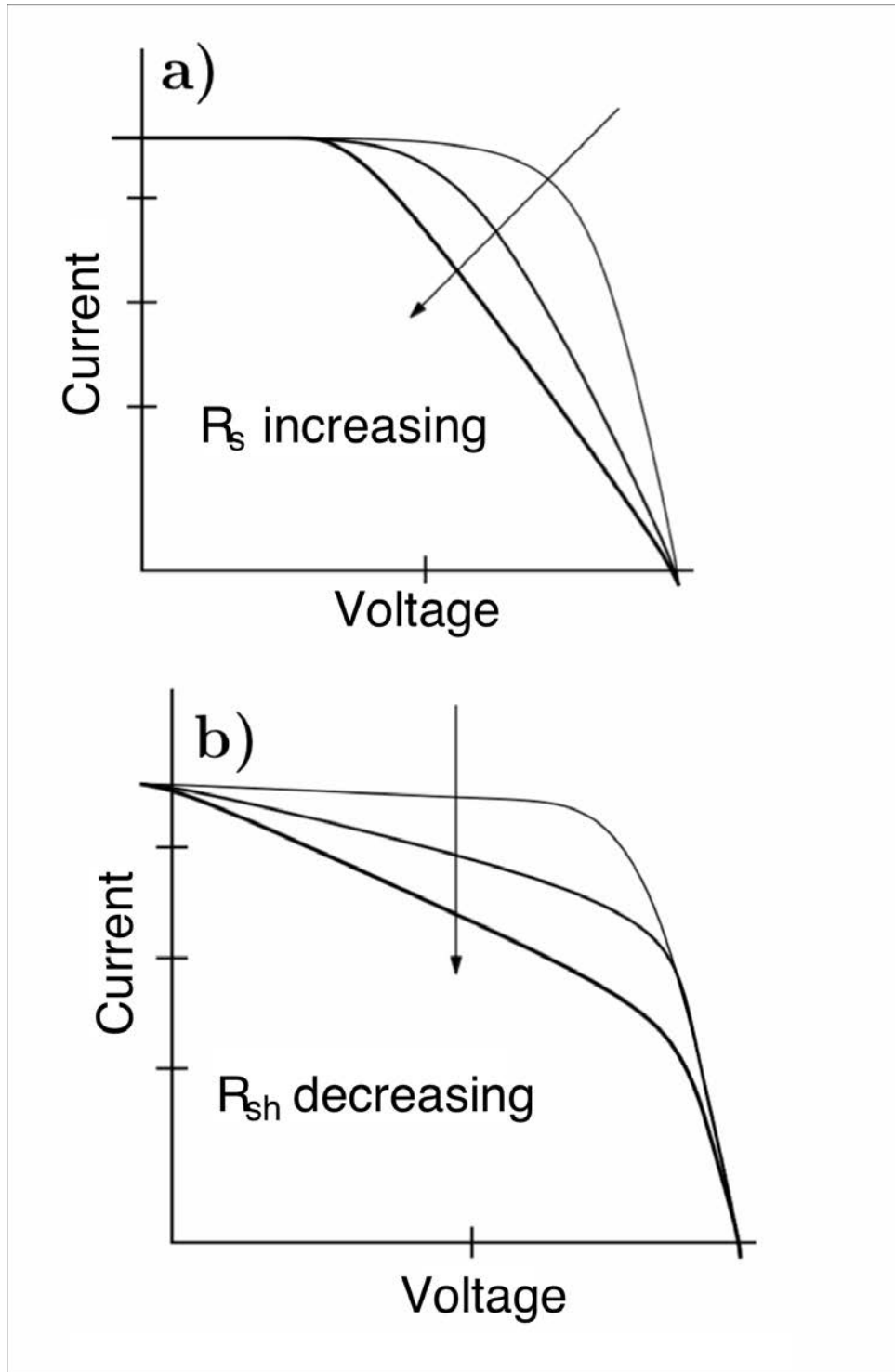
Fig. 1.3. Schematic representation of the current behavior of a solar cell when: a) the series resistance is increased, b) the recombination resistance is decreased [33].

Efficiency.

The photoconversion efficiency (η) could be calculated in terms of the maximum power as

$$\eta = \frac{J_m V_m}{P_i} \times 100 = \frac{J_{sc} V_{oc} FF}{P_i} \times 100 , \quad (1.6)$$

where, P_i is the incident light power. Then, if we want to increase η, we need to increase the J_{sc} V_{oc} and FF at the same time. Unfortunately it is not a simple labor. For example, if we consider an ideal cell (FF =1) with the maximum V_{oc} possible ($V_{oc}=\varepsilon_g$), the band gap must be increased to have an increment of the open circuit potential. However, the QE for any semiconductor will be 0 for any photon with energy E<ε_g since these photons cannot excite electrons over the B_c, then Equation 1.4 will be rewriten as:

$$J_{sc} = q \int_{\epsilon_g}^{\infty} b_s(E) QE(E) dE \quad (1.7)$$

indicating that an increase of V_{oc} by increasing the band gap will decrease J_{sc}. Then, a theoretical maximum efficiency could be calculated by rewriting Equation 1.6 as

$$\eta = \frac{\epsilon_g q \int_{\epsilon_g}^{\infty} b_s(E) QE(E) dE}{\int_{\epsilon_g}^{\infty} b_s(E) dE} \times FF \times 100 \quad (1.8)$$

Fig. 1.4 shows the theoretical η for solar cells with only one photogenerator material, using as a light source a sun at 1.5 air mass and FF =1. Here, it can be observed that the maximum η for this kind of solar cells will be 33%, obtained for a semiconductor material with 1.4 eV band gap. Because silicon has 1.1 eV, then its

10

maximum efficiency will be approximately 30% [33].
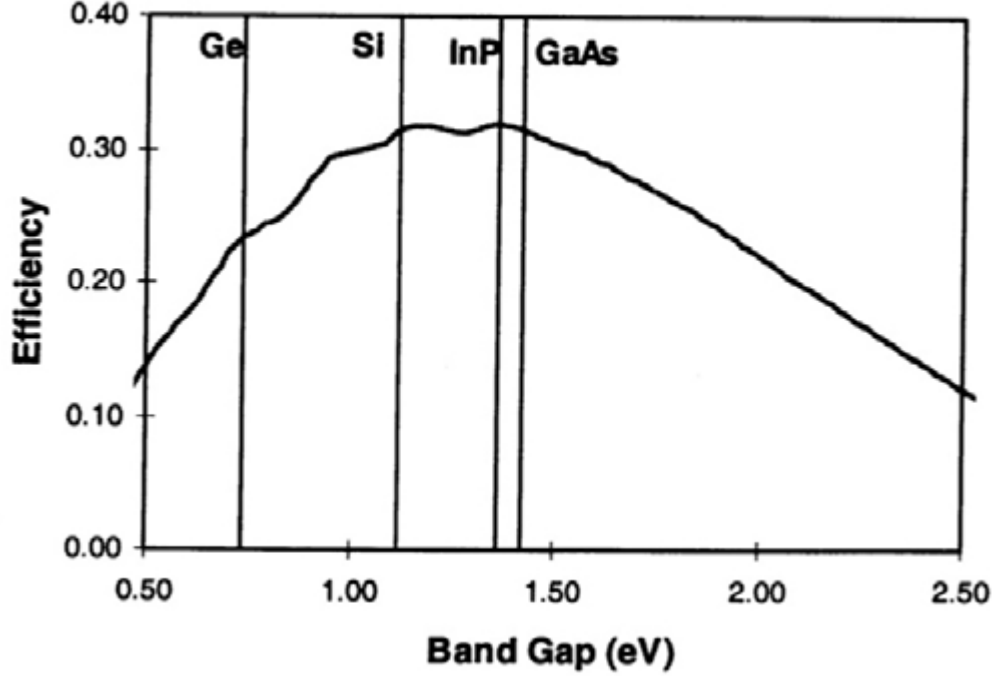
Fig. 1.4. Theoretical η of solar cells by changing ε_g of the semiconductor photogenreator material. [33]

1.2.3.   External Quantum Efficiency

Another complementary measurement for solar cell characterization is the Incident Photon to Current Efficiency (IPCE), which is defined as the ratio of the number of extracted electrons (e_{ex}) to the number of incident photons (ph_i) at certain wavelength (λ), i.e. the external quantum efficiency (QE).

$$IPCE = QE = \frac{e_{ex}}{ph_i}$$

(1.9)

To calculate the QE, it is necessary to consider that J_{sc} and the number of

electrons extracted from the cell are related as

$$J_{sc} = \frac{q \cdot e_{ex}}{A \cdot t},$$ (1.10)

where, q is the fundamental electron charge, A is the solar cell active area and t is the time. Meanwhile, the incident light power P_i is related with the number of photons (ph_i)as:

$$P_i(\lambda) = \frac{h \cdot c}{\lambda \cdot A \cdot t} ph_i,$$ (1.11)

being h the Planck constant and c the light velocity. Finally, we can express the IPCE in terms of J_{sc} and P_i as [28]

$$IPCE = \frac{h \cdot c}{q} \frac{J_{sc}}{\lambda \cdot P_i(\lambda)} = 1240 \frac{J_{sc}[A/cm^2]}{\lambda[nm] \cdot P_i[W/cm^2]}$$ (1.12)

As previously mentioned, this measure will be very helpful to characterize the origin of J_{sc}. IPCE could determine which material contributes to the photogeneration at each λ and how efficient it is. In this way, it is possible to select one or other material to complement the photogeneration or use a specific region of the solar spectrum to increase the photocurrent.

1.3. Organic Solar Cells

The organic solar cell technology is based in fulleren and polymer semiconductors. These materials have in their atomic structure hybrid bounds SP_2, divided in two kinds of orbitals π and $π^*$ that could be visualized as two bands, one completely full with electrons represented by Highest Occupied Molecular Orbital (HOMO), and another completely empty, that is represented by the Lowest Unoccupied

Molecular Orbital (LUMO). When a photon reaches these organic materials, an electron-hole pair is generated and are strongly electrostatic linked (0.1 to 1 eV) forming an exciton. To break the exciton bound is necessary to use materials with different electron affinities (see Fig. 1.5), one that prefers to donate electrons, and another one that prefers to accept them. Some examples of donor materials are, MDMO-PPV (poly[2-methoxy-5-(3,7-dimethyloctyloxy)]-1,4-phenylene- vinylene), P3HT (poly(3-hexylthiophene-2,5-diyl)) and PFB (poly[9,9'-di-octyluorene-co-bis-N,N'-(4-butylphenyl)-bis-N,N-phenyl-1,4-phenylenedi-amine]); and the more common acceptor materials are CN-MEH-PPV (poly[2-methoxy-5-(2'-ethylhexyloxy)]-1,4-(1-cyanovinylene)-phenylene), F8BT (poly(9,9'-dioctylu orene-co-benzothiadiazole)) and PCBM ([6,6]-phenyl C61 -butyric acid methyl ester). Electrons in the LUMO of the donor material are injected to the acceptor by the energy difference of the materials. Once electrons and holes are separated, they are driven by an electric force due to the difference in the work function of the electric contacts (Fig. 1.5 b). Then, in this kind of cells, the maximum electron distance before recombination is given by

$$\mathrm{d} = \mu\tau\mathrm{F} \text{ ,} \qquad\qquad (1.12)$$

where, τ is usually 1 μs and $\mu \sim 10^{-4}$ cm^2/Vs. With gold (ϕ=5.2 eV) and aluminum (ϕ =4.3 eV) at 90 nm as contacts, the electric field will be 5.2 × 10^5 V/cm^2, then an electron in this material could travel around 100 nm making this array viable for solar cells. The main problem in this material is that exciton has a very short diffusion length (5 to 20 nm). Then, the active zone must be in the donor acceptor interface and at the same time extended in all the thickness of the cell to maximize the light absorption. Therefore, donor and acceptor must be mixed as schematized in Fig. 1.5a. In addition, V_{oc} will be limited by the HOMO-LUMO energy difference and the work function of the metallic contacts. The correct selection of the materials of the cell in particular the donor and the acceptor is vital to obtain high efficiencies. One of the most studied junctions is the Polymer-Fulerene with a conversion efficiency of 5.2%.
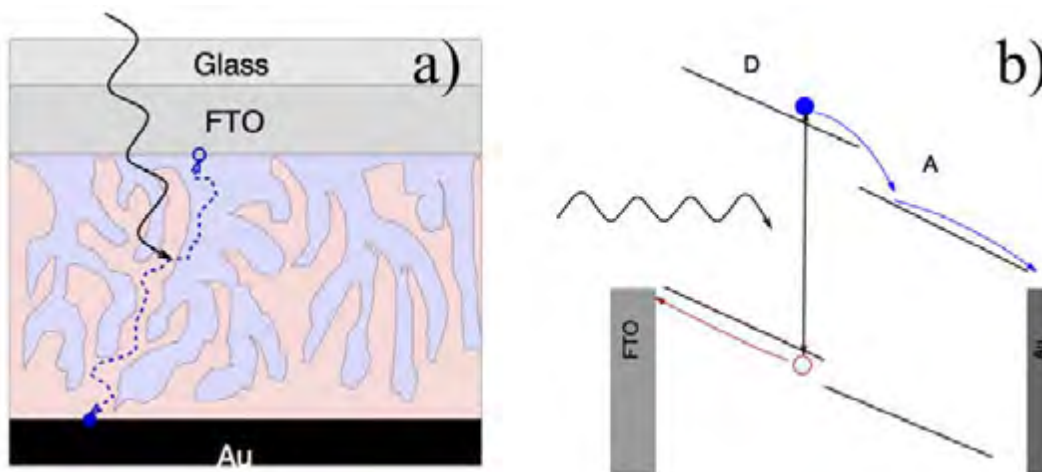
Fig. 1.5. Schematic representation of a) an organic solar cell and b) the energy levels of an organic solar cells.

1.4. Grätzell Solar Cells

One of the most studied hybrid type nanostructured solar cells is the Grätzel or dye sensitized solar cell (DSSC) [32,35-41]. This kind of cells typically consists of a TiO_2 nanocrystals (NCs) film deposited on a transparent conductive oxide (TCO) like indium tin oxide (ITO) or fluorine doped tin oxide (FTO). This TiO_2 serves as a high porous matrix where dye molecules are adsorbed. Such sensitized TiO_2 film is immersed in an electrolyte, typically , I^-/I_3^- which is in contact with the counter-electrode of the cell (see Fig. 1.6a). When a photon impinges in a dye molecule, an electron is promoted from HOMO to LUMO, generating an electron hole pair. As the TiO_2 NPs and dye molecules are in nano scale, the energy bands in each material are not deformed by the presence of the other one, i. e. they have "flat energy bands" (Fig. 1.6b). Then, electrons and holes (e^- and h^+) inside of the dye do not feel any force producing a random movement until e^- reach the TiO_2/dye interface and h^+ reach the dye/electrolyte. Electrons in TiO_2/dye feel a strong force due to variations in χ, (the energy difference between LUMO in dye and B_c in TiO_2) and are injected to the TiO_2's B_c (Fig. 1.6b) where they are driven by electron concentration gradient to the metallic contact. In a similar way holes feel a force

due to the energy difference between the HOMO and the RedOx (ϕ_{RedOx}) potential of the electrolyte, and oxidizes I^- to the I_3^- electrolyte moves by diffusion to the counter electrode were is reduced to I^- again.
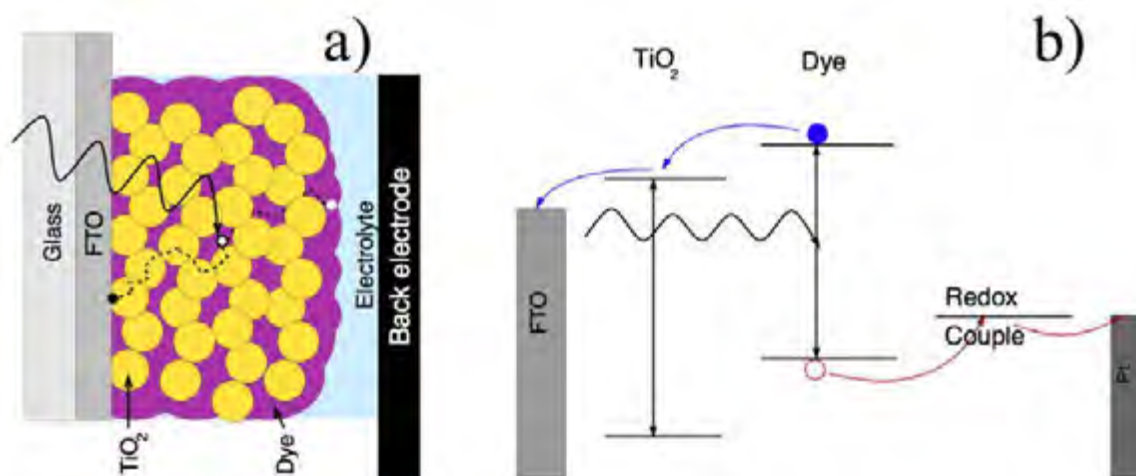
Fig. 1.6. a) Schematic representation of a DSSC and b) Energy levels and photocurrent generation process in a DSSC.

Nanostructured TiO_2 cells have many features that can affect the photoconversion efficiency. As particle size increases, surface defects and grain boundaries are reduced and consequently the charge carrier recombination decreases, resulting in increased fill factor [6]. However, the sensitizer-metal oxide interaction area is reduced, relatively to volume, resulting in photocurrent decrease.

1.5. Quantum Dots Solar Cells

The largest photoconversion efficiency of DSSC reported in literature is 12% [5,42], obtained with a ruthenium-based dye [22, 24, 30, 32, 37, 39, 43]. Unfortunately, this kind of solar cells are costly because of the high price of the ruthenium dyes. An alternative to DSSC is the use of quantum dots (QDs), e.g., CdSe, CdTe, CdS,

PbS, PbSe, Bi$_2$S$_3$ and InP [16,17,28,38,44-49], as sensitizers to replace the expensive ruthenium dyes. QDs have large extinction coefficients in the visible region and, after band gap excitation, undergo charge separation, injecting electrons to the conduction band of metal oxide according to the following equations

$$QDs + h\nu \rightarrow QDs(e^- + h^+)$$ (1.13)

$$QDs(e^- + h^+) + TiO_2 \rightarrow QDs(h^+) + TiO_2(e^-)$$ (1.14)
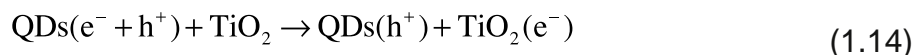
Thus, the charge separation is improved by coupling QDs with metal oxides (MOs) with appropriate energetics. The driving force for electron transfer between QDs and TiO$_2$ is dictated by the energy difference between the conduction band edges. For example, the conduction band edge for CdSe QDs varies from -0.8 V to 1.57 V vs normal hydrogen electrode (NHE) for size ranging from ~7.5 nm to 3 nm [50], while the conduction band edge of TiO$_2$ is located at -0.5 V vs NHE [51]. Therefore, it is possible to increase the driving force for electron transfer by controlling the crystallite size of QDs, which in turn can improve the conversion efficiency.

Recently, synergistic effect was reported when QD sensitization is combined with N-doping, in which N-doping is proposed to facilitate the hole transport while QDs act as sensitizers [44]. N-doping into TiO$_2$ lattice results in a red-shift of the electronic absorption and enhanced photocurrent response relative to undoped TiO$_2$ films [44,52,53]. In that report, CdSe QDs linked to TiO$_2$:N NCs were found to significantly increase the photocurrent and photoconversion efficiency of the films compared to standard TiO$_2$:N films without QD sensitization [44]. QDs-sensitized TiO$_2$ solar cells have been reported to have quantum efficiency (QE) as larger as 12 % [44,54], but photoconversion efficiency (η) of only 4.44% has been reported recently [55]. Thus, for such configuration, it is necessary to improve the electron injection efficiency to increase η and take advantage of QDs' strong photoabsorption in the visible and near infrared.

1.6. Solid Hole Conductors

Another alternative to DSSCs is the use of a hole-conducting polymer for the regeneration of the dye complex. Thiophene derivatives seem to be the best option for this purpose [24]. Although possessing a longer useful life due to polymer photostability, this configuration has lower efficiency than DSSCs with liquid electrolyte. Thiophene has been widely used in organic solar cells for making heterojunctions with fullerene derivatives (acceptor) and a photoconversion efficiency up to 5% was reported for a configuration with donor-acceptor [56-59]. The extremely low electron mobility of polymer is compensated with the fast electron transfer to fullerene or another molecule [60-62]. QDs have also been used as electron acceptors, resulting in an improved charge separation because of the favorable energy difference in conductive band edges and higher electron mobility. In this configuration, QDs are used as the electron transporter whereas thiophene is used as an effective hole transporter, resulting on a photoconversion efficiency of 1.7% [63]. More recently, thiophene composed with TiO_2 NCs as an electron conducting layer was found to improve the conversion efficiency up to 3.9% [19].

1.7. Electron Conductors

The photoresponse of semiconductors has also been improved by the presence of metallic NPs such as gold (Au) and silver (Ag), although the mechanism of the observed enhancement is not completely understood [64-68]. It has been suggested that such NPs act as electron traps to help separate the photogenerated charges and then improve interfacial charge transfer [67-70]. Studies have shown a shift in the Fermi level to a higher negative level by decorating the semiconductor with metal NPs. This shift enhances the efficiency of interfacial charge transfer process [71]. In this case, it has been reported a 40% improvement of hole transfer efficiency from semiconductor film to electrolyte [69]. Alternatively, metallic NPs

have been suggested to act as sensitizers in TiO_2 NCs and zinc oxide (ZnO) nanowires, similar than organic dyes, based on the photoresponse and the absorption spectra of metallic NPs [68-72]. In such a case, the electron injection from Au NPs to TiO_2 competes effectively with electron relaxation within Au NPs. Enhancement of photoconversion efficiency has also been reported in Si-thin films with the presence of Au NPs. In this case, the mechanism proposed is based on the absorption enhancement of Si-thin film via the excitation of surface plasmon resonance (SPR) [73,74]. However, for larger particle size, the dominant mechanism is based on the increment of light scattering and then absorption of Si-thin film [75-77]. Furthermore, plasmon-assisted current generation for single crystal TiO_2 and Au nanorods using visible to near IR light was reported recently [78]. Similarly, a strong increase in photoconversion efficiency with QDs sensitized Au-TiO_2 NPs composite has been found which was attributed to enhanced absorption of QDs caused by increased scattering of light by the Au NPs [64]

Chapter 2.
Single Sensitized Solar Cells

In this chapter, a systematic comparison of TiO_2 films sensitized with CdSe Quantum dots (TiO_2/QDs), TiO_2 films decorated with gold nanoparticles (TiO_2/Au NPs) and films decorated with poly 3-octyl thiophene (TiO_2/P3OT) is described. The synthesis and characterization of the basic components of the cells and the electrochemical characterization of the composite films are reviewed.

2.1. Synthesis of the Materials

2.1.1. TiO_2 Film Preparation

TiO_2 NCs were prepared by a sol-gel method. 3.75 ml of titanium isopropoxide (IV) and pluronic F127 were added in a solution of 5 ml of H_2NO_3 in 50 ml of absolute ethanol (EtOH) and 2.5 ml of H_2O, the mixture was stirred one hour. The synthesis process was done in a glove box with N_2 atmosphere. The mixed solution was transferred into a teflon autoclave. The hydrothermal treatment was carried out at 70ºC during 12 h outside the glove box. The resulting xerogel was washed three times with EtOH and annealed for one hour at 550 ºC. The TiO_2 powder was suspended in EtOH and deposited on ITO substrate by doctor blade method.

2.1.2.   CdSe QD Synthesis

To synthesize high-quality CdSe QDs, CdO was used as the Cd precursor and 1-tetradecylphosphonic acid (TDPA, 99%) and trioctylphosphine oxide (TOPO, 99%) are used as surfactants. Synthesis was performed in air-free reaction conditions according to the procedure proposed in ref. [16], where 0.05 g (0.39 mmol) of CdO,

0.3 g (1.1 mmol) of TDPA and 4 g (10.3 mmol) of TOPO were heated to 110 °C, degassed under vacuum and then heated to 300 °C under a nitrogen flow , [16,44,79]. A SeTOP (0.7 wt%) solution was prepared in inert atmosphere by adding 0.026 g of Se powder with 4.25 ml of TOP stirring for 1 h to ensure complete dissolution of the Se powder. After reaching 300 °C, the Cd-TDPA-TOPO solution was cooled to 270 °C prior to the injection of SeTOP. Under a nitrogen flow, 3 ml of SeTOP were injected lowering the temperature to 260°C. The temperature was then increased to 280 °C to facilitate particle growth; aliquots were removed and probed to track QD growth via UV-Vis absorption spectroscopy. The CdSe solution was cooled and removed from the reaction flask at around 80 °C and dissolved into 10 ml of toluene. It was cleaned twice through a precipitation and decantation process using methanol and centrifugation at 3000 rpm. QDs were ultimately dispersed in toluene prior to their use as a sensitizer. The resulting CdSe QDs were in the strong confinement size regime as will show in the structural and morphology description.

2.1.3.   Au NPs Synthesis

Au NPs were synthesized by reacting 10 mL of a 0.2 M solution of cetyl trimethylammonium bromide (CTAB) with 5 mL of 0.5 mM solution of $HAuCl_4$. The mixture was stirred in an ice bath to which 0.60 mL of 0.01 M $NaBH_4$ was added, resulting in a brown solution. The solution was stirred for 2 h to obtain 5.5 nm particle size which was verified via TEM and UV-vis absorption spectroscopy. The final solution was stored in a dark environment to avoid light exposure for later use.

2.1.4.   P3OT Preparation.

In this work, poly (3-octylthiophene) supplied by Sigma was used. A solution of 10^{-5}M in toluene of P3OT was made. The band gap of the P3OT was measured via UV-vis absorption spectroscopy derivate. The solution was stored in the dark before its use as sensitizer.

2.2. Structure and Morphology

Raman spectra were measured by exciting the TiO_2 NC powder with a HeNe laser, with a power of 60 mW and a wavelength of 632.8 nm, focusing the beam with a 40x microscope objective. The spectra were collected from 200 to 1000 cm^{-1}. A JEOL model JEM-1200EX transmission electron microscope (TEM) was used to verify the TiO_2 NC size. The composition was measured by electron energy loss spectroscopy (EELS), and the crystalline phase was studied by electron diffraction pattern (EDP).
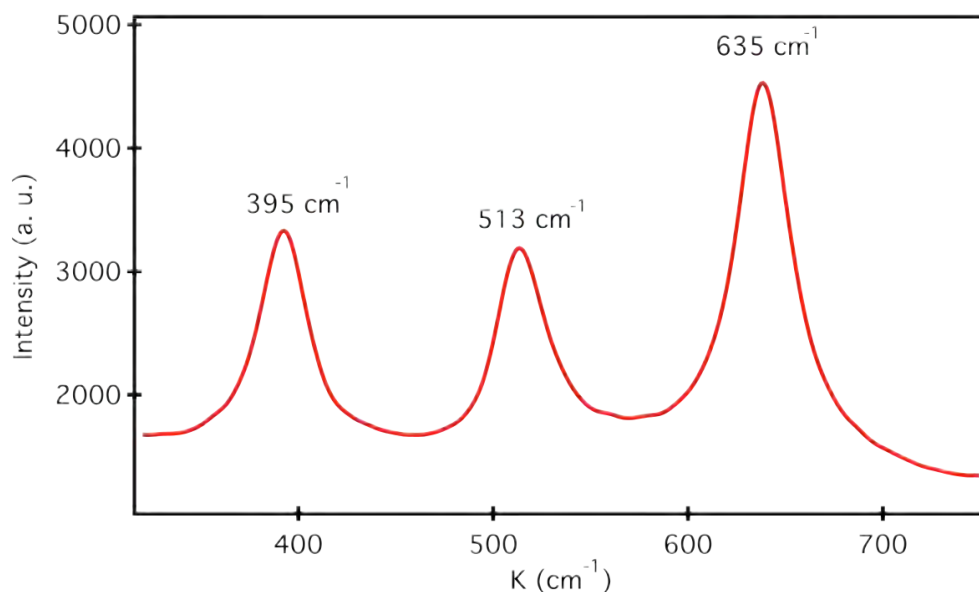
Fig. 2.1. Raman spectrum of TiO2 NCs powder annealed at 550 oC for one hour.

The Raman spectrum of TiO_2 NCs powder in Fig. 2.1 shows the well-defined characteristic peaks of anatase crystalline phase at 395 cm^{-1}, 513 cm^{-1}, and 635 cm^{-1}, indicative of a high degree of crystallinity [80]. The morphology of the TiO_2 NCs is shown in Fig. 2.2a, while Fig. 2.2b shows the electron diffraction pattern (EDP) with diffraction lines corresponding to the (1,0,1), (0,0,4), (2,0,0), and (2,1,1) planes of anatase TiO_2. The average crystallite size was 13 nm in diameter, and the size distribution is shown in Fig. 2.2c. The composition of the NCs powder was studied by using EELS, and the resulting spectrum is shown in Fig. 2.2d which displays peaks centered at 450, 465, and 535 eV that correspond to titanium L3

and L2 and oxygen K energy levels, respectively. Fig. 2.3 displays the TEM images of both QDs and Au NPs as well as the size distribution with average sizes of 4.5 and 5.5 nm for CdSe and Au NPs, respectively.
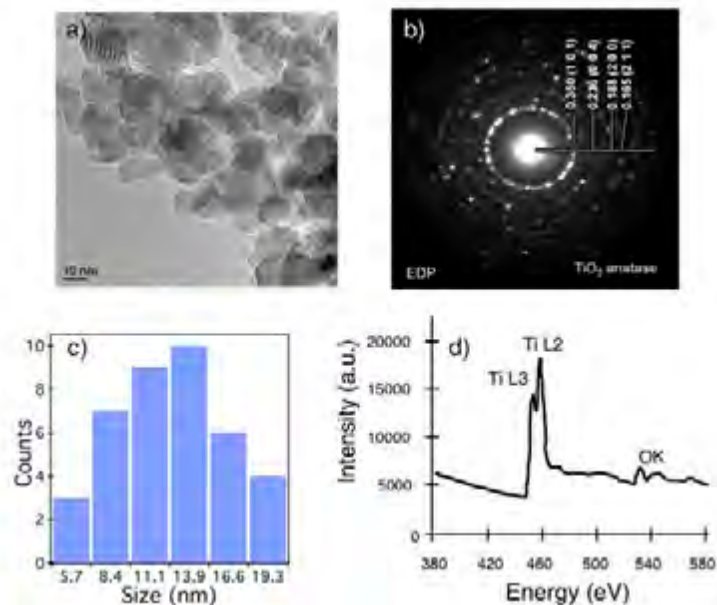
Fig. 2.2. a) Typical TEM image, b) Electron Diffraction Pattern (EDP), c) size distribution and d) EELS spectrum of TiO_2 NCs.
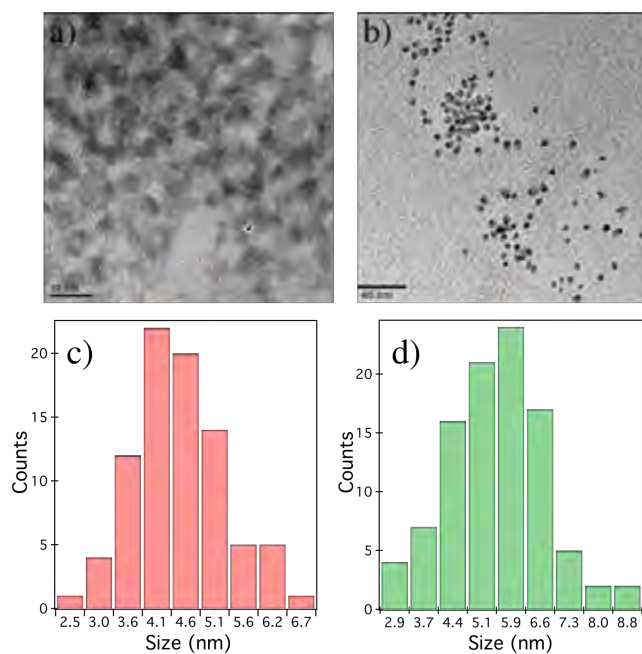
Fig. 2.3. TEM image of a) CdSe QDs and b) Au NPs, and size distribution of c) CdSe QDs and d) Au NPs.

22

2.3. Optical Properties

UV-VIS absorption spectra were measured with a Perkin-Elmer spectrophotometer (Lambda 900). The TiO_2 spectra were measured via reflectance in pellets of compact powder, scanning between 200 to 800 nm using an integrating sphere of 60 mm.
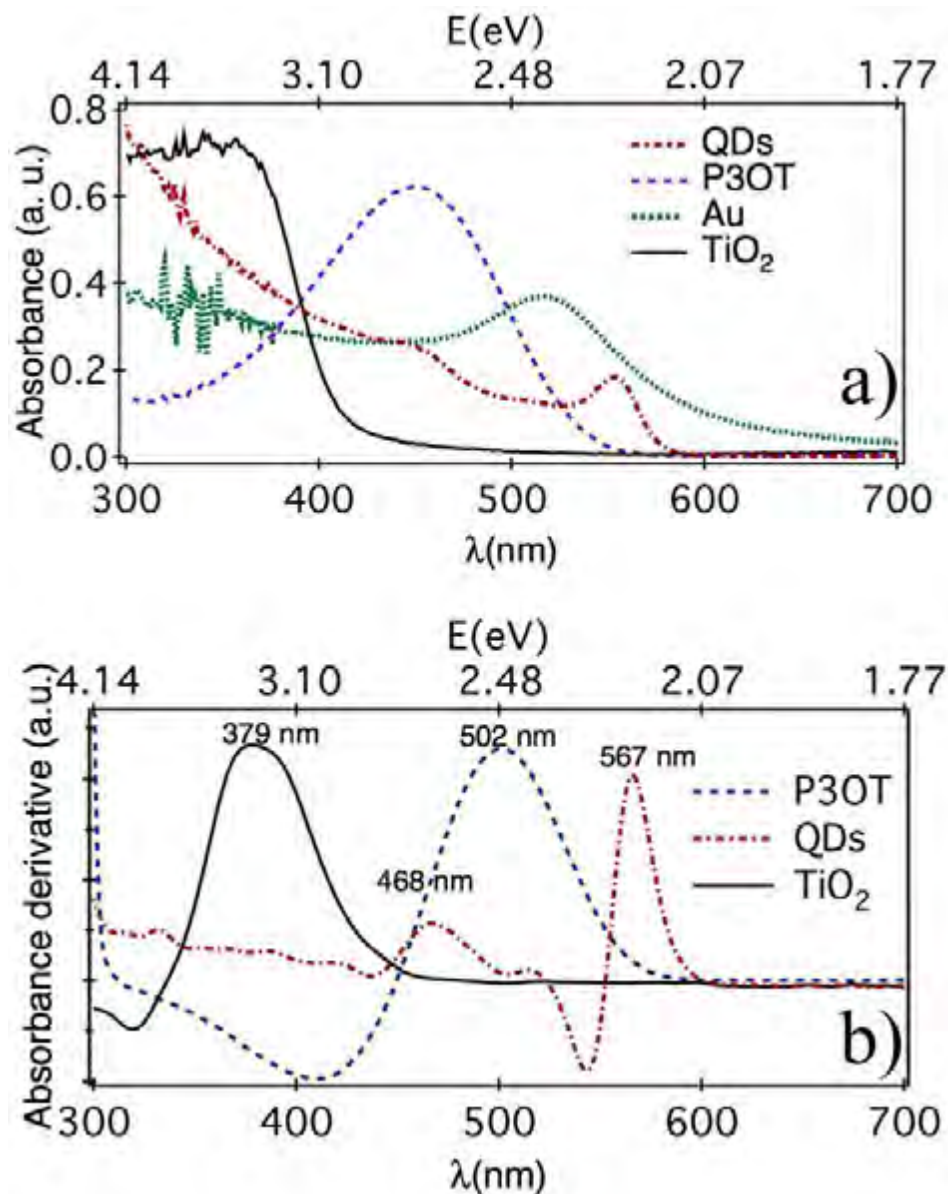
Fig. 2.4. a) Absorption spectra of Au NPs, P3OT, CdSe QDs, TiO_2 NCs. b) first derivative of absorption spectra of P3OT, CdSe QDs and TiO_2 NCs.

The absorption spectra of TiO_2 NCs, P3OT, CdSe QDs, and Au NPs are shown in Fig. 2.4a. The characteristic absorption peaks for each component are centered at 338 nm (3.67 eV), 459 nm (2.7 eV), 552 (2.24 eV), and 517 nm (2.40 eV), respectively. The absorption spectrum of Au NPs is characteristic of the surface plasmon resonance (SPR) expected for such size of NPs. [81] The first derivative of the absorption spectrum was calculated to estimate the threshold bandgap of each compose. The resulting curves exhibit peaks centered at 379 nm (3.27 eV), 502 nm (2.47 eV), and 567 nm (2.18 eV) associated with the bandgap of TiO_2, P3OT, and QDs respectively, as shown in Fig. 2.4b, being in agreement it the literature reported values [82,83].

2.4.   Film Sensitizing and Photovoltaic Evaluation

CdSe QDs, Au and P3OT were linked to TiO_2 NCs thin films to form TiO_2/QDs, TiO_2/P3OT and TiO_2/Au. Thioglicolic acid (TGA, HSCH2COOH) was used as a molecular linker for QDs and Au NPs. $TiO_2$ has a strong affinity to the carboxylate group of the linker molecules, while the sulfur atom from the TGA binds strongly to both QDs and Au NPs through surface interaction (Fig. 2.5a and Fig. 2.5b) [79]. TiO_2 films were dried on a hot plate at 100 ºC for 1 h to remove excess of H_2O. They were then immersed in a TGA solution diluted to 70% in the presence of CH_3Cl for 12 h in a nitrogen atmosphere glovebox. Consequently, they were immersed in toluene to remove the excess of TGA and immersed in a solution containing CdSe QDs, P3OT, or Au NPs for 12 h inside the glovebox. The resulting films of 1.61 cm^2 of active area were stored in a nitrogen-filled glovebox and not exposed to light prior to photoelectrochemical (PEC) characterization. Fig. 2.6a a shows a characteristic TiO_2 film with 250 nm before sensitization, meanwhile, Fig. 2.6b shows a TiO_2 after CdSe QDs sensitization, uniformly covered with a CdSe QDs layer, similar covering was obtained with Au NPs and P3OT.
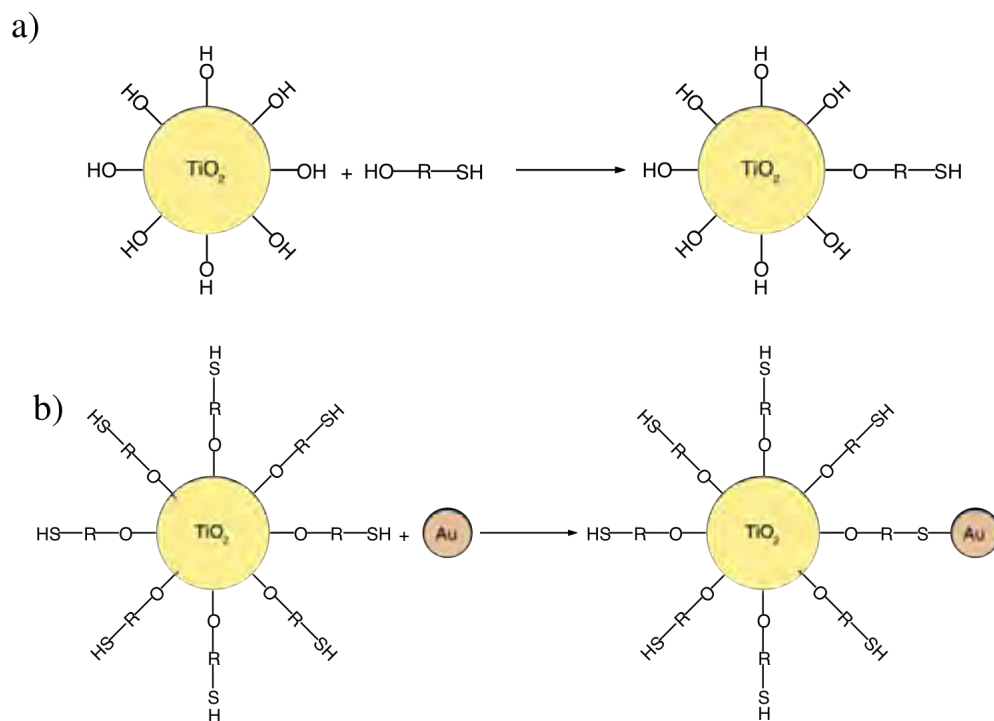
Fig. 2.5. Schematic representation of TiO$_2$ NCs decoration. a) Functionalization with TGA (R = CH$_2$CO). b) Decoration whit Au NPs.
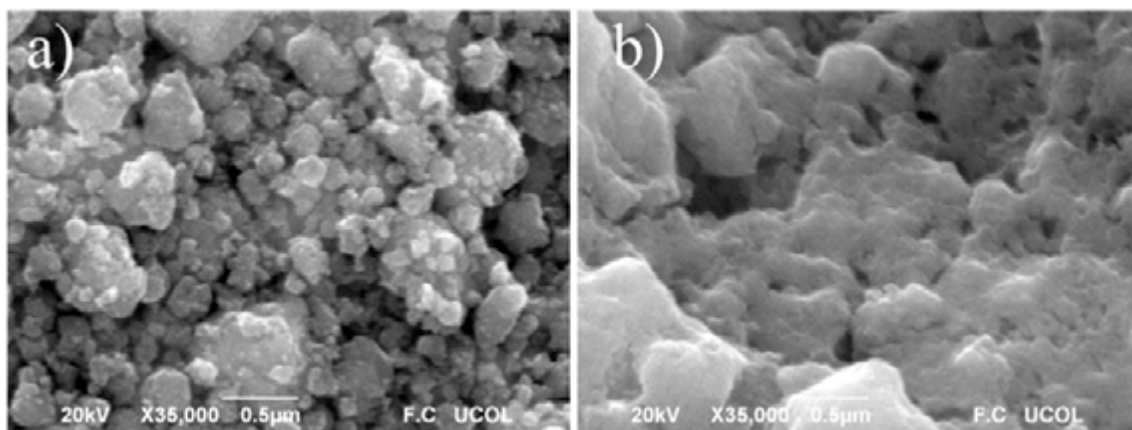
Fig. 2.6. Representative SEM image of TiO$_2$ films with (236 nm) of average particle size a) without decoration, b) decorated with CdSe QDs.

2.5. Photoconversion Measurements

Electrochemical measurements were made in a three-electrode cell using the sample as the working electrode which was illuminated with 31.83 mW/cm^2 from a halogen lamp. A saturated calomel electrode (SCE) was used as the reference electrode, while a platinum (Pt) wire was used as the counter-electrode and sodium sulfate (Na$_2$S) as the electrolyte using a Gamry Reference 600 potentiostat (Fig. 2.7). The electrolyte was purged with N$_2$ for ten minutes, although a small amount of O$_2$ could have remained in solution and played the role of electron scavenger however, the amount of hole scavenger should be much higher. The excess of O$_2$ in the electrolyte could induce loss of electrons by recombination with O$_2$ and thus may affect the conversion efficiency.
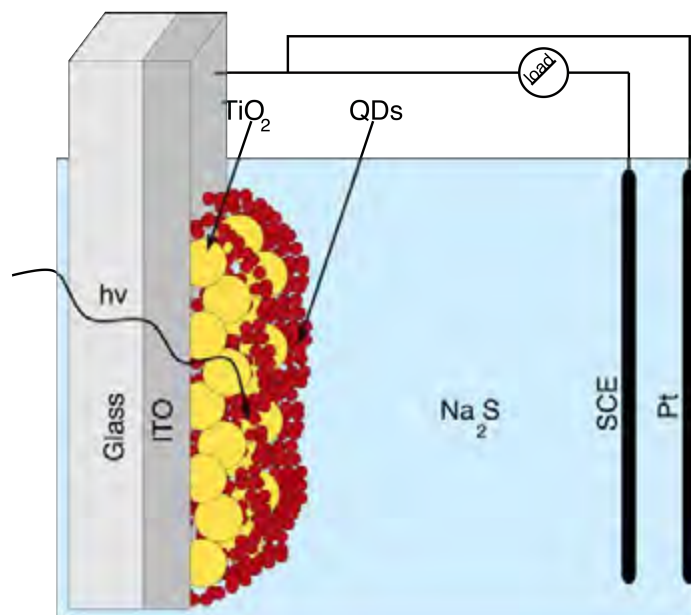
Fig. 2.7. Schematic representation of experimental arrangement to do the photovoltaic evaluation of the 10μm sensitized TiO$_2$ films

The current density-voltage (J-V) profiles for solar cells fabricated with different sensitizers were obtained. In Fig. 2.8 it can be appreciated that all decorated systems have a higher photocurrent than TiO$_2$ films without sensitizers.

The highest photocurrent was achieved for the TiO_2/QDs and the lowest one for TiO_2/P3OT cell. The short-circuit current and open-circuit voltage found in Fig. 2.4 are summarized in Table 2.1. The Fill Factor (FF) and power conversion efficiency (η) are also listed in Table 2.1 and were calculated by using the Equation 1.5 and 1.6. [84]
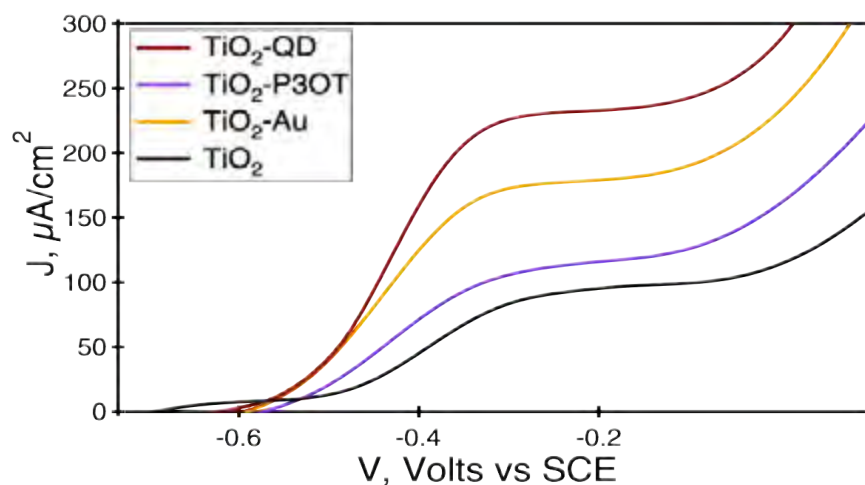
Fig. 2.8. Characteristic J-V curves of decorated and no decorated TiO_2.

Table 2.1. Efficiency of the solar cells under 31.83 mW/cm^2.

Sample	Jsc μA/cm2	Voc mV	FF %	η %
TiO₂/QDs	237	447	44.4	0.149
TiO₂/Au	183	437	51.8	0.130
TiO₂/P3OT	124	443	46.6	0.080
TiO₂	102	549	18.1	0.034

It is clear that TiO_2-Au films exhibit the highest FF (51.8%) followed by TiO_2/P3OT (46.6%) and TiO_2/QDs (44.4%). However, the highest photocurrent was achieved for TiO_2/QDs (237 μA), with the highest efficiency reported here (η=0.149%).

27

2.6. Discussion

The efficiency of TiO_2/QDs films is due to QDs capacity to photogenerate charge carriers with a large QE (~12%) [54]. When this kind of cell is illuminated, light excites electrons from the valence band (B_v) of TiO_2 and QDs to their respective conduction band (B_c), as shown in Fig. 2.9a. Electrons in QDs B_c are injected to TiO_2 B_c due to the potential difference between bands. In TiO_2, electrons are transported to ITO substrate avoiding recombination process with the wide band gap of TiO_2. Even if photogeneration of QDs increases the charge carriers population and consequently the photocurrent, QDs have small injection coefficient and relatively high resistance, that is the reason why many of the charge carriers recombine before being injected into TiO_2; thus, limiting the FF parameter.
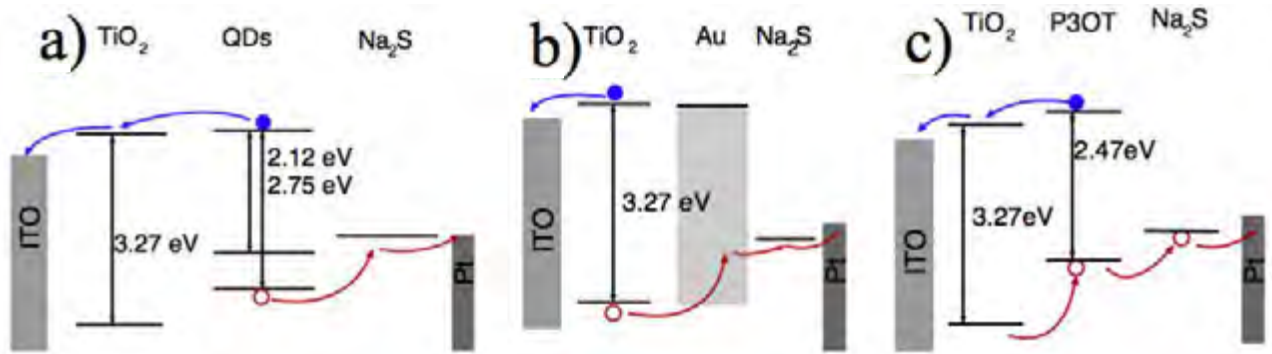
Fig. 2.9. Schematic representation of the energy levels of decorated and sensitized TiO_2 films. Blue and redlines indicate possible paths of electron and holes, respectively.

In the TiO_2/Au system (Fig. 2.9b), the increase in FF suggests a strong interaction between TiO_2 and Au NPs due to Au conductive attributes. The work function of the Au moves to be at the same level than the Fermi level of the TiO_2. When this kind of cell is illuminated, the photo-generation of charge carriers is done by the TiO_2 and the Au nanocrystals act as electron traps [67], this electron

28

trapping effect helps to separate the photogenerated carriers avoiding charge recombination and improving the interfacial hole transfer from the TiO_2 to the electrolyte increasing the injection rate and the photocurrent. The problem with this configuration is the dependence of the UV light absorption of TiO_2. So, it has poor photogeneration, but its injection rate is high enough to give an important increment in the efficiency.

In the TiO_2/P3OT system (Fig. 2.9c), P3OT transports the holes from the TiO_2 to the electrolyte in contrast to TiO_2/Au system, P3OT can contribute with the photogeneration of charge carriers as it needs lower excitation energies. But, P3OT has low electron injection efficiency to TiO_2, and only a small amount of the electrons generated in P3OT can arrive to TiO_2 and contribute whit the current. Additionally, the hole transport in P3OT is less efficient than in Au, in consequence the FF parameter and the photoconversion efficiency of P3OT decorated TiO_2 are less than the Au decorated TiO_2.

2.7. Conclusions

The efficiency of TiO_2 films decorated with Au, P3OT and QDs were compared. Results suggest, as it will be demonstrated next chapters, that these systems increment the photoconversion efficiency in different ways. Au improves hole injection rate by increasing the charge carriers separation in TiO_2, P3OT increases the hole transport and CdSe QDs increments the photogeneration of charge carriers. It also was found, that each system has disadvantages. TiO_2/Au system depends of the UV TiO_2 absorption, TiO_2/P3OT system partially depends of TiO_2 and has slow electron injection, and TiO_2/QDs have slow charge carriers injection. It was found that the best efficiency was achieved with QDs (η=0.149%).

Chapter 3.
Multi-sensitized Solar Cells

According to the experimental results of the previous chapter, CdSe sensitized TiO$_2$ films could be improved using conductor layers to increase the charge carrier transport. In this chapter we discuss, a systematic characterization of TiO$_2$ films composited with poly-3-octylthiophene (P3OT), CdSe QDs and Au NPs in different configurations. The goal was to improve the overall photoconversion efficiency by extracting in a more efficient manner the electrons from QDs with the help of Au NPs and by increasing the hole transport with the presence of P3OT. A detailed study of the optical, and photoelectrochemical properties has been carried out to gain new insight into the underlying mechanism. While the Au NPs increase the electron injection rate from CdSe QDs to TiO$_2$, P3OT injects electrons by absorbing the remaining visible light not absorbed by the QDs and increases the hole transport. In conjunction, Au NPs and P3OT improve the regeneration of QDs and facilitate the overall photocurrent generation of the sensitized TiO$_2$ NC films.

3.1. TiO$_2$ Films Decoration

Au Nps, CdSe QDs, and TiO$_2$ syntheses as well as TiO$_2$ film deposition, were explained in the previous chapter.

CdSe QDs, and P3OT were linked to TiO$_2$ NCs thin films to form TiO$_2$/QDs, TiO$_2$/P3OT, TiO$_2$/QDs/P3OT TiO$_2$/P3OT/QDs, TiO$_2$/Au/QDs, TiO$_2$/QDs/Au, TiO$_2$/QDs/Au/P3OT, TiO$_2$/P3OT/QDs/Au and TiO$_2$/Au/QDs/P3OT. Thioglicolic acid (TGA, HSCH2COOH) was used again as a molecular linker for QDs and Au NPs. TiO$_2$ films were dried on a hot plate at 100 ºC for 1 h to remove excess of H$_2$O. They were then immersed in a TGA solution diluted to 70% in the presence of CH$_3$Cl for 12 h in a nitrogen atmosphere glovebox. Subsequently, they were

immersed in toluene to remove the excess of TGA and immersed in a solution containing CdSe QDs or Au NPs for 12 h inside the glovebox. The second and third component layers were deposited in a similar way. From this, only the first component was strongly linked to TGA, while the subsequent components were introduced as uniform layer as shown in Fig. 3.1. The resulting films of 10μm of thickness and 1.61 cm^2 of active area were stored in a nitrogen-filled glovebox and not exposed to light prior to photoelectrochemical (PEC) characterization.
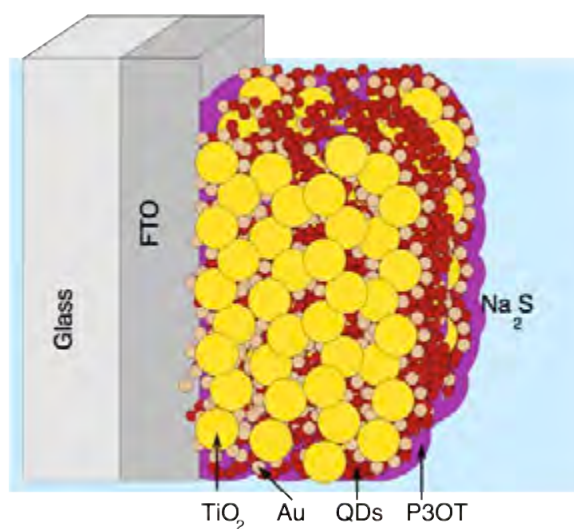
Fig. 3.1. Schematic representation of TiO$_2$ NCs/Au NPs/CdSe QDs/ P3OT film.

3.2. Optical Properties

The absorption of the TiO$_2$ NC film decorated with the QDs, Au NPs, and P3OT was likewise studied, and Fig. 3.2 shows the absorption spectrum of the composite film TiO$_2$/Au/QDs/P3OT. It presents two well-defined bands corresponding to TiO$_2$ NCs (338 nm) and CdSe QDs (552 nm). The slope from 400 to 550 nm is attributed to combined absorption from P3OT and QDs, and the absorption between the 600 to 700 nm was observed in all Au NPs-decorated films. This long red-shifted absorption tail confirms the presence of Au NPs and suggests possible agglomeration during the film deposition. When agglomeration occurs, the absorption band becomes characteristically weaker and broader. Thus, the slope

31

from 400 to 550 nm also contains the absorption of Au NPs.
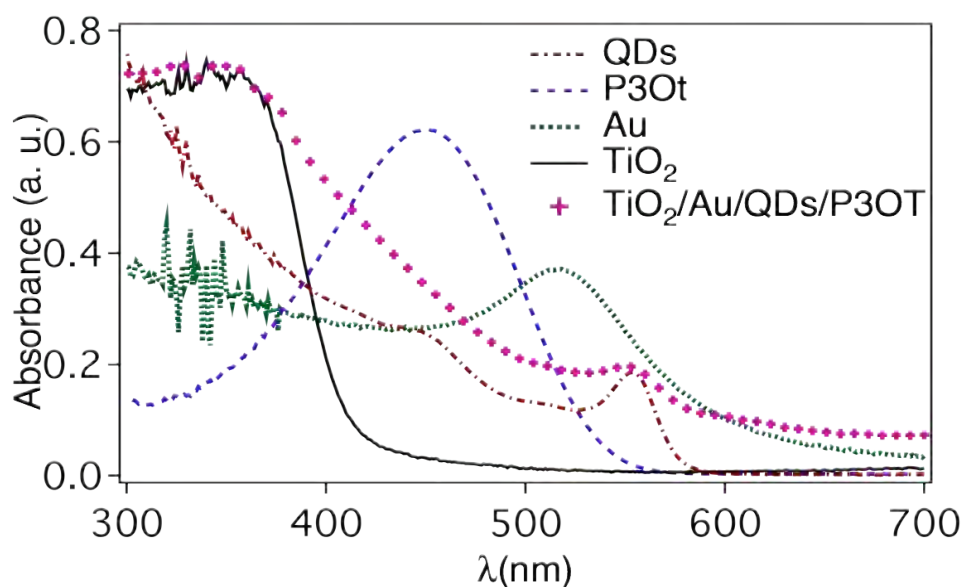
Fig. 3.2. Absorption spectra of Au NPs, P3OT, CdSe QDs, TiO_2 NCs, and TiO_2/Au/QDs/P3OT film.

3.3. Photovoltaic Evaluation

Electrochemical measurements as in the last chapter, were made in a three-electrode cell using the sample as the working electrode which was illuminated with 31.83 mW/cm^2 from a halogen lamp. A saturated calomel electrode (SCE) was used as the reference electrode, while a platinum (Pt) wire was used as the counter-electrode and sodium sulfate (Na_2S) as electrolyte see Fig. 3.3.
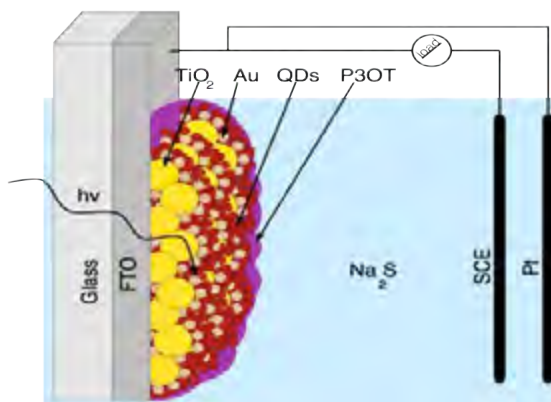
Fig. 3.3. Schematic representation of TiO$_2$ NCs/Au NPs/CdSe QDs/ P3OT film for photoelectrochemical characterization.

The current density-voltage (J-V) profiles for TiO$_2$ NC films decorated with Au NPs, QDs, and P3OT fabricated with different configurations were obtained and are shown in Fig. 3.4. Before such characterization, the electrolyte behavior was studied by cyclic voltammetry with platinum as the working electrode, while the oxidation peak at 0.214 V vs SCE was observed. This oxidation voltage was taken as a reference (V = 0) to evaluate all films under study. The measured short-circuit current density (Jsc) and open-circuit voltage (Voc) are summarized in Table 3.1. The fill factor (FF) and photoconversion efficiency (η) were calculated by using Equation 1.5 and Equation 1.6. [84]. All calculated values for different configurations are displayed in Table 3.1. Values reported here are the mean values of 5 samples measured of each configuration, the calculated efficiencies had a relative variation of 5%. The results clearly show that all multi-decorated systems present photocurrent and photoconversion efficiency higher than that observed for the TiO$_2$/QDs film. With the introduction of Au NPs and P3OT, the photocurrent increases by ~ 85% and ~150%, while the photoconversion efficiency increases by ~167% and ~177%. The improvement demonstrates the importance of using properly configured material architectures (TiO$_2$/QDs/Au and TiO$_2$/QDs/P3OT). The enhancement with the introduction of Au NPs is a little higher than that reported recently by the Zhang group, which was obtained using a different configuration involving blending of TiO$_2$ NC, Au NPs, and CdSe QDs in large colloidal spheres (2.5 times at 1 sun) [64]. The different photocurrent and similar photoconversion efficiencies in our experimental results suggests a stronger effect on FF of Au NPs than P3OT, as confirmed by the calculated data shown in Table 3.1. As the FF parameter is related with the ratio of charge carriers extracted from the device to those photogenerated in the active material, an increase in FF indicates an increase of the transport efficiency caused by either a reduction of the leak current or a reduction in electron flux resistance. Thus, Au NPs enhance

charge separation and transport and reduce charge recombination, which is in good agreement with results reported by others. [67]

P3OT enhances the photocurrent by contributing to the electron injection as well as hole transport. Therefore, one may expect an increase in photoconversion efficiency when Au NPs and P3OT are used in conjunction. Indeed, the highest FF (38.1%) was obtained from the TiO_2/Au/QD/P3OT configuration that represents an increase of ~95% compared to that obtained for TiO_2/QDs film (19.5%). Such a configuration shows an increase of photocurrent of ~285% (906 μA), resulting in an increment of ~600% on the photo- conversion efficiency (0.661%). This strong enhancement is a result of the synergistic effect of the combined use of both P3OT and Au NPs. Detailed analysis of each configuration will be performed and described later.
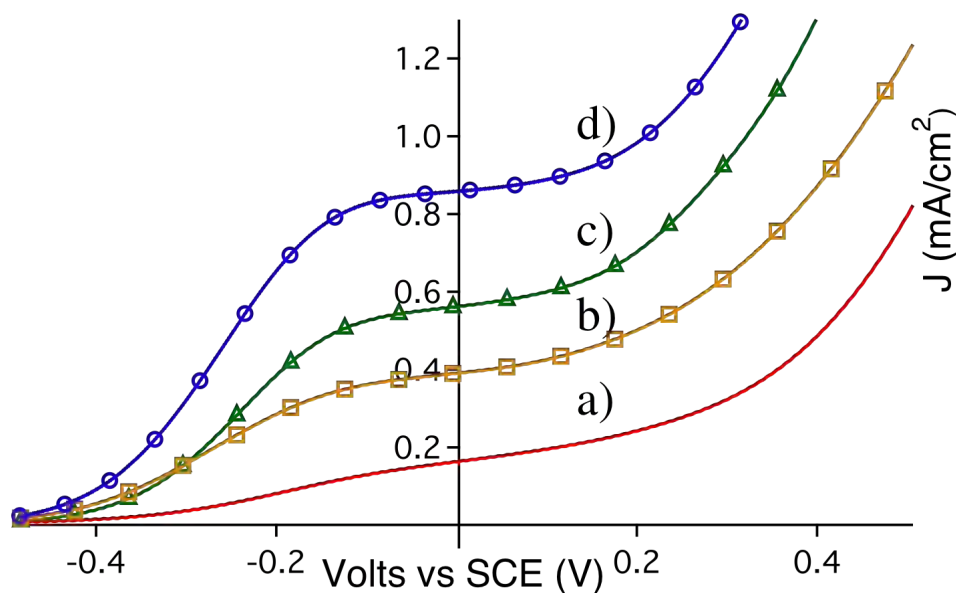
Fig. 3.4. Characteristic J-V curve of TiO_2 NCs films decorated with a) CdSe QDs, b) CdSe QDs/Au NPs, c) P3OT/CdSe QDs/Au NPs, and d) Au NPs/CdSe QDs/P3OT. Measurements were performed in a three-electrode cell, using a saturated calomel electrode as a reference, Pt as a counter electrode the sample

under study as a work electrode, and Na2S as electrolyte using the measured oxidation potential 0.214 V Vs SCE. A halogen lamp with 31.83 mW/cm2 was used for illumination.

Table 3.1. Photocurrent (Jsc) measured at 0.214 V vs SCE, photovoltage (Voc), fill factor (FF), and photoconversion efficiency (η) of multi-decorated TiO_2 films under 31.83 mW/cm2 of Light Intensity.

Sample	Jsc µA/cm2	Voc mV	FF %	η %
TiO$_2$/QDs	236	675	19.5	0.098
TiO$_2$/QDs/P3OT	584	631	23.5	0.272
TiO$_2$/P3OT/QDs	503	637	20.3	0.206
TiO$_2$/QDs/Au	437	597	32.1	0.262
TiO$_2$/Au/QDs	401	531	28.9	0.194
TiO$_2$/QDs/Au/P3OT	260	526	28.1	0.120
TiO$_2$/P3OT/QDs/Au	609	601	34.3	0.394
TiO$_2$/Au/QDs/P3OT	906	610	38.1	0.661

To understand the contribution of CdSe QDs, Au NPs and P3OT in the photocurrent the QE for TiO$_2$/QDs, TiO$_2$/Au/QDs, and TiO$_2$/Au/QDs/P3OT films were calculated with Equation 1.12 (Fig. 3.5). All samples have a peak around 365 nm, attributed to the strong photoabsorption of TiO$_2$ NCs (Fig. 3.2), combined with the absorption of FTO (360 nm). For the TiO$_2$/QDs film, the QE starts to increase at 590 nm a shoulders at 512 nm and a, that corresponds to the absorption of CdSe QDs (Fig. 3.5 a).
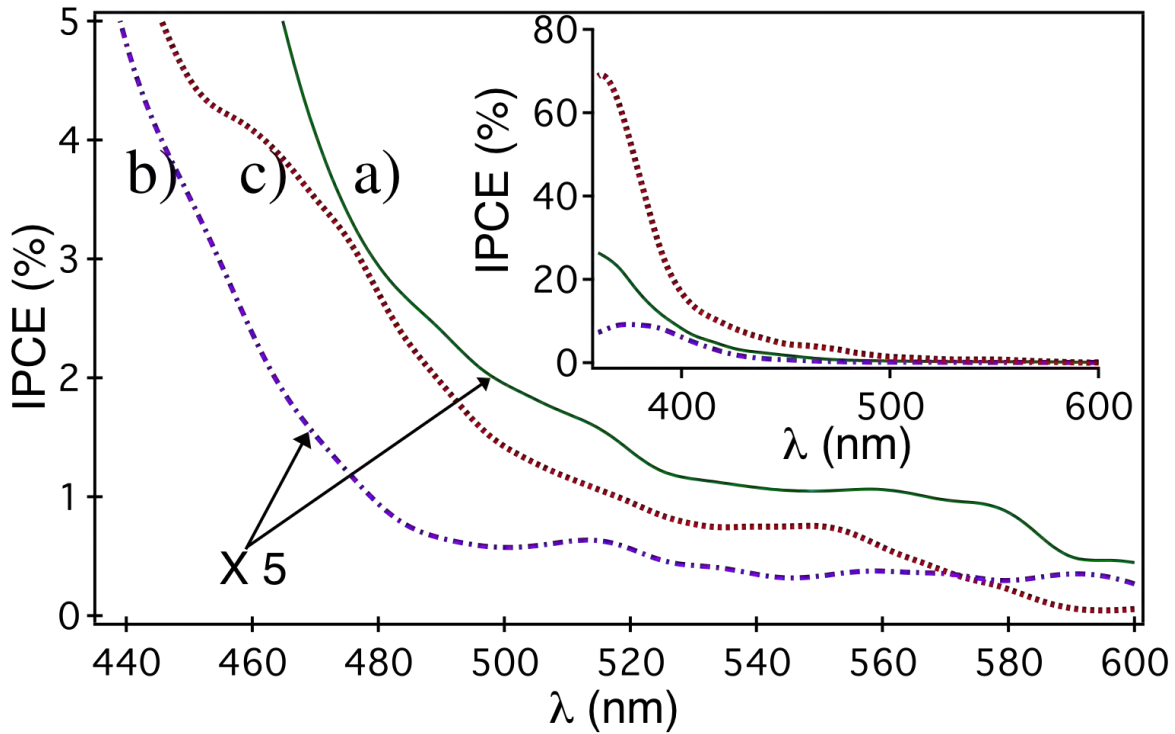
Fig. 3.5. Incident photon to current conversion efficiency (IPCE) determined from the photocurrent at different excitation wavelength and by using eq 1.12, for different configuration. a) TiO_2 NCs/CdSe QDs, b) TiO_2 NCs/Au NPs/CdSe QDs, and c) TiO_2 NCs/Au NPs/CdSe QDs/P3OT. Inset shows a zoom-out of the same samples. Notice that curve a and b are amplified 5X for visualization purpose**.**

The TiO_2/Au/QDs film showed reduced IPCE (Fig. 3.5 b), down to about a third of that obtained for the TiO_2/ QDs film, with bands at 365 nm associated with TiO_2, 518 nm associated with Au NPs, and a weak band at 550 nm associated with the QDs. The enhancement of the band at 518 nm suggests a possible photosensitization role due to the Au NPs, in agreement with results reported by Tian et al [68,72]. However, the observed decrease in the QE values is likely the result of dominant trapped photogenerated electrons as suggested previously [67], [70] as well as light scattering which reduces the excitation of QDs. The photosensitizer or electron trapping effect dominance depends on the interaction between TiO_2 and Au NPs as suggested recently, [64] which, in turn, is dependent

36

on the film and linking mechanism between both nanoparticles. Thus, the photosensitizing effect observed in our case suggests a strong interaction between TiO_2 and Au NPs and contributes to the electron injection, while the dominant electron trapping effect helps to separate the photogenerated charges, improving the interfacial charge transfer. The combined effects result in an increase of overall conversion efficiency. A 680% increase of QE was observed for films prepared with the TiO_2/Au/QDs/P3OT configuration, as compared to that of the TiO_2/QDs film. The IPCE plot shows a well-defined broad band from 455 to 480 nm that could be attributed to P3OT, confirming its contribution to the photocurrent generation directly by absorbing light. Additionally, an enhanced band associated with QDs confirming the role of P3OT in the hole regeneration and a weak band associated with Au NPs was observed at 518 nm. Therefore, the strong increase of IPCE from 580 nm to the UV confirms the synergistic effect, especially considering the enhancement is larger than the addition of contribution of each component in the composite. The relatively low IPCE values can be attributed to the fact that most of the important parameters were not yet optimized, such as electrons and holes trapped at the interface, internal and surface defects of each component that promote recombination, light scattering, etc. The electron scavenging by the remnant O_2 in the electrolyte could also partially contribute to the reduced IPCE.

3.4. Discussion

With the results described above, it is possible to gain a better understanding of the physical mechanism involved in the photo-conversion efficiency for each configuration under study. Among all the composite films studied here, the TiO_2/QDs films show the lowest photoconversion efficiency (0.098%). This is still higher than that obtained for pristine TiO_2 due to the QD's ability to photosensitize TiO_2. [54] In the TiO_2/QDs film, photo-generated electrons in the conduction band (B_c) of the CdSe QDs are injected into the B_c of TiO_2 NCs due to the energy difference between their band edges, as shown in Fig. 3.6a. Once in the B_c of TiO_2, electrons can be transported to the FTO substrate. However, QDs have significant

37

electron losses mediated by electron-hole radiative and nonradiative recombination processes [85], which limit the FF to 19.5%.

An increase of photocurrent (584 µA/cm2) and FF (23.5%) was observed with the addition of P3OT to form the TiO_2/QDs/ P3OT configuration, although the FF parameter is still small in comparison to other configurations studied here. The increase in photocurrent is attributed to the photoabsorption of P3OT that has a broad absorption band and acts to complement the absorption of CdSe QDs. When relevant energy levels are considered, as shown in Fig 3.6b, it is likely that electrons which are photogenerated in P3OT are first injected to QDs because of the energy difference between the LUMO of P3OT and B_c edge of the CdSe QDs. These electrons are subsequently transported and injected, along with electrons directly photo-generated in the CdSe QDs, to TiO_2 NCs and then to the FTO substrate. However, not all electrons generated contribute to the photocurrent. In fact, a limitation with this configuration is the inefficient electron injection of QDs due to significant surface recombination that explains the relative low value of FF. Nevertheless, holes in QDs in this configuration are injected to P3OT (and then filled by oxidizing the electrolyte), improving the electron injection as confirmed by the small increment of FF. When the order of sensitizer is switched to have the TiO_2/ P3OT/QDs configuration, the photocurrent (503 $\mu A/cm^2$) and FF (20.3%) were found to be lower than those obtained from TiO_2/QDs/P3OT. Such a reduction is because many electrons generated in QDs do not reach the TiO_2 effectively due to the LUMO energy level of P3OT being higher than B_c edge of QDs, as shown in Fig. 3.6c. An additional reason is from the reduction of the QD absorption, considering that irradiation was first absorbed by P3OT. Therefore, the increase of photocurrent and conversion efficiency (0.272%) areis likely a result of contribution of electron injection from P3OT, and the reduction of photocurrent, FF, and photoconversion efficiency (0.206%) is possible due to reduced contribution from QDs.

The addition of Au NPs instead of P3OT in TiO_2/QDs/Au configuration increases the FF to 32.1%. This is the result of improved hole injection from the

QDs to the electrolyte due to the better conduction properties of Au NPs (Fig 3.6d). Au NPs likely improved the regeneration rate of QDs that in turn increase the photoabsorption and photocurrent in comparison to TiO_2/QDs films. This increase is strong enough to give a conversion efficiency of 0.262%, similar to that obtained with P3OT (Table 3.1). However, the photocurrent is relatively low for this configuration (437 µA/cm2) compared to the sample using P3OT because Au NPs, unlike P3OT, do not contribute to the photogeneration process. Furthermore, a stronger decrease in photocurrent (401 µA/cm2), FF (28.9%), and photoconversion efficiency (0.194%) was observed when Au NPs were placed between TiO_2 and QDs to form the TiO_2/Au/QDs configuration (Table 3.1, Fig3.6e). In this case, electron injection from QDs to TiO_2 may be reduced due to the electron trap and the scattering of incident light by Au NPs, as indicated by the IPCE results discussed above. Overall, the FF obtained with the introduction of Au NPs is higher than that obtained with bare TiO_2/QDs and with P3OT in any configuration. This is explained by the ability of Au NPs to extract electrons from QDs and inject it into TiO_2 electrode and is in good agreement with results recently reported. [86]

In summary, the use of P3OT contributed substantially to increasing the photogeneration of charge carriers but maintained a relatively low FF due to the low electron injection efficiency. The use of Au NPs improves the electron injection rate, resulting in a higher FF but does not contribute (or contribute in a minor proportion) to the photogeneration of charge carriers and may actually reduce it somewhat due to electron trapping and scattering of the incident light. The combination of Au NPs and P3OT in the right configuration was found to improve the photoconversion efficiency by enhancing the FF as well as the photocurrent. When Au NPs are linked between QDs and P3OT (TiO_2/QDs/Au/P3OT), a strong reduction of photocurrent (260 µA/cm^2) and photoconversion efficiency (0.12%) was observed compared to TiO_2/QDs/Au and TiO_2/QDs/P3OT films. This configuration can be visualized as a couple of cells with opposite electron flux. In this case, QDs and P3OT photogenerate charge carriers in a similar way to that in the TiO_2/QDs/ P3OT configuration, but Au NPs act as a charge sink capturing

holes from both sides, as shown in Fig. 3.6f. Furthermore, the low conversion efficiency suggests a low flux of electrons through TiO_2 as a result of reduced QDs regeneration. In addition, the excess of holes in Au NPs induces oxidation, as has been reported previously, [70] changing its role to a charge sink. A strong increase of photocurrent (609 µA/cm2) and FF (34.3%) was observed with the configuration of TiO_2/P3OT/QDs/Au. In this case, the photoconversion efficiency (0.394%) represents an increase of ~91% when compared to similar configuration but without Au NPs. The enhancement is attributed to the improvement of QDs regeneration by Au NPs. However, QDs are not used in its optimal efficiency because their B_c edge is lower than that of P3OT (Fig. 3.6g). Thus, the limitation of this configuration is that P3OT is not a good electron conductor and QDs are not good hole conductor resulting in a resistance to the charge carriers flux and low performance of the configuration.

The strongest improvement of both photocurrent (906 µA/ cm^2) and FF (38%) was obtained with the TiO_2/Au/QDs/ P3OT configuration (Figure 3.6h), taking advantage of the positive characteristics of each component. This configuration shows a photoconversion efficiency of 0.661%, which represents an increase of ~600% when compared with samples sensitized only with QDs. In this configuration, P3OT absorbs part of the incident light and photogenerates electrons that can be efficiently injected into the B_c of the QDs and then to TiO_2. Moreover, P3OT is very efficient in transporting holes from QDs to the electrolyte, facilitating its regeneration that should increase overall photoabsorption. Meanwhile, Au NPs improve the charge carrier transport, electrons from QDs, resulting in a strong improvement of photocurrent. When all is combined, this produces a system with optimal energy levels for efficient charge carrier generation, transfer, and transport and thereby high overall photoconversion efficiency.
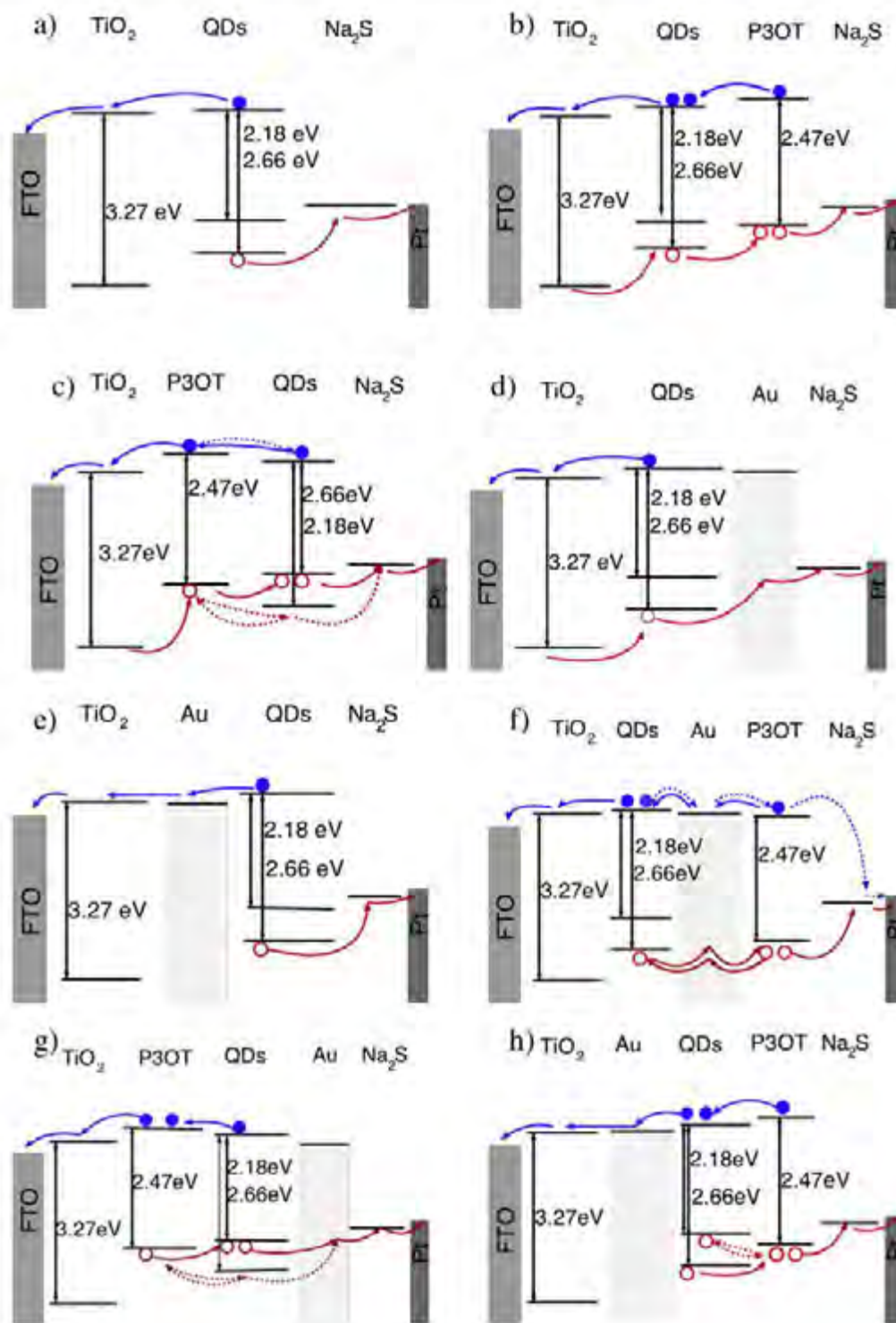
40

Fig. 3.6 Schematic representation of the energy levels in different configurations of sensitized TiO2 films. Blue and redlines indicate possible paths of electron and holes, respectively.

According to IPCE results, Au NPs strongly affect the photoabsorption of QDs due to the electron trapping effect and light scattering. However, FF indicates that Au NPs considerably reduce the energy losses in the electrons transport, resulting in an increase of photoconversion efficiency. This effect was confirmed by evaluating the conversion efficiency for a different concentration of Au NPs on the TiO_2/Au films. Experimental results show an increase of photoconversion efficiency with the increase of Au NPs loading, 0.074%, 0.096%, and 0.104% for 0.26×10^{14}, 0.52×10^{14}, and 1.04×10^{14} nanoparticles/mL, respectively. The gain in photocurrent is attributed to the high conductivity of Au NPs, allowing a better electric contact between TiO_2 and the electrolyte. Higher concentration of Au NPs covers more efficiently the TiO_2 surface and enhances the electric contact.

3.5. Conclusions

The photovoltaic properties of CdSe QD-sensitized TiO_2 NC films decorated with Au NPs and P3OT in different configurations have been systematically studied and analyzed. It was demonstrated that all multidecorated systems show higher photoconversion efficiency than TiO_2/CdSe QDs or TiO_2/Au NPs. The presence of Au NPs improves the charge separation and thereby photocurrent generation. The introduction of P3OT contributes to electron injection as well as to hole transport. Most significantly, the combined use of Au NPs and P3OT synergistically improves the photoconversion efficiency. The strong enhancement of ~285% on J_{sc} and ~600% on photoconversion efficiency with the optimum configuration of TiO_2/Au/QDs/P3OT being the result of the fast electron extraction by Au NPs from QDs and the electron injection from P3OT accompanied with hole conduction. The composite systems based on CdSe QDs, Au NPs, P3OT, and TiO_2 NCs, when constructed in the appropriate configuration, have been demonstrated to be promising for photovoltaic and possibly other optoelectronics applications. However, the optimal configuration reported here can be improved to increase IPCE and photoconversion efficiency in order to make such configuration more reliable for practical applications.

Chapter 4.
Impedance Modeling

One of the motivations in photovoltaic (PV) cell studies is to understand the processes involved in the charge carrier transport inside the cell [87-90]. The semiconductor/electrolyte interface extends to the entire film volume, implying that transport, reaction, and polarization processes occurring throughout the porous structure of the film are coupled in an intricate manner [88]. Electrochemical impedance spectroscopy (EIS) is an excellent and well-established technique for characterizing electrochemical systems, most notably for those involving a number of coupled processes [88,89,91-93]. EIS can identify important parameters affecting the cell performance, such as: (i) electron transport in the TiO_2, which is influenced by the free carrier density and electron mobility, the latter being likely dependent on the carrier density, as the electron motion is a trap limited process [88,94-98]. (ii) Transfer of electrons to redox species in the electrolyte (sometimes named *recombination* or *back reaction* process in the context of DSSC studies). (iii) Charging of the contact on the transparent conducting substrate (TCS) with the electrolyte (provided that the electrolyte penetrates the porous structure up to the substrate). (iv) Charging of capacitive elements in the high surface area porous structure, including the Helmholtz capacitance in the TiO_2/electrolyte interface and the capacitances related to filling the conduction band and surface states of the TiO_2 in the porous structure [88,99]. In addition, the lifetime, the diffusion coefficient, and the diffusion length could be obtained [91].

The EIS experimental measurements are relatively simple to make, however the correct interpretation of these measurements requires the use of a suitable model. In the case of sensitized solar cells, the structure is a complex network of interconnected TiO_2 NCs deposited on a transparent conducting oxide (TCO), with sensitizers and a redox electrolyte. Due to this complexity, impedance models

published so far to describe the behavior of the sensitized solar cell are restricted to certain working conditions [100] or applied only to separate parts of the cell [89,101,102].

In the previus chapter it was described how the addition of Au NPs to CdSe QDs sensitized TiO_2 increases the efficiency of the cells by augmenting the FF suggesting that Au NPs improve the electron transport, while P3OT increases the photocurrent and FF, indicating that the polymer contributes with the photogeneration and helps to the hole transport (see Fig. 4.1). To have a more detailed comprehension of the internal charge carrier process of the multi-sensitized cells, EIS studies of TiO_2 films sensitized with CdSe QDs with and without further decoration of Au NPs and/or P3OT have been carried out. An improved model has been proposed to explain the experimental results and to better understand the charge transport processes across the interfaces of the different components of the films. Impedance analysis suggests that part of the increment in efficiency observed in TiO_2/Au/QDs/P3OT films is due to a reduction in the resistance to electron flux between QDs and TiO_2 due to the presence of Au NPs. Meanwhile, P3OT promotes hole regeneration and reduces electron recombination.
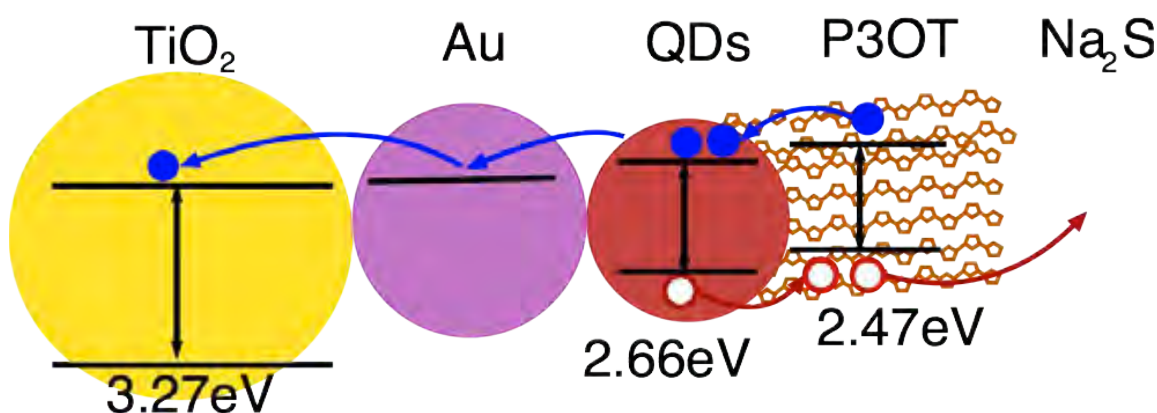

Fig. 4.1. Schematic representation of the electron and hole flux in TiO2/Au/QDs/P3OT films

4.1. Electrochemical Impedance Spectroscopy

Electrochemical impedance spectroscopy (EIS) measurements were done in dark conditions applying a sinusoidal voltage of ±10 mV from the equilibrium potential, varying the sinusoidal frequency from 1×10^5 to 1×10^{-2} Hz. EIS measurements were fitted with Boukamp Equivalent Circuit software. Figure 4.2 shows the Nyquist and Bode experimental curves of TiO_2/QDs, TiO_2/Au/QDs and TiO_2/Au/QDs/P3OT films. The introduction of Au NPs between TiO_2 NCs and CdSe QDs strongly reduces the impedance, and the addition of P3OT slightly raises the impedance, as is observed in Fig. 4.2a. Module curves in Bode diagram indicate that the stronger reduction in the impedance when Au NPs were added is located in the middle to low frequency region (≤10 Hz), commonly associated with transport processes [89] (see Fig. 4.2b). Meanwhile, the high frequency impedance is almost not affected. An increase in the low frequency region impedance was observed after the addition of P3OT to TiO_2/Au/QDs films, not as high as in TiO_2/QDs films. However, the high frequency impedance in TiO_2/Au/QDs/P3OT films is slightly higher than the other ones. The low frequency region is influenced by a combination of capacitive an resistance processes that are associated with the electron interaction in the material boundaries [89,91,99,103]. On the other hand, the high frequency region is determined by linear resistances commonly associated with the transport processes inside of the materials [87,89,91]. Therefore, Au NPs likely reduce the resistance to interfacial electron flux without significantly affecting the internal transport resistance, while P3OT increases the resistance to boundary injection processes and the resistance to the electron transport inside of the film.
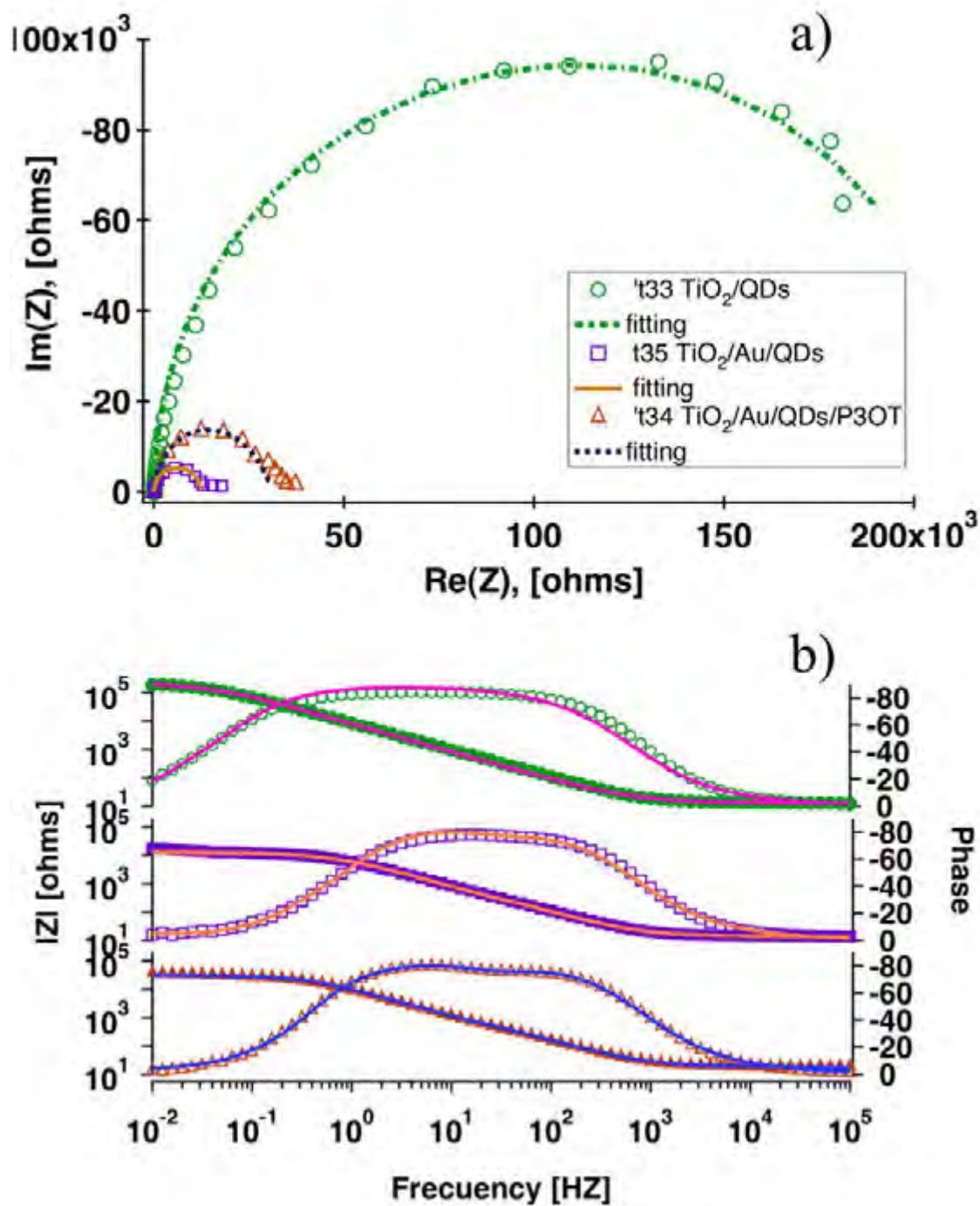
Fig. 4.2. Niquist (a) and Bode (b) representation of the impedance for each film under study showing module (filled), phase (emtpy). Fittings with the correspondent equivalent circuit by using the proposed extended model are shown in solid lines.

4.2. Circuit 1

In all cases, Au NPs reduce the resistance to the electron transport in the interface; meanwhile, P3OT increases such resistance. However, these systems are composed of several interfaces between the electrolyte, the sensitizers, and TiO_2. To better design solar cells, it is important to understand how electron flux is affected by each component of the film. Equivalent circuits allow obtaining a better interpretation of the impedance separating the resistance in components that could be associated to the individual processes in the film. As a first approximation, the circuit described in Fig. 4.3 with only three elements was used to fit the impedance response of the tree types of devices. Where R_1 is the electron transport resistance, R_2 is the charge transfer resistance in the film/electrolyte interface and C_2 is the chemical capacitance which consist in a constant phase element with exponent ß i.e. ($C_2 = Z_{c2}^{-1}(i\omega)^{\text{ß}}$). The fitted results are shown in Table 4.1 where ß takes values between 0.96 and 1 indicating a very low frequency dispersion, and therefore it may be considered as almost an ideal capacitor [88]. W represents the Warburg impedance, associated with diffusion processes in the electrolyte species.

Fig. 4.3. Equivalent circuit with only three elements (R_1, R_2, C_2) used to fit the impedance measurements of multidecorated film.

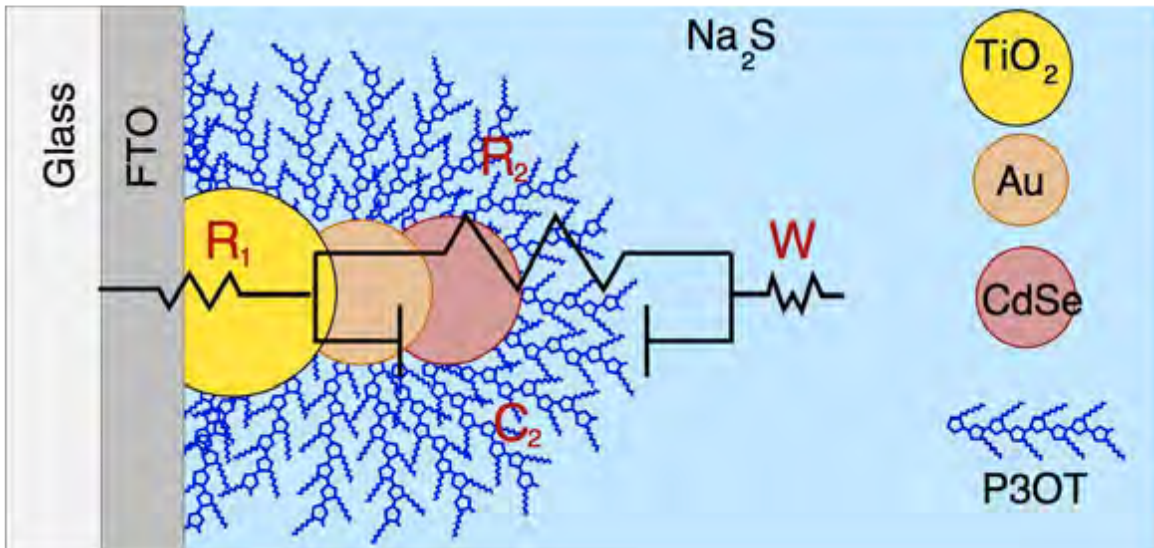The calculated resistance indicates that R_1 is almost not affected by the addition of Au NPs and P3OT. In contrast, the addition of P3OT increases the charge transfer resistance (R_2=33.4 KΩ), indicating a reduction in the electron leakage, consistent with the FF behavior. However, a reduction in the charge transfer resistance (R_2=15.3KΩ) was obtained when Au NPs are added. This change should be reflected in a reduction of the FF, which is not observed. This suggests that a more detailed analysis is needed as discussed below.

Table 4.1 Resistances and capacitance obtained by fitting the impedances with the equivalent, circuit with only three elements, see Fig. circ1.

Sample	R_1 (Ω)	R_2 (KΩ)	C_2 (µF)
TiO_2/QDs	13	215	12.6
TiO_2/Au/QDs	14	15.3	15.9
TiO_2/Au/QDs/P3OT	15	33.4	11.1

Effective electron transfer time in the film/electrolyte interface could be calculated as the capacitor discharge time (τ_{ct}) as a function of a pair Resistance-Capacitor (R_{ct},C_{ct}). The discharge time was calculated by using the expression $R_2 \times C_2$ and the circuit values listed in Table 4.1, as plotted in Fig. 4.4. It is observed that the addition of Au NPs and P3OT reduces the discharge time of the conduction band of the film, although with P3OT the discharge time of the conduction band is slightly higher than that for Au NPs. Such difference indicates that Au NPs increase the leakage process while P3OT reduces it. However, FF and η increase with the addition of Au NPs, suggesting there is still contributions unaccounted for by the model suggesting that a more detailed model is still necessary.
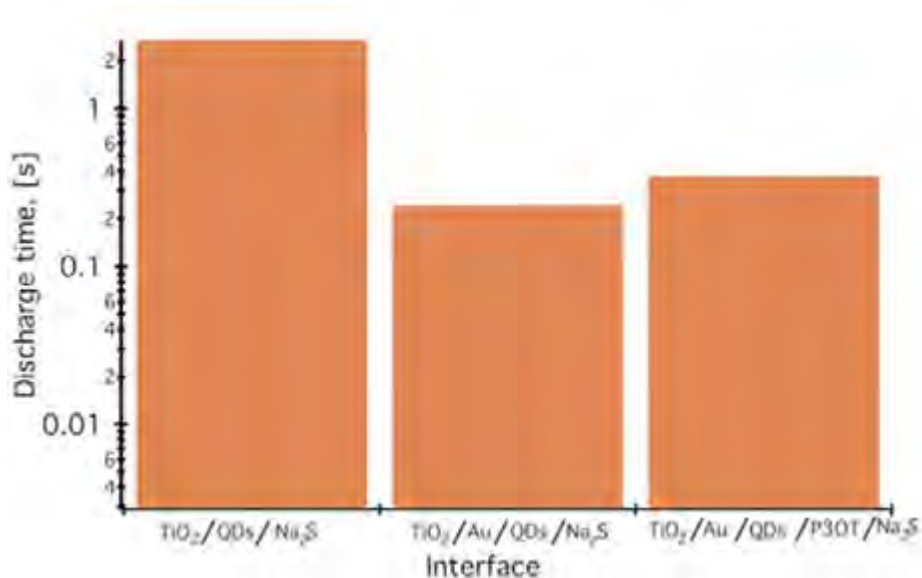
Fig. 4.4. Discharge time of the film conduction band calculated from the Rj, Cj values displayed in Table 2 and obtained from the proposed equivalent circuit with only three components.

4.3. Circuit 2

To elaborate a more appropriate model, the impedance phase (Fig. 4.2b) was analyzed and it was found that such curve for TiO_2/QDs could be described as the sum of two Gaussian curves, indicating two capacitance regions. In $TiO_2/Au/QDs$ films, impedance phase has some structural variations that indicate the presence of three capacitance regions, and four capacitance regions for $TiO_2/Au/QDs/P3OT$. As was discussed above, capacitance regions are related to interfacial processes, suggesting that when a sensitizer is added two new capacitances (interfaces) must be considered. Thus, our proposed basic model with only one capacitance must be expanded. The resulting circuits for each configuration are shown in Fig. 4.5 where R_1 is the sum of series resistance of the film and is associated with the resistance to the electron flux inside of the NPs and inside FTO. R_2 and C_2 are the resistance and capacitance associated with the electron transfer from the sensitizers to TiO_2. R_5 and C_5 are associated to the electron transfer between the film and the

electrolyte. In a similar manner, R_3 and R_4 with their respective capacitances represent the transfer processes in the Au/QDs and QDs/P3OT interfaces, respectively (when they exist). Experimental data of impedance for each configuration were fitted with these proposed equivalent circuits showing a very high accuracy (>95%) in both Niquist and Bode representations as are shown in solid lines in Fig. 4.2.

Fig. 4.5. Schematic representation of proposed extended equivalent circuit for each configuration under study.
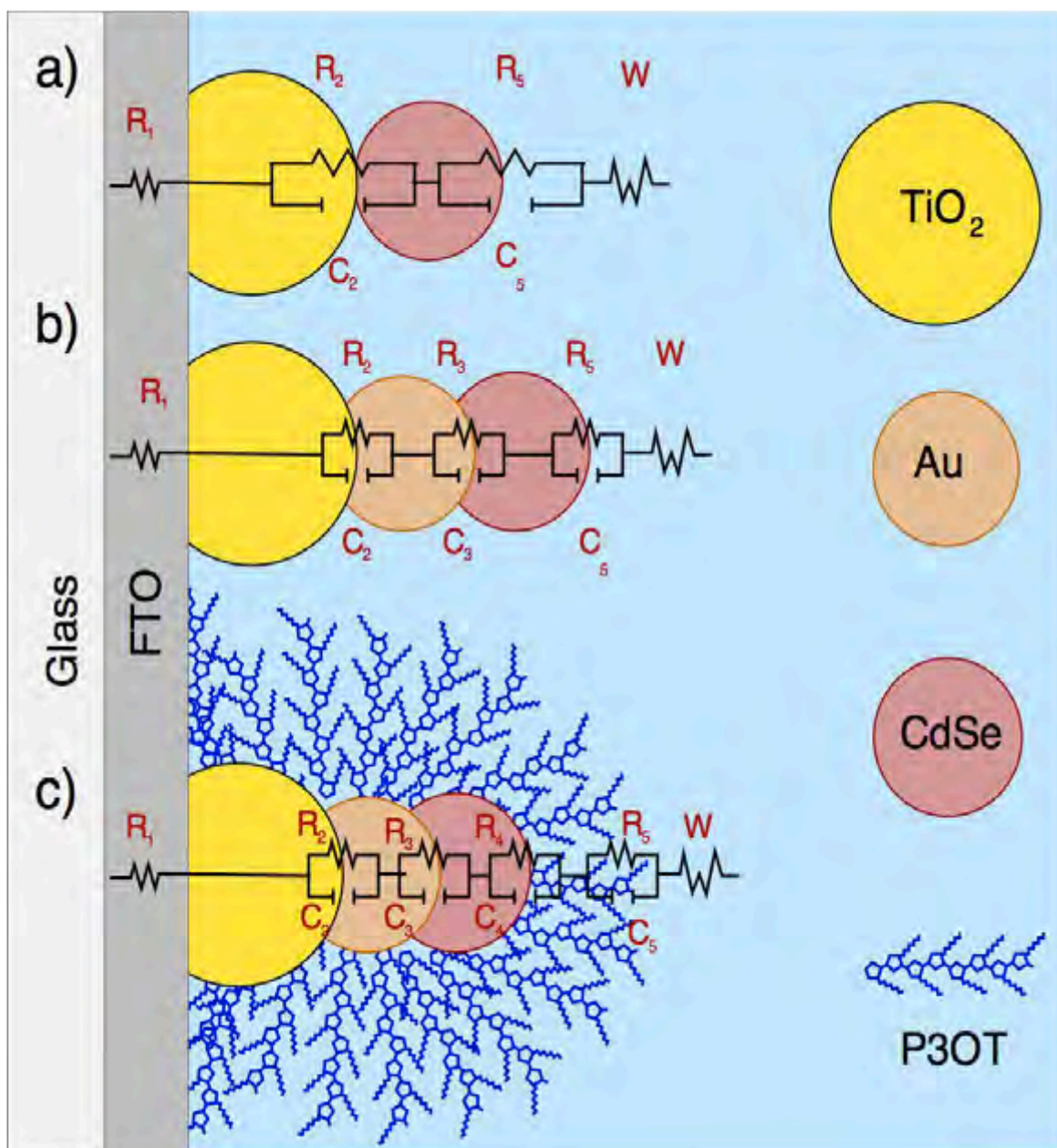
51

The resistance and capacitance values were obtained from extended models proposed for each configuration. TiO_2/QDs films have a high resistance to the electron flux, R_2=85.9 KΩ, in both interfaces between TiO_2/QDs and R_5=128 KΩ between film/electrolyte. The former indicates that electron flux from QDs (where they are generated) to TiO_2 is restricted, getting low FF values and consequently low η. However, R_5 indicates a low recombination process that improves the final η of such device. When Au NPs were added to obtain TiO_2/Au/QDs configuration, a general reduction of the resistances was observed, especially at the TiO_2/Au interface where R_2=47 Ω. Meanwhile, the resistance in the Au/QDs interface is higher R_3=6.18 kΩ, probably produced by de resistive properties of the QD's surface. It is important to note that the resistance to electron injection from QDs to TiO_2 across Au NPs is lower than from QDs to TiO_2 in TiO_2/QDs films, which explains the FF increase. Furthermore, the resistance in the film/electrolyte interface is also reduced (R_5 =5.6 KΩ), which could indicate the generation of a leakage zone in the Au NPs as will be discussed later. A general increase in the resistances was observed with the addition of P3OT, with the exception of the film/electrolyte interface resistance (R_5=3.78 kΩ). However, the resistance at this interface is higher than that of the QD/P3OT interface (R_4=232Ω), while the Au/QDs interface resistance (R_3=25.4KΩ) is still higher than that of the TiO_2/Au interface (R_2=111Ω), indicating a favorable electron flux from P3OT to TiO_2 except for the Au/QDs interface [87].

The discharge times (τ_j=R_j×C_j) of each capacitor were calculated and are listed in Table 4.2 and plotted in Fig. 4.6. For the proposed models in Fig. 4.5, the discharge times are associated with the transfer rate at each interface. As expected, the higher response times were obtained for TiO_2/QDs films as observed in Fig. 4.6. It is observed that discharge time from QDs to electrolyte (7.49 s) is higher than QDs to TiO_2 (2.55 s), producing a gradient of electron concentration inside QDs that facilitates the electron transfer to TiO_2. All response times were reduced after the addition of Au NPs as observed in Fig. 4.6. The results show a relatively long discharge time from QDs to the electrolyte (489 ms), a fast injection

rate from QDs to Au NPs (173 ms) and even faster electron transfer from Au NPs to TiO$_2$ (3.87 ms), resulting on an increase in the final efficiency. Notice the considerably reduced value of τ_5 after the addition of Au NPs, this is probably because the electrolyte permeates deeply in the film and some electrons leak in the Au/electrolyte interface resulting in a reduction in the average film/electrolyte discharge time.

Table 4.2. Injection time calculated from R_j and C_j values obtained from the proposed extended equivalent circuit components, see Fig. 4.5.

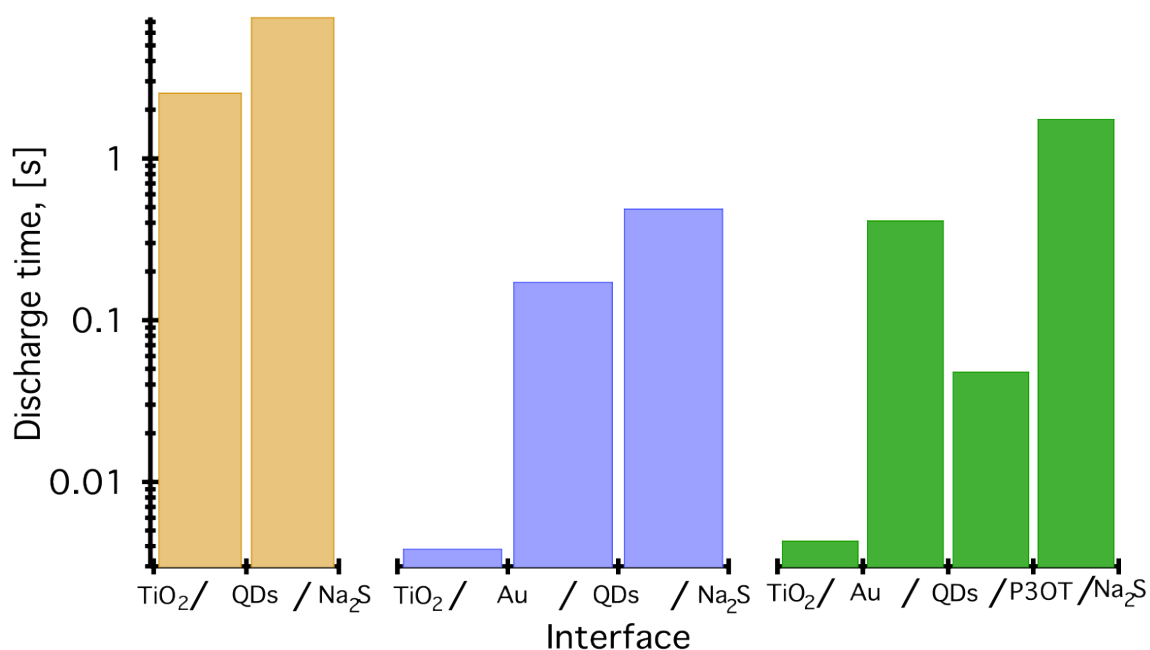| Sample	τ_2 TiO$_2$/... (s)	τ_3 Au/QDs (s)	τ_4 QDs/P3OT (s)	τ_5 .../Na$_2$S (s)	τ_5/τ_2
TiO$_2$/QDs	2.55	--	--	7.469	2.92
TiO$_2$/Au/QDs	3.87×10^{-03}	0.173	--	0.489	126.35
TiO$_2$/Au/QDs/P3OT	4.32×10^{-03}	0.413	0.048	1.760	407.41

Fig. 4.6. Calculated discharge time for each interface as a result of the proposed extended equivalent circuit.

When P3OT is added, small increases in $\tau_2 = 4.32$ ms and $\tau_3 = 413$ ms were observed, as can be seen in Fig. 4.6, indicating that the electron transfer rate between QDs and Au NPs, and between Au NPs and TiO$_2$ was reduced. This suggests that some P3OT may have penetrated deeply into the film and consequently some electrons from QDs are transferred to TiO$_2$ via P3OT. P3OT is not as good electron conductor as Au NPs, where the electron transport rate in the interfaces decreases [24,104,105]. The response time associated with the QDs/P3OT is very fast (48 ms), which suggests that the energy levels are coupled facilitating the electron transfer from P3OT to QDs and the hole transfer from QDs to P3OT. Although R$_5$ is decreased in comparison with the same resistance in TiO$_2$/Au/QDs films, the discharge time of film/electrolyte interface is substantially lengthened (1.760 s) due to the high capacitance of these films (C$_5$=466µF). The capacitance is related to the density of states and the surface recombination sites. An increase in the capacitance could indicate passivation of the surface recombination sites [106]. In the TiO$_2$/Au/QDs/P3OT configuration, the response time difference between τ_5 and τ_4 is more pronounced than that between τ_3 and τ_5 for the other two configurations, as shown in Fig. 4.6. This result indicates a high electron concentration gradient inside P3OT, reducing the probability of electron recombination via the electrolyte. Figure 4.5 shows that that injection time for the QDs/P3OT interface is lower than that of the Au/QDs interface, which could limit the electron transfer. Finally, it is important to note that the τ_5/τ_2 ratio is strongly related to the FF (see Table 4.2), confirming that such configuration (TiO$_2$/Au/QDs/P3OT) presents the best performance between electron transport and leakage resistance, giving as a result considerable increase in the device performance described in the previous chapter (600%) and confirming the important contribution of P3OT for reducing the electron leakage [1,4,104,107].

4.4. Conclusions

EIS was used to study the charge transport in TiO_2 films sensitized with QDs and simultaneously decorated or modified with Au NPs and P3OT for solar energy conversion applications. The proposed RC model describes the key features of this complex film and helps to better understand the transport process of electrons between different components of the solar cell that ultimately improves the cell design and performance. It was found that Au NPs in the TiO_2/Au/QDs/P3OT films enhance the electron transfer process between CdSe QDs and TiO_2, resulting in an increase of FF. Furthermore, P3OT acts as a hole conductor, increasing the amount of charge carries collected, and in the meantime also acts as a passivation layer that reduces the surface recombination sites. Such passivation effect, in conjunction with the strong absorption of CdSe QDs and the electron transport process facilitated by Au NPs, resulted in a substantial increase of FF and η. This study demonstrates that a rational design of nanocomposite structures can be promising for light energy conversion applications.

Chapter 5.
Engineering the Photovoltaic Device to Improve Photoconversion Efficiency

In this chapter some techniques will be discussed that allow to increase the performance solar cells by: 1) Improving the quality of the TiO_2 film, depositing 3 types of TiO_2 that provide good electrical contact, give high superficial area and scatter the light. 2) Using an electrolyte which redox potential better reduce the QDs, and a counter electrode that properly catalyzes this electrolyte. 3) Using deposition techniques that allow to sensitize the films with big amounts of high quality QDs.

5.1. Cell Assembling

5.1.1. TiO_2 Deposit

Photoactive films were made with 3 types of TiO_2 to do 3 layers with different aims called: compact layer, transparent layer and scattering layer. All these layers were deposited on clean (tec 15) FTOs by spray pyrolysis and Screen printing as described in what follows.

Compact layer (Spray Pyrolysis):

For the preparation of the first TiO_2 layer, a solution with 12g of Acetylacetone and 12g Titanium isoprpoxide in 16g EtOH was sprayed 3 times on a 400ºC preheated

FTO, using a paint gun at 1 bar of pressure, see Fig. 5.1. Then, the film was sintered at 450ºC by 30 min. Fig. 5.2 shows the SEM and EDS analysis of the FTO prior to the spray pyrolysis deposit (Fig. 5.2 a, b y c) and after (Fig. 5.2 d, e y f). SEM images demonstrate that FTO films have a granular structure with 100nm average grain size, and that spray pyrolysis almost does not affect this morphology. However, EDS mapping shows an uniformly distributed TiO_2 deposit (by the presence of titanium). This means that a very thin (approximately 150 nm) and compact TiO_2 layer was deposited. This layer avoids direct contact of the electrolyte with the FTO, reducing electron leakage from FTO to the electrolyte. This layer also acts as a contact point between FTO and the next TiO_2 layer. Providing in this way not only a better adhesion, but also a better electron transport process from TiO_2 to FTO [108].
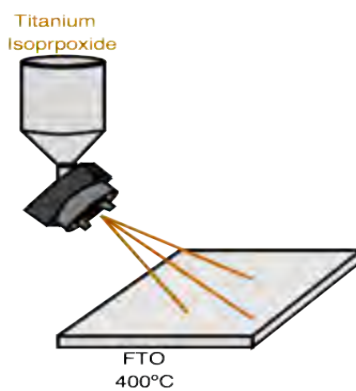
Fig. 5.1. Schematic representation of spray pyrolysis process.

Transparent and scattering layers (Screen Printing):

The deposit of the second layer of TiO_2 was done by screen printing using the 18nr-t dye sol commercial paste and ATMA screen printing machine. The process consists in passing the sample through a microporous mesh at the time this mesh was pressing the substrate (see Fig. 5.3), then the film was dried at 80ºC by 10 min. The film thickness was controlled by the viscosity of the titania paste, the porous size of the mesh and the number of times that the process is repeated. In

this case with 3 repetitions a 6µm film was obtained. According to microscopy analysis (Fig. 5.4a,c), the film particle size is 40nm suggesting a high superficial area. In addition, the films are highly transparent in visible region (80% of transmittance) allowing the adsorption of a big amount of sensitizer [6] and a good light absorption by the sensitizer.
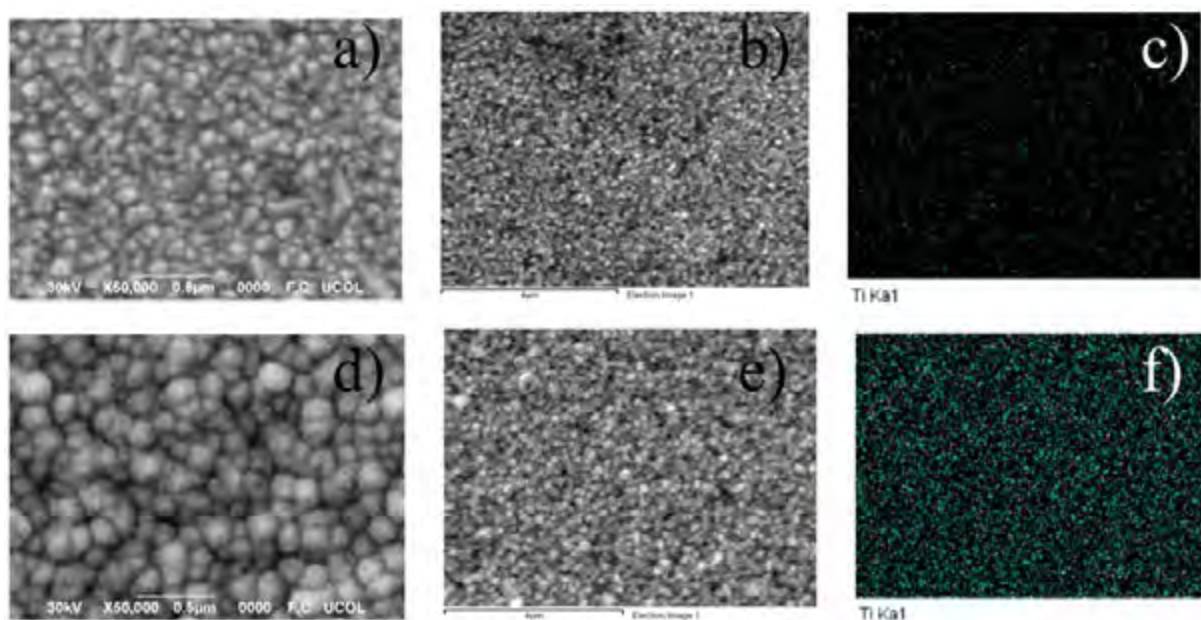
Fig. 5.2. SEM and composition analysis of TiO_2 deposited by spray pyrolysis. a) clean FTO at 50000X, b) FTO at 10000X, c) Titanium EDS mapping of the clean FTO at 10000X, d) TiO_2 compact layer on FTO at 50000X, e) Compact layer at 10000X and f) Titanium EDS mapping of the TiO_2 compact layer on FTO at 10000X

The third layer of the film was done by screen printing two times with the commercial paste Wer2-O of dye-sol obtaining a 4µm opaque layer (Fig. 5.3c). This film consist in 250 nm TiO_2 NPs, see Fig.5.4 b,d, that will scatter the light that pass through the sensitizer in the transparent layer. Scattering provides a second chance to capture light with the sensitizers and increase the final η of the device. Finally, the films were annealed at 400º C for 30 min to remove organic components of the paste and to obtain the anatase crystalline structure.

58
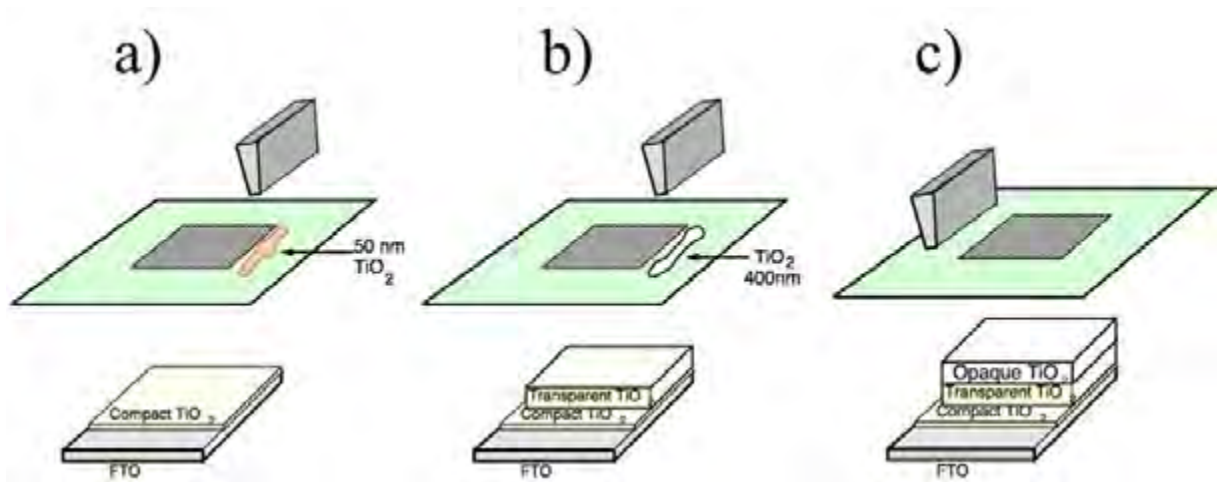
Fig. 5.3. Squematic representation of the Screen Printing process a) before transparent layer deposit, b) before Scattering layer deposit c) final TiO$_2$ film configuration
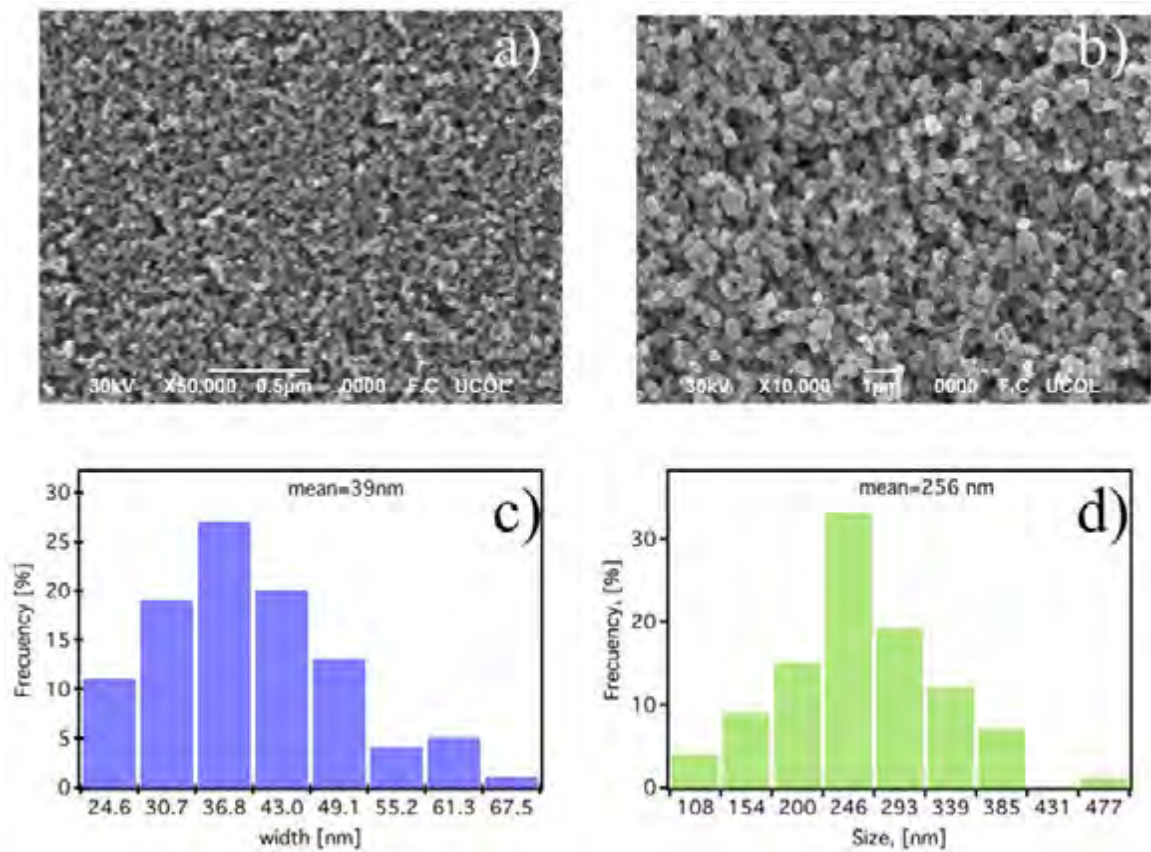
Fig. 5.4. SEM images of a) TiO$_2$ transparent film and b) TiO$_2$ scattering film. And the particle size distribution of the c) transparent and d) scattering films.

5.1.2. Electrolyte & Counter electrode

The electrolyte used in these cells was polysulfide, which consists in a solution of 1M Na$_2$S:9H$_2$O, 1M S, 0.1M NaOH in miliQ water. With this S^{2-}/S_x^{2-} electrolyte a (   ) redox couple was obtained. From the perspective of chemical reaction, oxidation occurs at the photoanode/electrolyte interface according to [109]:

$$S^{2-} + 2h^+ \rightarrow S \tag{5.1}$$

$$S + S_{x-1}^{2-} \rightarrow S_x^{2-} \tag{5.2}$$

At the counter electrode, reduction occurs where S_x^{2-} is reverted back to S^{2-}:

$$S_x^{2-} + 2e^- \rightarrow S_{x-1}^{2-} + S^{2-} \tag{5.3}$$

This chemical reaction is thought to enhance the hole recovery rate which results in a higher performance of the solar cell

With the purpose of properly catalyzing the reduction of the electrolyte, Cu$_2$S electrodes were made by immersing brass foils in concentrated (38%) HCl at 90ºC for 20 min. With this treatment the superficial Zn is removed from the brass (Fig. 5.5a, b). The resulting Cu surface is delimited with tape and sulfated by adding a drop of polysulfties (Fig. 5.5c).

Final devices are assembled by placing a drop of electrolyte on the counter electrode, and covering with sensitized TiO$_2$ films, and holded with foldback clips. The tape defines the working area and acts as spacer between the photoelectrode and counter electrode to contain the electrolyte in the assembled cells.
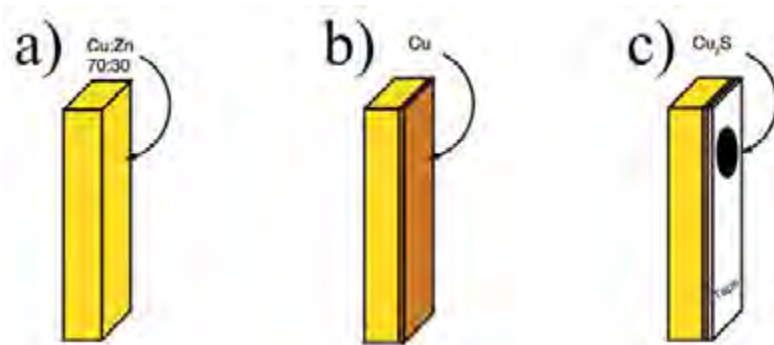
Fig. 5.5. Schematic representation of Cu$_2$S counter-electrode elaboration, a) commercial brass foil, b) after HCl treatment, c) delimited and sulfated

5.2. SILAR

Successive Ionic Adsorption and Reaction (SILAR) is a method to synthesize and deposit sensitizers such as PbS, CdS, ZnS and others QDs. A SILAR cycle consists in a TiO$_2$ film dip in a solution with the wanted cation (Pb, Cd or Zn) for 1 min (Fig. 5.6a) allowing the ions to deeply penetrate into the film. Then, the film was dried for 1 min and dipped 1 min in the solvent used to dissolve the cation removing the excess of ions. After another minute of drying, the film was immersed in a solution with the wanted anion (S^{2-} in our case). It is in this step when the reaction was done forming the QDs. Finally, the film was dried and washed in the solvent used to dissolve the anion. To increase the amount of deposited QDs many cycles were done until the wanted QDs concentration was reached.
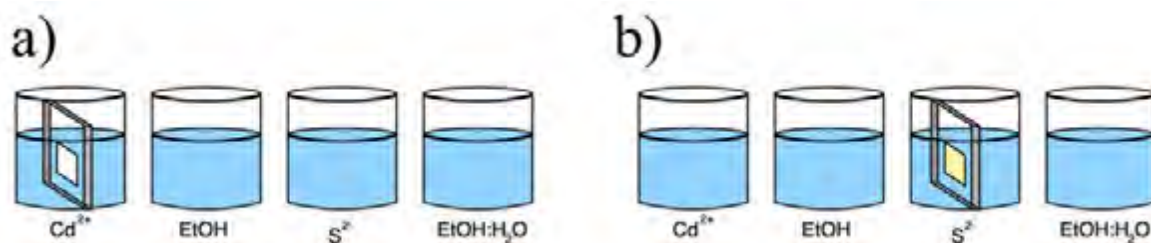
Fig. 5.6. Schematic representation of a SILAR cycle a) Cation dipping b) Anion dipping and reaction to form CdS QDs

The precursor solution used for SILAR was: 0.02 M lead acetate trihydrated (Pb_{act}) in methanol (MetOH) and 0.02M of sodium sulfate nonahydrated (Na_2S) in a 1:1 MetOH:H_2O mix to synthesize PbS QDs; 0.05M of Cadmiun Acetate (Cd_{act}) in EtOH and 0.05M Na_2S in MetOH:H_2O 1:1 for CdS; and 0.1M of Zinc Acetate (Zn_{act}) in H_2O and 0.1 M of Na_2S to make ZnS QDs.

5.2.1.   SILAR Optimization:

This part of the work describes the study done to optimize the efficiency of SILAR deposition for sensitized solar cells.

Number of cycles:

As a first approximation, to increase the photo absorption and the photocurrent, the number of SILAR cycles was varied. The substrates with 3 deposits of the TiO_2 compact layer (spray pyrolysis), 3 deposits of the transparent layer and 3 of the scattering layer (3c/3t/3s), were sensitized according to the following configurations. CdS(6 cycles) /ZnS(2 cycles) (as blank), PbS (1 cycle)/ CdS(5 cycles)/ZnS(2 cycles), PbS(1 cycle)/CdS(6 cycles)/ ZnS (2 cycles) and PbS(2 cycles of 30seconds)/CdS(6 cycles)/ZnS(2cycles).

The J-V curves displayed in Fig. 5.7 show that the addition of PbS to CdS/ZnS films increase J_{sc} meanwhile the V_{oc} is reduced (see Tabe 5.1), indicating a much larger photogeneration due the PbS absorption in the near infrared. In the same way, with the increase of CdS cycles (PbS(1)/CdS(6)/ZnS(2)) both J_{sc} and V_{oc} were increased giving a conversion efficiency of η=2.9%. This indicates that the films could adsorb more QDs without significantly reducing the charge carrier transport and efficiency. However, when the cycles of PbS are increased (PbS(2)/CdS(6)/ZnS(2)), J_{sc} and V_{oc} are considerably reduced compared to (PbS(1)/CdS(6)/ZnS(2)). It is important to note that FF is not negatively affected by the extra cycle of PbS, suggesting that the reduction in performance is not due to transport problems.

Fig. 5.7. Representative J-V curves of solar cells sensitized with QDs of PbS, CdS and ZnS deposited by SILAR varying the number of SILAR cycles.

Tabe 5.1 Representative J_{sc}, V_{oc}, FF and η of solar cells sensitized with QDs of PbS, CdS and ZnS deposited by SILAR varying the number of SILAR cycles.

Sample	J_{sc} (mA/cm)	V_{oc} (mV)	FF (%)	η (%)
CdS(6)/ZnS(2)	7.84	496	53.26	2.07
PbS(1)/CdS(5)/ZnS(2)	11.11	436	53.91	2.61
PbS(1)/CdS(6)/ZnS(2)	11.97	478	50.68	2.90
PbS(2*0.5)/CdS(6)/ZnS(2)	10.31	284	60.66	1.78

The IPCE curves (Fig. 5.8) show how the addition of PbS considerably extends the wavelength region used for photogeneration. However, at the same time that it increases de Quantum Efficiency (QE) in the region from 600 to 1000 nm, the QE for λ < 550 nm (that correspond to the CdS QD's absorption) was reduced. And when the number of cycles of PbS is increased this effect becomes

63

stronger. This means that the addition of PbS QDs effectively increases the photogeneration by contributing with the absorption of near infrared light, but at the same time, the strong absorption of visible light of the PbS limit the amount of light that reaches the CdS QDs. Then, to maximize the efficiency of the cell it is necessary to find the amount of PbS QDs that absorb enough infrared light without limiting too much the photogeneration of the CdS QDs.

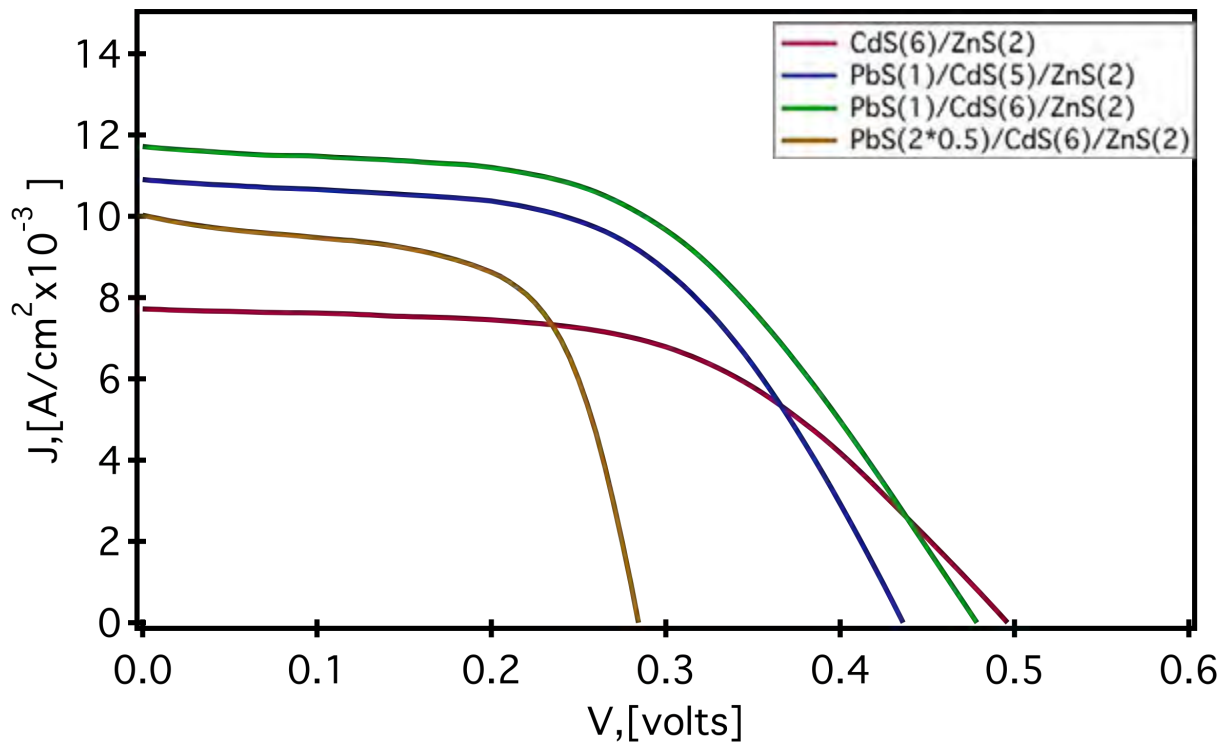**Fig. 5.8.** Representative IPCE curves of solar cells sensitized with QDs of PbS, CdS an ZnS deposited by SILAR varying number of SILAR cycles.

TiO_2 thickness:

The Second approximation to increase the photocurrent and then the conversion efficiency was increasing the thickness of the transparent and the scattering TiO_2 layers to allow a higher adsorption of the sensitizers. All samples had 3 deposits of the compact layer (3c), and variations of the thickness were done by increasing the number of deposits in the other two layers. Tree configurations of the film were studied: 3 deposits of transparent layer and 2 deposits of scattering layer

(3c/3t/2s), 4 deposits of transparent layer and 2 deposits of scattering layer (3c/4t/2s) and 3 deposits of transparent layer with 3 deposits of scattering layer (3c/3t/3s). The samples were sensitized by SILAR PbS(1 cycle)/CdS(5 cycles)/ZnS(2cycles), a CdS(5 cycles)/ZnS(2 cycles) sample was added as a blank. In addition, the effect of drying the samples with air during the SILAR cycles was studied.

The J-V curves of the samples (Fig. 5.9) show that when the thickness of the films increases (3c/3t/3s and 3c/4t/2s), J_{sc} increases with minimal reduction of FF (Tabe 5.2). Being the higher increase with the 3c/4t/2s films (J_{sc}=13mA/cm^2, η=2.9%). These results suggest that increasing the thickness, leads to an increase in the amount of adsorbed QDs that in turn induces a higher photogeneration and photocurrent. However, it limits the charge carrier transport (FF) because of the larger transport length. Being the final effect an increase in η.
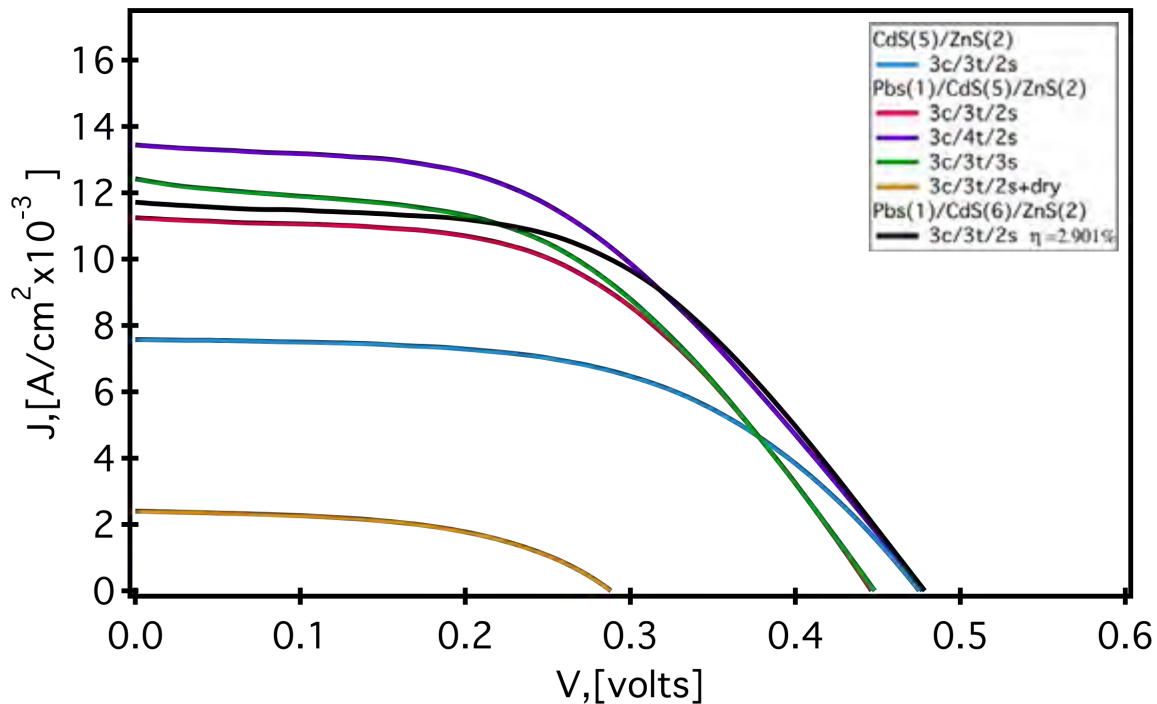
Fig. 5.9. Representative J-V curves of PbS, CdS and ZnS QDs sensitized cells varying the number of deposits in the Transparent TiO$_2$ layer (t) and the TiO$_2$ scattering layer (s).

Tabe 5.2. Representative J_{sc}, V_{oc}, FF and η of PbS, CdS and ZnS QDs sensitized cells varying the number of deposits in the Transparent TiO_2 layer (t) and the TiO_2 scattering layer (s).

Sample	J_{sc} (mA/cm^2)	V_{oc} (mV)	FF (%)	η (%)
CdS(5)/ZnS(2)				
3c/4t/2s	7.66	475	54.06	1.97
PbS(1)/CdS(5)/ZnS(2)				
3c/3t/2s	11.48	446	50.66	2.59
3c/4t/2s	13.75	477	45.59	2.99
3c/3t/3s	12.67	448	47.25	2.68
3c/3t/2s+ dry	2.41	288	51.20	0.36

Fig 5.10 confirms that the increase in film thickness increases the QE in all useful wavelengths. However, when the scattering layer is thicker (3c/3t/3s) the QE increase is more pronounced for λ < 600 nm. In the other hand, when the transparent layer is thicker (3c/3t/2s) the QE increase is slightly pronounced in the region with λ>600nm. This could be attributed to the fact that PbS QDs were deposited before than CdS ones. Then, the film with more transparent layer (inner layer) facilitate a better anchoring of the PbS QDs increasing the QE in their absorption region. Moreover, as CdS QDs are deposited after PbS they are closer to the scattering layer. Then with 3c/3t/3s configuration CdS QDs will capture more scattered light increasing the QE in their working region.
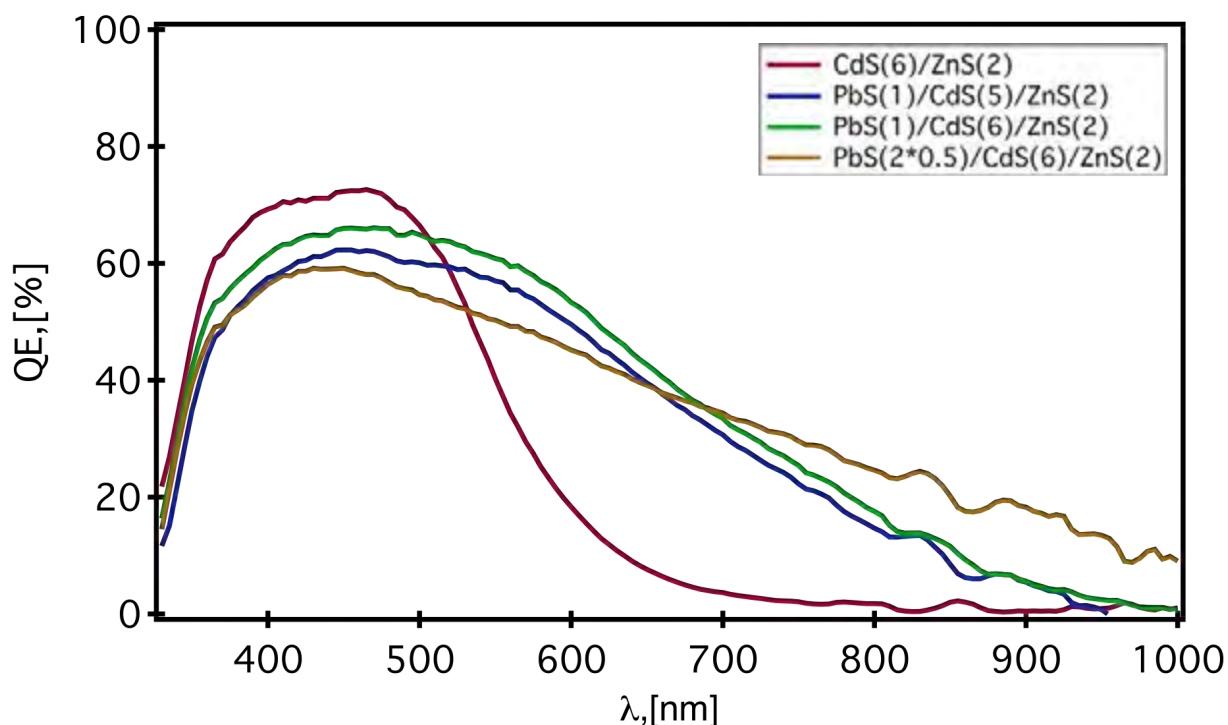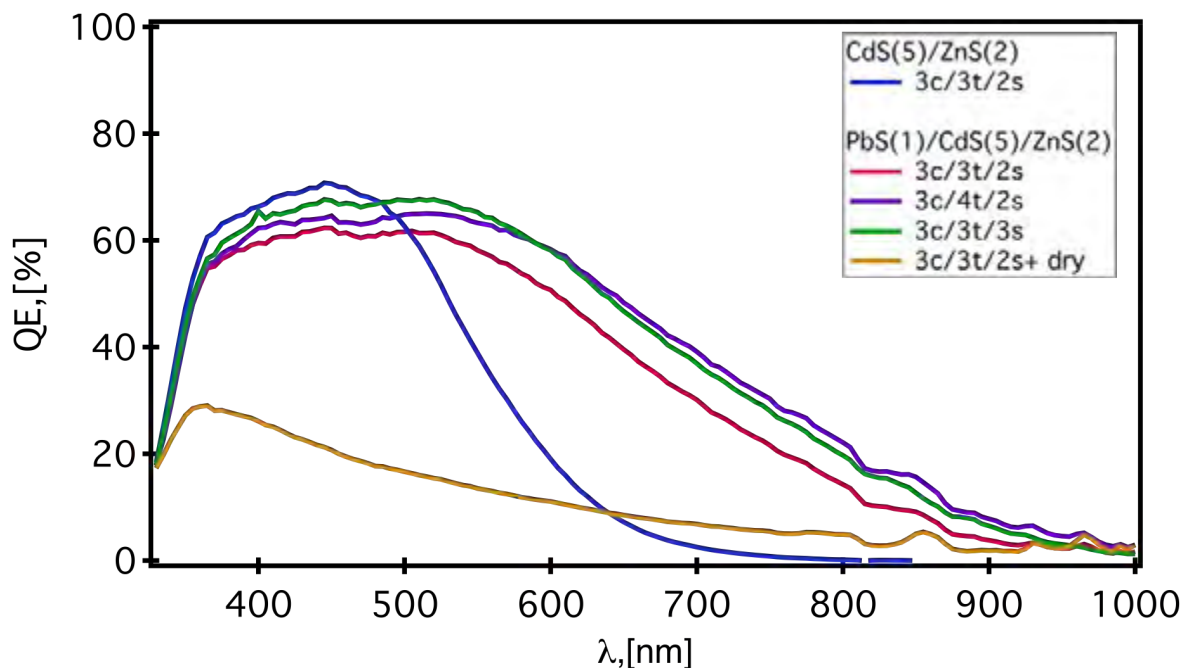
Fig. 5.10. Representative IPCE curves of solar cells sensitized with QDs of PbS, CdS an ZnS deposited by SILAR varying the number of deposits of the TiO_2 transparent (t) and scattering (s) layers.

Immersion Time & Number of SILAR cycles:

The effect of adding an extra SILAR cycle of CdS was tested by doing samples with 6 and 7 cycles of this QDs; also the effect of the deposition time for the PbS QDs was varied (60 and 120 seconds). These samples were grown using the TiO_2 films that had the better performance in the previous section (3c/4t/2s).

The J-V curves of these samples in Fig. 5.11 show that the highest efficiency was obtained with PbS(1)/CdS(6)/ZnS(2) (η = 3.5%), being higher than the obtained for similar configurations with (3c/3t/2s) TiO_2 films and comparable with best efficiencies for similar configurations and deposit methods (4%) [110]. It is also remarkable that by increasing the CdS cycles a decrement in J_{sc} and V_{oc} was obtained. Meanwhile, increasing the deposition time for PbS gives a slight

67

decrement in V_{oc} but with a negligible effect on J_{sc} (see Tabe 5.3). According to IPCE measurements (Fig. 5.12), the photocurrents obtained for 60 and 120 s deposition of PbS are due to different proportions of visible and infrared contributions, i.e. when the deposition time is increased the QE in visible light is reduced at the same time that it is increased in the near infrared region, resulting in almost the same photocurrent. This suggest the possibility to increase the photocurrent by fine tuning the QE changing the adsorbed PbS amount, although it also will affect the recombination resistance giving the V_{oc} observed variations [111].
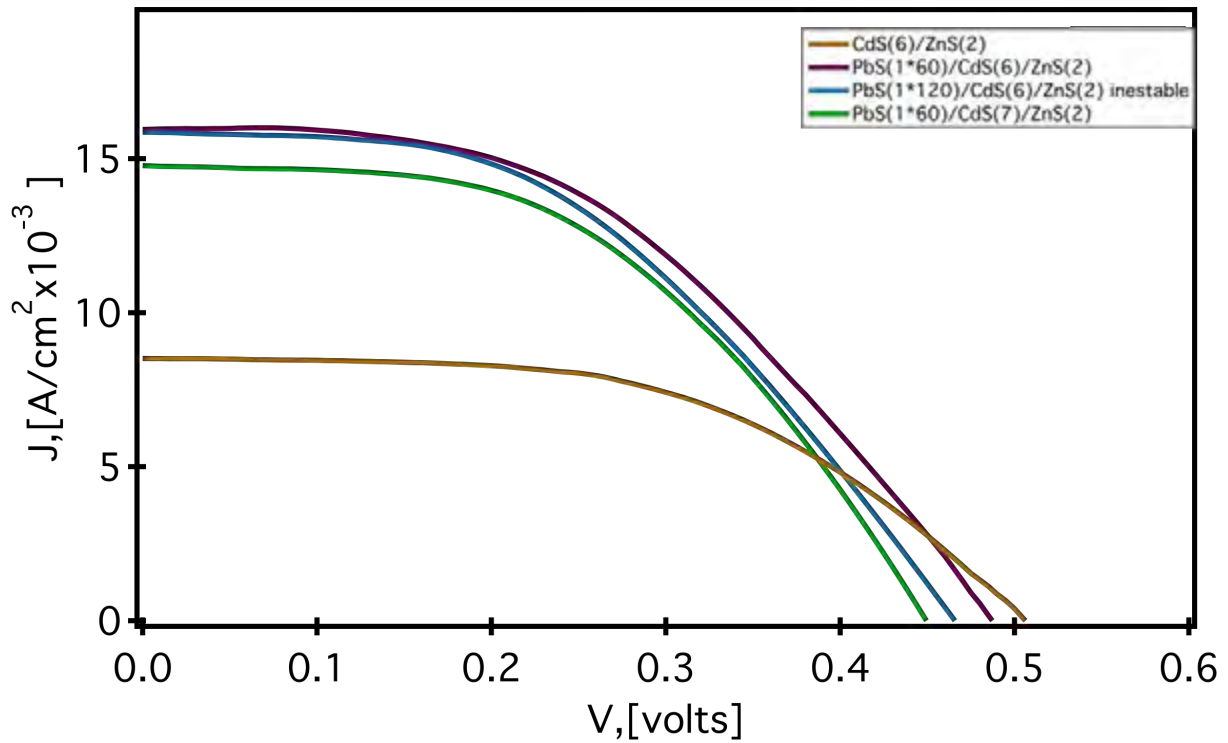
Fig. 5.11. J-V curves of cells made of (3c/4t/2s) TiO$_2$ films sensitized with PbS, CdS and ZnS QDs varying the time and number of SILAR cycles.

Tabe 5.3. J_{sc}, V_{oc}, FF and η of (3c/4t/2s) TiO_2 films sensitized with PbS, CdS and ZnS QDs varying the time and number of SILAR cycles.

Sample	J_{sc} (mA/cm^2)	V_{oc} (V)	FF (%)	η (%)
CdS(6)/ZnS(2)	8.64	0.485	54.21	2.27
PbS(1*60)/CdS(6)/ZnS(2)	15.95	0.485	46.27	3.58
PbS(1*120)/CdS(6)/ZnS(2)	15.86	0.465	46.11	3.40
PbS(1*60)/CdS(7)/ZnS(2)	14.77	0.450	49.00	3.26
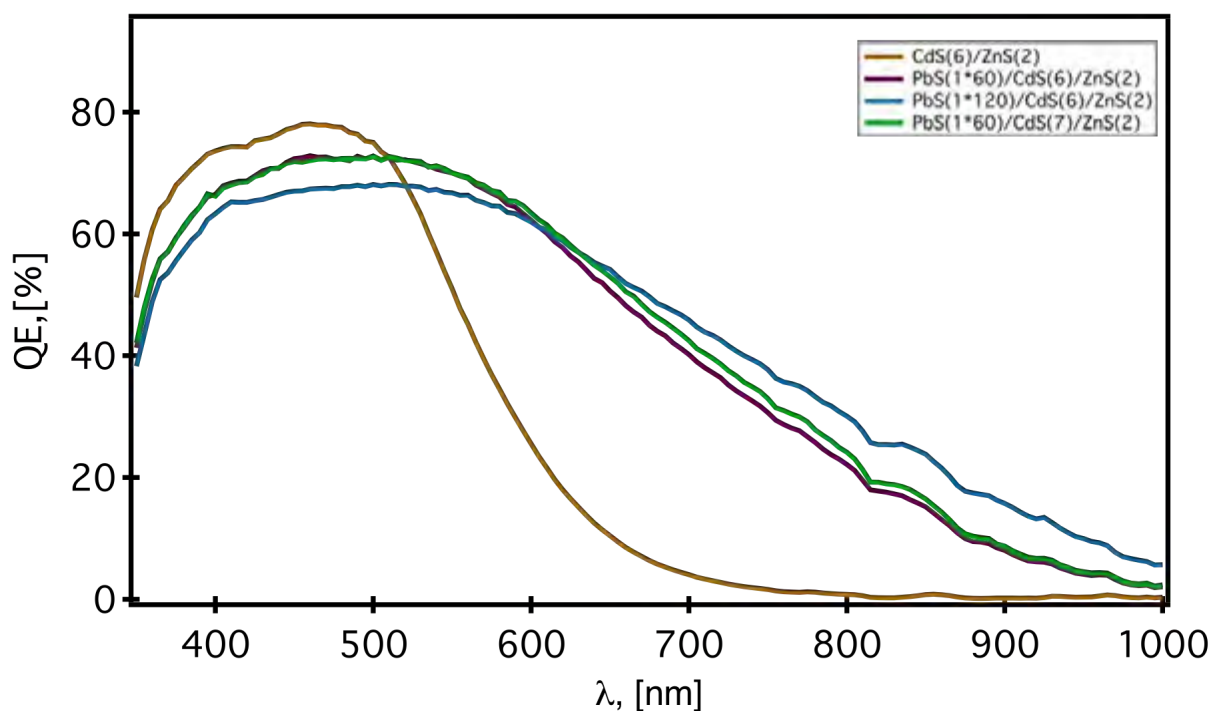
Fig. 5.12. IPCE curves of cells made of (3c/4t/2s) TiO_2 films sensitized with PbS, CdS and ZnS QDs varying the time and number of SILAR cycles.

5.3. Electrophoresis

Electrophoresis (EP) is a technique that allows to deposit colloidal QDs, that have less defects than SILAR QDs, then if the same amount of QDs are deposited by SILAR and EP, cells sensitized by EP should have better electrochemical performance. To sensitize TiO_2 films by electrophoresis a solution 8×10^{-6} M of

commercial colloidal PbS QDs in toluene was prepared. Then, two substrates with (3c/3t/2s) TiO_2 film were immersed face to face in the solution separated by 5 mm from each other (Fig. 5.13a). After that, 200V were applied between the samples. This voltage strongly charges the films and polarizes the QDs surface, attracting them to the nearest electrode. After some time the QDs were strongly bound to the TiO_2 films, being more concentrated the deposit in the inner layers of the film, and increasing the concentration with the deposition time (Fig. 5.13b). Immediately after Electrophoresis deposition (EP), the films were protected from degradation by SILAR depositing of CdS (5 cycles) and ZnS (2 cycles).
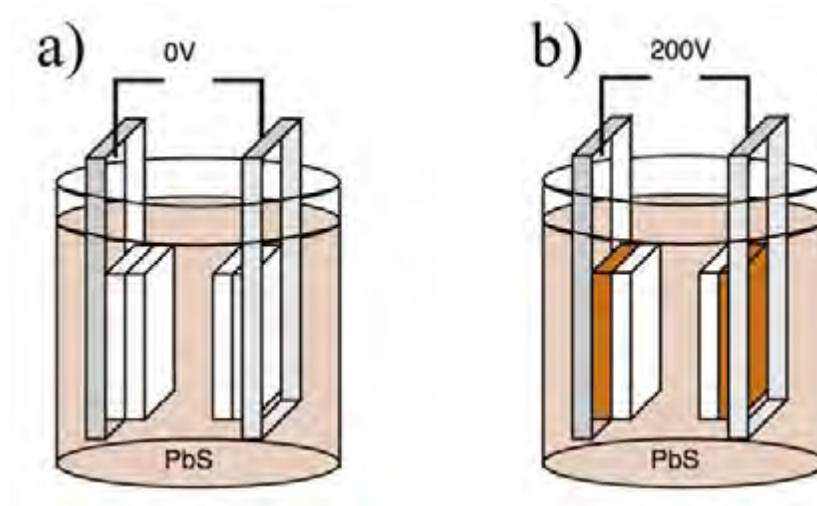
Fig. 5.13. Schematic representation of the electrophoresis process. a) inmersion of TiO_2 films in PbS QDs colloidal solution, b) applying voltage.

5.3.1.   Effect of the EP deposition time.

To measure the effect of the deposition time, samples with 30, 60 and 90 min of EP were tested using a CdS(5 cycles)/ZnS(2 cycles) cell as blank. Results displayed in Fig. 5.14 and Tabe 5.4 show that the higher J_{sc} and V_{oc} were obtained with 30 and 60 min of EP (13.53, 13.46 mA/cm^2 and 538, 546 mV respectively) maintaining almost the same FF than the blank (FF > 50%). This induces an

70

increase of η from 2.53% in CdS/ZnS samples to 3.75% in 60 min EP samples, higher than the reported for EP deposited PbS/CdS QDs (2.1%). When the EP time was increased for above 30 min a considerable reduction of the J_{sc} and η were observed. It is also noteworthy that the 30 and 60 min samples that were positively charged in the EP (indicated by (+) in Table 5.4) have higher photocurrent than the negative ones. While, for 90 min the negatively charged sample has higher photocurrent. This suggest that the EP process with this QDs is faster in the positive electrode, and with 90 min of EP the samples are saturated of PbS QDs so the performance of the cells is reduced, being more notorious in the positive electrode.

Fig. 5.14. J-V curves of cells with CdS/ZnS QDs deposited by SILAR and cells with QDs de PbS deposited by 30 to 90 min EP and covered with CdS/ZnS QDs deposited by SILAR. + and – indicate the polarity durin the deposit.

Table 5.5. J_{sc}, V_{oc}, FF and η of cells of CdS/ZnS QDs deposited by SILAR and cells with QDs de PbS deposited by 30 to 90 min EP and covered with CdS/ZnS QDs deposited by SILAR

Code	Sample	J_{sc} mA/cm2	V_{oc} mV	FF %	η %
c13	CdS/ZnS	8.13	434	52.98	1.87
c14	CdS/ZnS	9.86	493	52.05	2.53
z01	PbS(90min) (+)/CdS/ZnS	8.84	496	53.81	2.36
z02	PbS(90min) /CdS/ZnS	11.61	506	53.83	3.16
z03	PbS(60min) (+)/CdS/ZnS	13.53	538	51.45	3.75
z04	PbS(60min) /CdS/ZnS	12.77	517	53.50	3.53
z05	PbS(30min) (+)/CdS/ZnS	13.46	546	50.96	3.74
z06	PbS(30min) /CdS/ZnS	11.79	514	54.36	3.29

The IPCE curves displayed in the Fig. 5.15 indicate an expansion of the spectrum region were QE > 58% with 30 min of EP suggesting a contribution of the PbS QDs in the photogeneration. This effect is reduced when the EP time is increased, for 90 min the QE at 550 nm is reduced compared with samples without PbS. This indicates that with 90 min EP, the PbS QDs interfere with the CdS photogenration process confirming the previously mentioned saturation process.
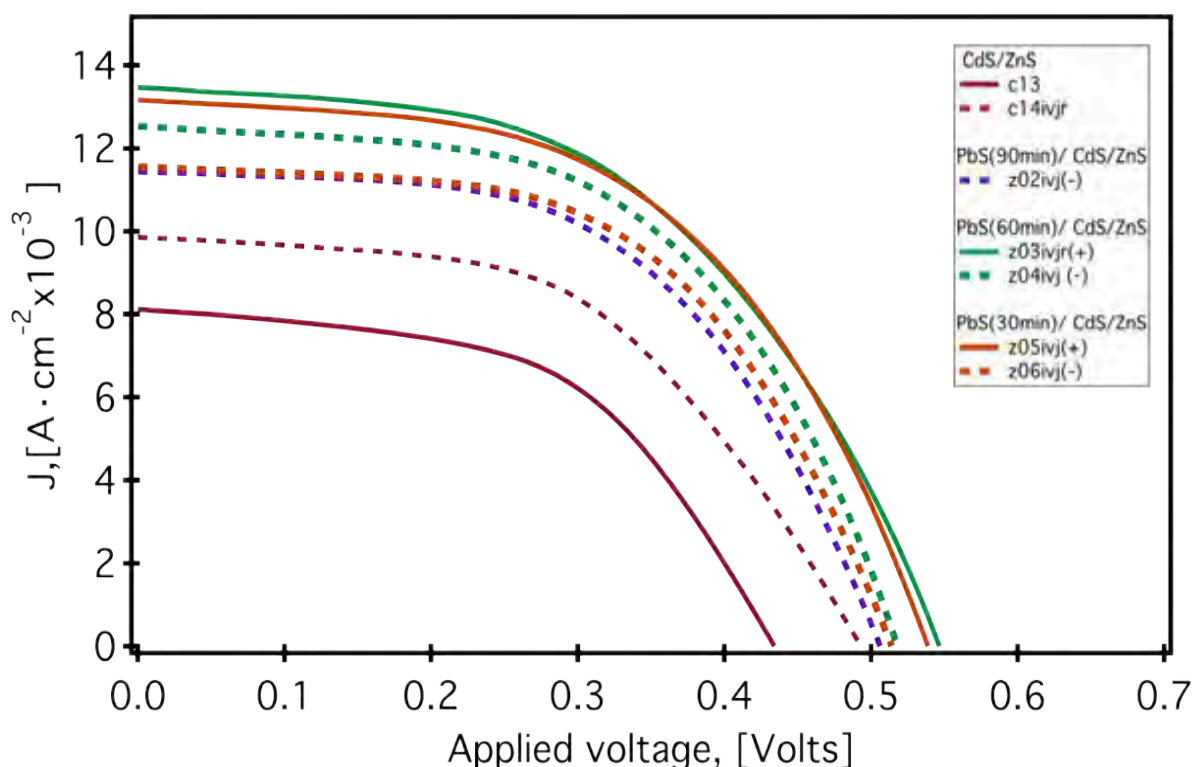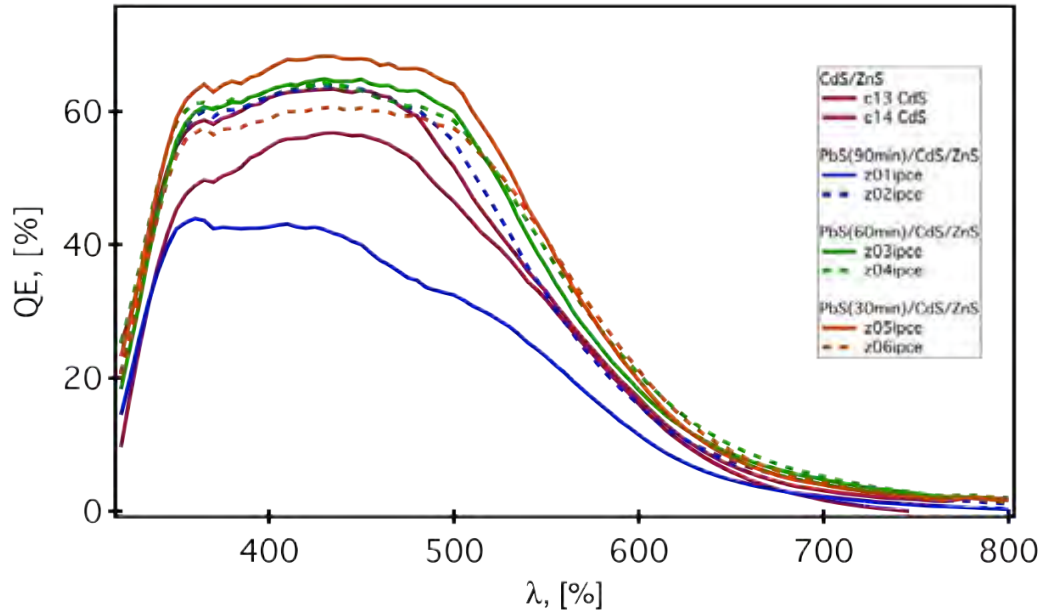
Fig. 5.15. IPCE of cells with CdS/ZnS QDs deposited by SILAR and cells with QDs of PbS deposited by 30 to 90 min EP and covered with CdS/ZnS QDs deposited by SILAR.

5.4. Conclusions

It was determined that the best configuration for solar cell sensitized by SILAR has 3 deposits of TiO_2 compact layer, 4 of the transparent layer and 2 of the scattering layer, and is decorated with 1 cycle of 1 minute of PbS, 6 cycles of CdS and 2 cycles of ZnS, giving an efficiency of 3.5% a little lower than the best results for SILAR deposited PbS QDs (4%) [110]. It also was found that making little variations of these parameters could give variations in the QE that could result in an increase of the photocurrent and efficiency.

While when PbS colloidal QDs are deposited by EP, the optimal deposition time was 60 minutes. In which an η of 3.75% is obtained, (higher than best results in EP QDs 2.1% [108]). This efficiency is propitiated by an increase in the photocurrent due to an increment in the QE, and a high FF obtained by avoiding the QD's saturation.

73

As result of these studies, not only high efficiencies were obtained, but also high control and reproducibility in the dising of solar cells, that will allow better characterize new architectures.

Chapter 6.
Other QDs Sensitized TiO$_2$ Photovoltaic Applications (H$_2$ Production).

One of the most promising strategies for solar energy conversion and storage is based on mimicking the photosynthetic organisms which harvest and store solar energy in chemical bonds from abundant raw materials (water and carbon dioxide). [112,113] This approach is termed artificial photosynthesis and the simplest scheme is based on the photo-assisted splitting of water with semiconductor materials to generate hydrogen (H$_2$) as an energy carrier. [114] Scientists have intensively focused on the development of suitable semiconductor materials and devices able to efficiently decompose water with the only input of sunlight [115-118]. The most advanced devices entail dual band gap tandem p/n photoelectrolysis cells, which can provide solar-to-hydrogen (STH) efficiencies of 15%[119,120]. So far, efficiencies of 12.4% have been reported for III-V semiconducting materials, although at the expenses of high cost and low stability. [121]. Recently, Nocera et al. demonstrated an artificial leaf device based on a triple junction photovoltaic structure with earth-abundant catalysts and STH efficiencies close to 8%. [117], unfortunately its high cost severely limit further commercial application. In this context, mesoscopic metal oxides appear as a promising alternative for unassisted water splitting providing a wide prospect of low cost materials with attractive features. Although several metal oxides have been extensively studied, such as TiO$_2$, WO$_3$, α-Fe$_2$O$_3$, none of these materials allow efficient STH conversion due to either too large bandgaps (TiO$_2$, WO$_3$) or inadequate band alignment to split water and reduce H$_2$ (WO$_3$, α-Fe$_2$O$_3$) [122]. Sensitization of wide bandgap semiconducting materials like TiO$_2$ can provide a

smart solution to overcome the limitations of poor light harvesting in the visible region [123,124]. Indeed, several recent studies have reported solar hydrogen devices based on wide bandgap semiconducting materials (TiO_2, ZnO) sensitized by chalcogenide quantum dots (QDs) [125-129] [130]. Although chalcogenide based semiconductors are not able to carry out unassisted solar water splitting since they suffer from fast photocorrosion in aqueous solutions, this limitation can be overcome by the use of sacrificial agents, e.g. Na_2SO_3 or Na_2S. As a remarkable example, short circuit currents of 16 mA/cm^2 have been reported by employing inverse opal TiO_2 photoanodes sensitized with CdSe QDs [129]. On the other hand, narrow band gap semiconductors, as PbS, have also been studied to harness infrared photons for photoelectrochemical conversion [126,128]. A "quasi artificial leaf" based on TiO_2/PbS/CdS heterostructures has proven to produce hydrogen under simulated solar illumination at a rate of 4.30 mL·cm^{-2}·day^{-1} in the presence of a sacrificial oxidation agent. Moreover, one of the fundamental problems of these systems relates to the position of the conduction band edge, slightly above the H+/H_2 electrochemical potential which precludes the reduction of hydrogen at useful rates; unless an external voltage is applied. Indeed, very limited studies have reported effective light driven H_2 evolution without the assistance of an external electrical bias [127,128,130].

This chapter describes development of a device with high unassisted STH conversion efficiency (4.1%) is described, based on a dual absorber tandem comprised of a TiO_2/CdS film connected in series with a DSSC which provides the extra energy needed for efficient water reduction to H_2.

One important issue for dual absorbers is to maximize the photoabsorption of both absorbers. In this sense, CdS decorated TiO_2 absorption (Fig. 6.1), starts in 320nm (that corresponds with TiO_2 absorption) and has its maximum at 430nm being almost zero after 550nm. Meanwhile, Ruthenium n719 DSSC absorption extends until 700 nm and has a maximum at 550nm. Then, CdS QDs and Ruthenium n719 DSSCs were selected because they exhibit partially complementary absorption spectral ranges.

76
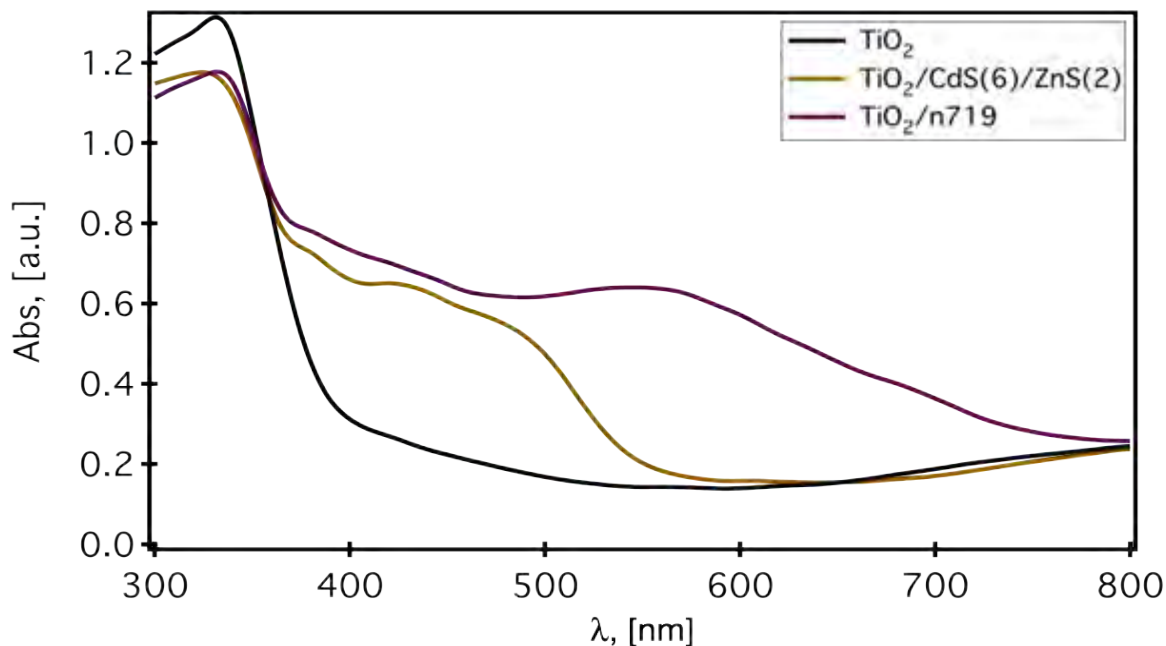
Fig. 6.1. Absorption spectra of CdS decorated TiO_2 and ruthenium N719 DSSC.

6.1. CdS sensitized TiO_2 Films

After selecting the active absorbers, a study was carried out to maximize the performance of each one. For CdS decorated electrode films with 3 deposits of the compact TiO_2 layer applying variations in the thickness on the transparent layer (3 and 4 deposits i. e. 6 and 9 µm respectively) were used. No scattering layer was deposited, to allow the light to propagate through the film and reach the DSSC. Then, the films were sensitized by SILAR depositing CdS (5 and 6 cycles) and ZnS (2 cycles) QDs.

Photoelectrochemical measurements were performed in a two electrode configuration using the sensitized TiO_2 films as photoanode, as counter electrode a platinum mesh, and as electrolyte with sacrificial agent a 0.25 M Na_2SO_3, 0.35 M Na_2S solution. Measurements were done under 100 mW/cm^2 Xe light. As schematized in Fig. 6.2, when the device is illuminated, CdS generate electron hole pairs. Holes (h$^+$) are filled by oxidizing the sacrificial electrolyte with the

reaction described by:

$$S^{2-} + SO_3^{2-} + 2h^+ \rightarrow S_2O_3^{2-} \; .$$

(6.1)

The electrons are injected to the mesoporous TiO_2 and after reaching the FTO substrate, they are directed to the Pt mesh where hydrogen evolves according to the equation:

$$2H^+ + 2e^- \rightarrow H_2$$

(6.2),
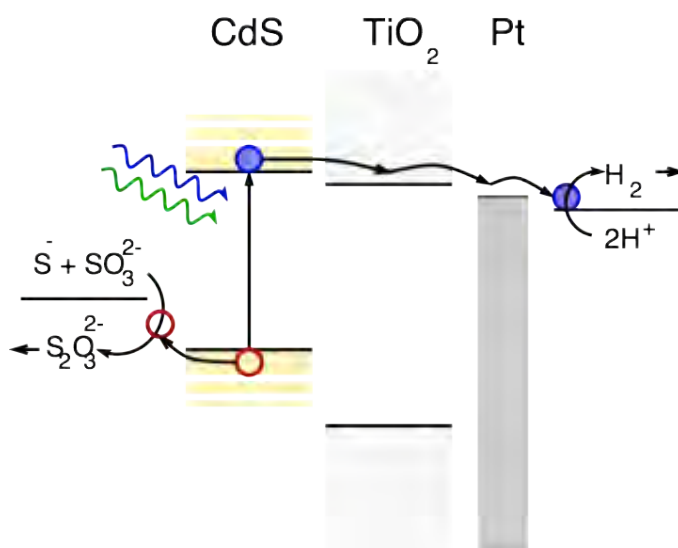
Fig. 6.2. Schematic representation of the energy levels for the hydrogen production with CdS decorated TiO_2 films.

Fig. 6.3 shows the photocurrent response of the samples. As previously mentioned, the B_c of the CdS QDs is only a little above of the redox potential of the hydrogen evolution [51]; then, the photocurrent (and H_2 production) is very poor at "0" V, and increases when a potential is applied. It also was observed that both the increase in the film thickness or the number of SILAR cycles give an increase in

78

the photocurrent, obtaining the best performance with 6 cycles of CdS and 4 deposits of transparent TiO_2 (4.7 μA/cm^2 at 1 V).
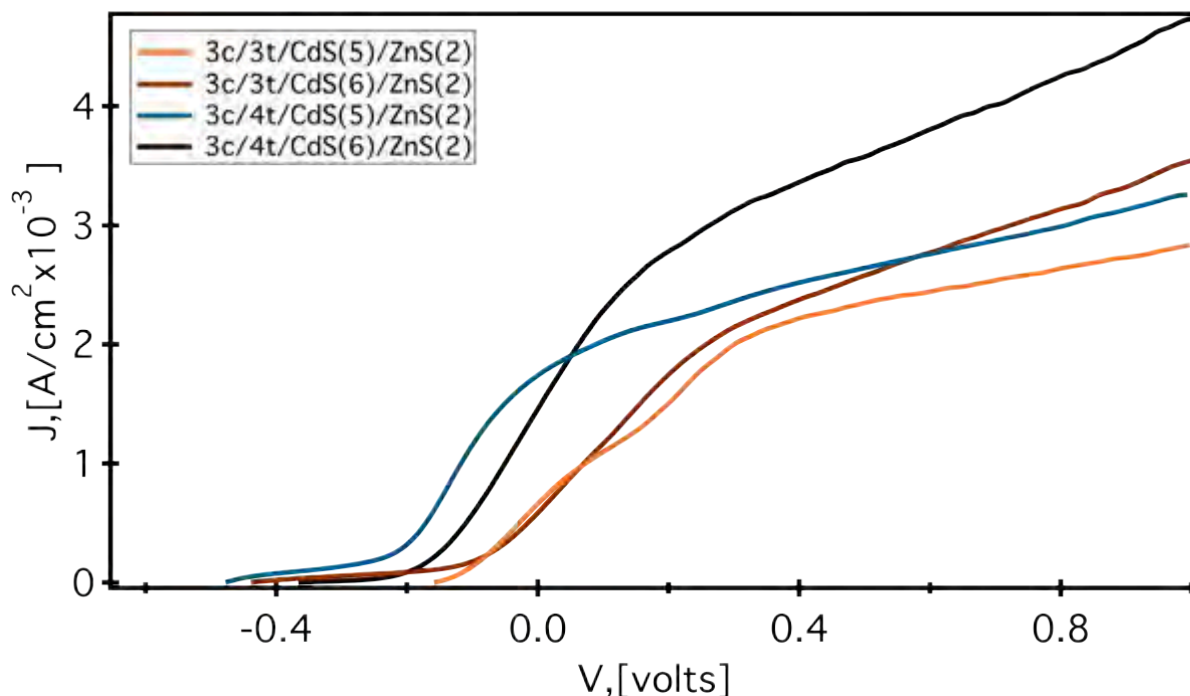
Fig. 6.3. J-V curves of CdS sensitized TiO_2 films measured under 100 mW/cm^2 Xe light inside sacrificial electrolyte.

6.2. Dye Sensitized Solar Cell (DSSC)

The DSSC was also tested with the QDs photoanode facing the light beam, although not connected (QDs || n719), in order to evaluate the effect of the light absorption at the TiO_2/CdS heterostructure on the DSSC performance, the Incident Photon to Current Efficiency (IPCE) of the individual components of the device: the photoanode (TiO_2/CdS) and the DSSC were also measured. As a consequence of the lower incident light, the DSSC performance drops 44.4% in the presence of the QD photoanode (Fig. 6.4). This reduction of incident (and thus absorbed) light in the DSSC due to the presence of CdS is mainly confined to the 300-500 nm

region, as evidenced by the subtraction of both IPCE spectra (see green line in Fig. 6.5). Despite the large decrease of both efficiency and photocurrent, 70% and 60% respectively (inset Fig. 6.4) in the DSSC as a consequence of the optical losses in the measurement chamber, the short-circuit current, J_{sc}, is high enough to facilitate tandem device operation without charge transfer limitations from the TiO_2/CdS photoanode to the DSSC. The photocurrent of the TiO_2/CdS photoanode at zero bias is 1.70 mA/cm^2, while DSSC J_{sc} is 4.26 mA/cm^2.

Sample	J_{sc} mA/cm2	Voc V	FF %	η %
n719[a]	10.87	0.725	63.58	5.01
QDs ll n719[a]	5.59	0.700	71.31	2.79
n719[b]	7.29	0.647	46.40	2.19
QDs ll n719[b]	4.26	0.647	53.50	1.48
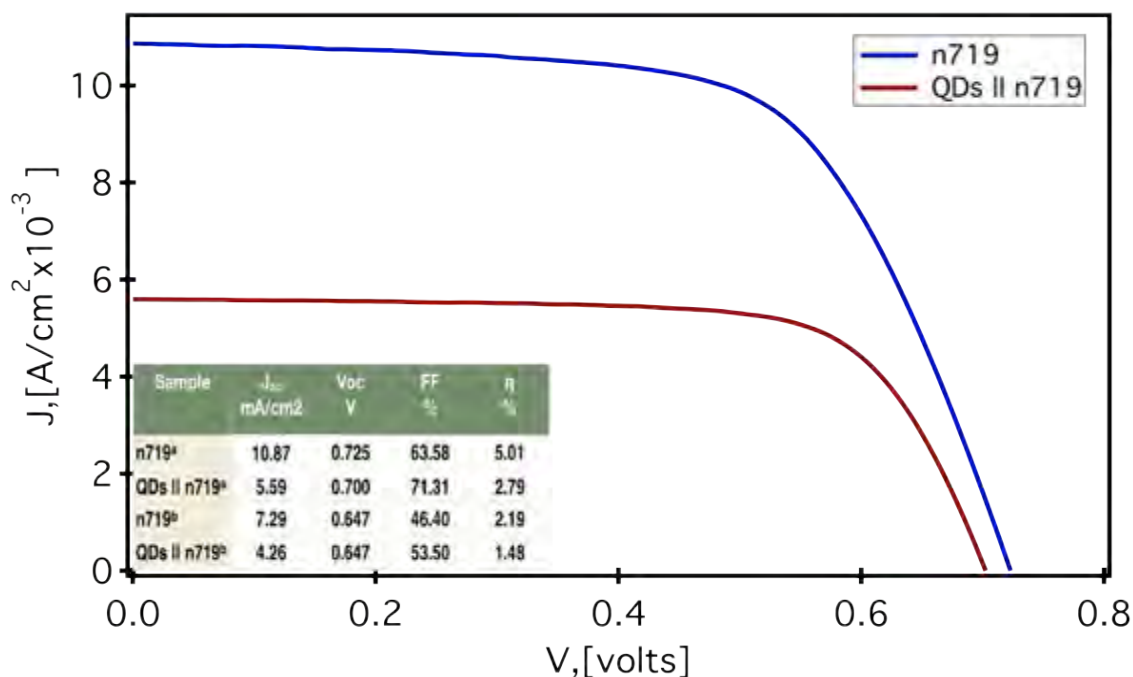
Fig. 6.4. J-V curves of DSSC direct under 1 sun illumination and covered with a CdS decorated TiO_2 film. Inset: Photovoltaic parameters of the DSSCs with and without the TiO_2/CdS film directly facing the light beam. Measurements were carried out in air (a) and in the measurement chamber with electrolyte (b), all of them under 1 sun illumination (100 mW/cm2).
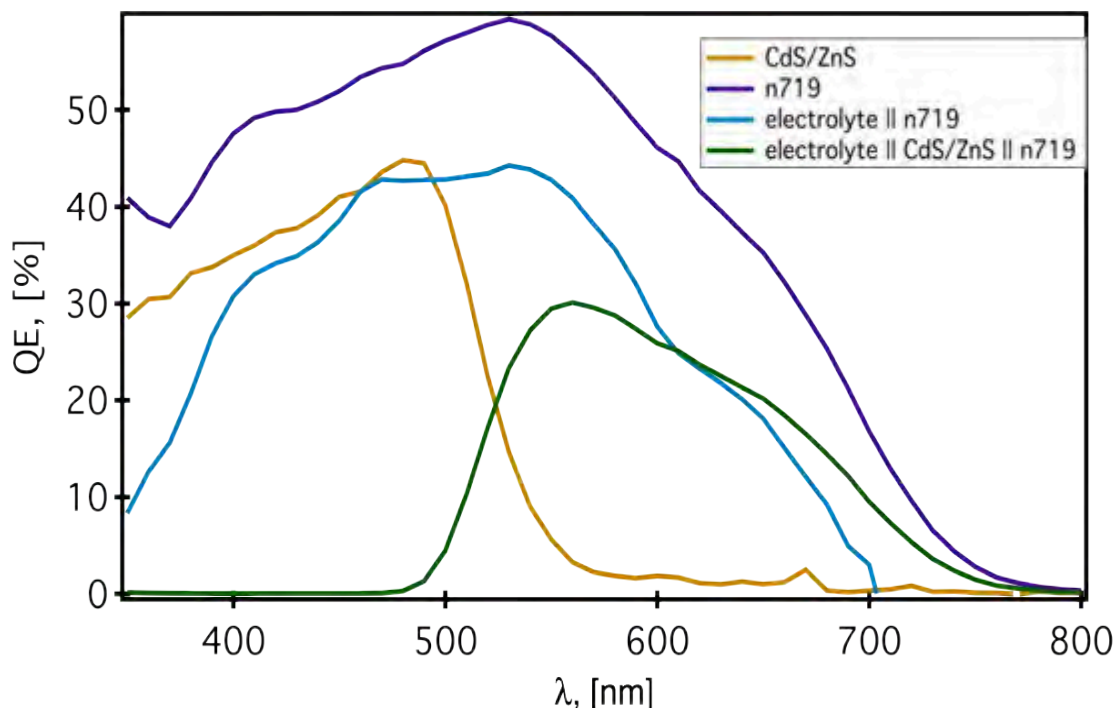
Fig. 6.5. IPCE for CdS, N719 and CdS plus N719 in series but not connected. The IPCE of QD based photoelectrode was recorded at applied potential of 0.7 V. The DSSCs was measured in the electrolyte to discard optical losses that can be attributed to the measurement chamber.

6.3. Tandem Device

The next step was assembling the tandem device, as sketched in Fig. 6.6a. The light beam, entering the photoelectrochemical cell, first reaches the TiO_2/CdS photoanode and upon visible absorption, an electron/hole pair is created at the CdS QD Fig. 6.6b. Subsequently, the electron is injected into the mesoporous TiO_2 frame and after reaching the FTO substrate, it is directed towards the DSSC connected in series. There, electrons reduce the electrolyte to $3I^-$. when this specie reach the dye, the photogenerated holes in n719 filed by oxidize the electrolyte. In this way, an electron photogenerated in CdS is now in the B_v of n719, then, the electron will be promoted to the B_c by a photon ($\lambda \geq 500nm$) and then injected to TiO_2. This provides an additional bias to the electrons that evolve hydrogen

potential when reach the Pt cathode with out applying external potential. On the other hand, the corresponding holes in the CdS QD are reduced by the sacrificial agent in the solution (Na_2SO_3) as described above.
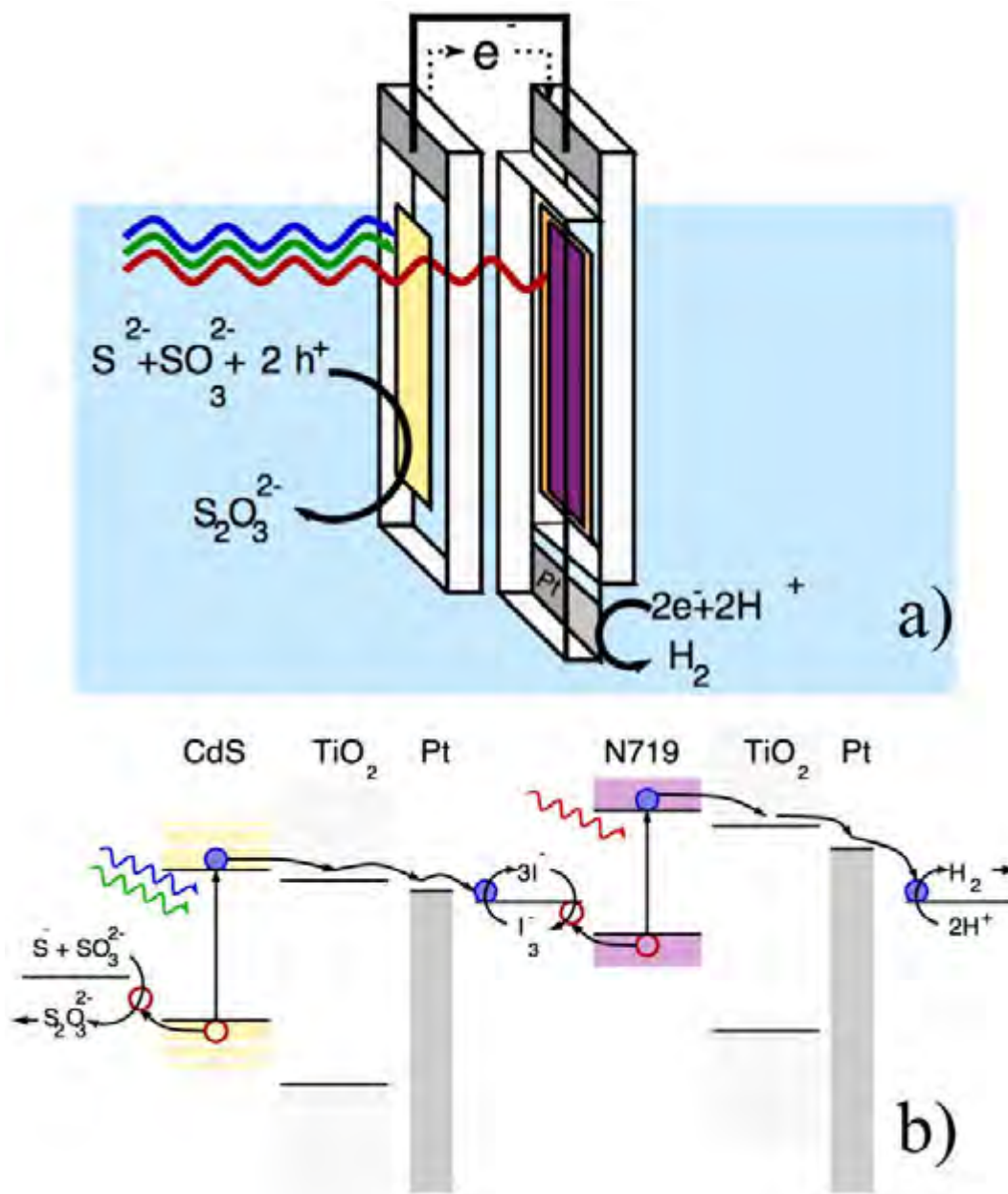
Fig. 6.6. a) Scheme of tandem device in autonomous mode inside of the sacrificial electrolyte. b) Energy level representation of the device showing the reactions needed for the hydrogen evolution.
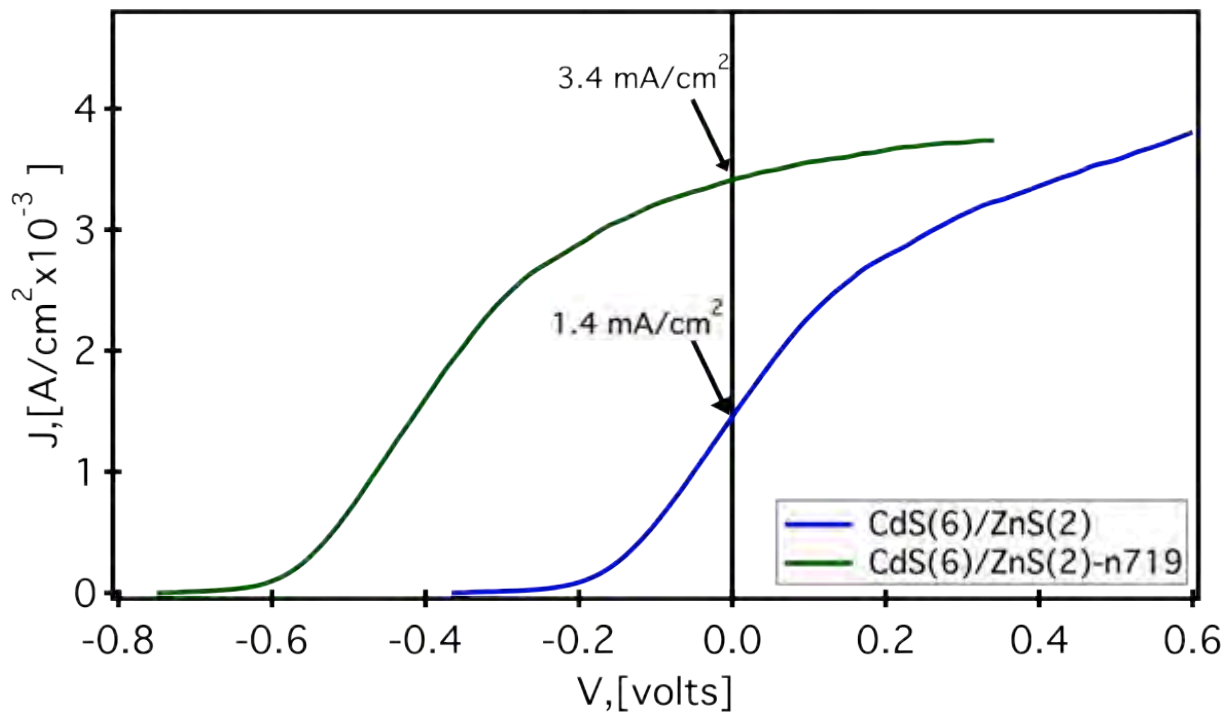
Fig. 6.7. JV curves of CdS films and tandem devices.

Current-voltage curves for both the TiO_2/CdS photoanode and the tandem cell are plotted in Fig. 6.7. When connecting the DSSC in series, a 550 mV cathodic shift of the photocurrent onset is observed, attributed to the contribution of DSSCs, which promotes the electrons to a high energy level and dramatically improves the performance for unassisted hydrogen generation. This cathodic shift is consistent with the photovoltage of the DSSC (647 mV). The operational current of the tandem system is 3.4 mA/cm^2, near 2.5 times the photocurrent of the CdS based films, indicating a high increase in the autonomous hydrogen production. Finally, Solar To Hydrogen (STH) conversion efficiency was estimated using large area devices (1.5 × 1.5 cm^2), collecting the hydrogen bubles with an inverted burette (see apenddix A and adjunct file h2 movie). STH can be expressed as the fraction of incident solar energy photo-converted into chemical energy [131].

$$STH = \frac{\Delta G^0_{H_2} * R_{H_2}}{P_i * A}$$

(6.3)

83

where, $\Delta G_{H_2}^0$, is the standard Gibbs energy for the hydrogen formation reaction (237,200 J/mol), R_{H_2} is the hydrogen generation rate (mol/s) in standard conditions, P_i is the incident solar irradiance (W/m^2) and A is the irradiated area. Fig. 6.8 shows the amount of collected hydrogen in an inverted burette as a function of time and the net photocurrent recorded during the measurement. The maximum amount of hydrogen generated can be estimated by integrating the photocurrent over the time and dividing by two, since hydrogen generation is a two electron process. Comparing the experimental amount of hydrogen collected (+ symbols, Fig. 6.8n) with the estimated H$_2$ evolution (blue line, Fig. 6.8) 62% of the photogenerated carriers lead to hydrogen production, most of the losses are attributed to bubbles trapped in the Pt mesh. STH efficiencies for both the TiO$_2$/CdS photoanode and the tandem device are shown in Table 1. All the measurements were performed under standard conditions, P= 1 atm and T=298 ^oC, and the efficiencies were estimated for the first 1 h, before the consumption of sacrificial agent significantly affects the photocurrent values. In these conditions, the net current can be considered constant. This result highlights the key role of the DSSC, promoting the electron to a higher energetic state level and inducing light driven H$_2$ generation, with recorded STH efficiencies of 4.1%; nearly threefold the reported for the single QD based photoanode.

Table6.1. Experimental Solar to Hydrogen conversion efficiencies for single TiO$_2$/CdS photoanode and tandem device. (J$_{op}$, operational current density, I$_{op}$, operational current, R$_{H2}$, rate of H$_2$evolution, STH, solar to hydrogen conversion efficiency).

Sample	J$_{op}$ mA/cm2	I$_{op}$ mA	R$_{H_2}$ nmol/s	STH %
TiO$_2$/CdS	1.40	0.350	1.78	1.69
Tandem	3.40	0.846	4.32	4.10
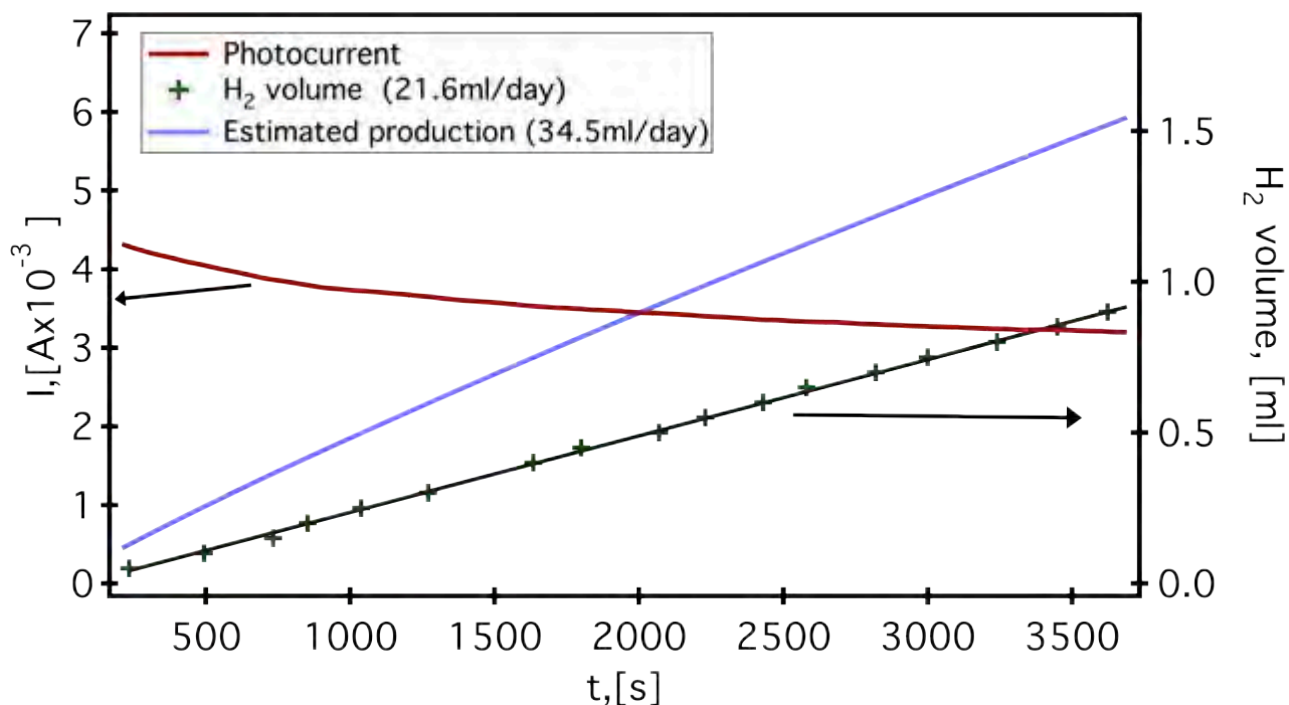
Fig. 6.8. Photocurrent and evolution of hydrogen gas at 0 V lighting 100 mW/cm^2 Xe lamp**.**

6.4. Conclusions

In summary, we demonstrated the improvement in unassisted hydrogen generation of a CdS calchogenide photoanode by designing a tandem device and connecting it in series with a ruthenium based DSSC. To the best of the authors' knowledge, the reported 4.1% STH efficiency of the tandem device is the highest one reported for these heterostructured systems. The present results are expected to open wide avenues in the design of tailored nanocomposites based on mesoporous photoanodes working in parallel tandem devices, improving the light absorption properties within a broad spectral range, from visible to near-IR; as well as hydrogen generation rates.

Chapter 7.
General Conclusions

During this research work several materials for solar cells and photovoltaic applications based in decorated or sensitized TiO_2 were studied. In particular it was found that the use of Au NPs increases the FF and the efficiency of TiO_2 films by improving the charge carrier separation and the electron transport. CdSe QDs considerably increase the charge carrier photegeneration, resulting in an increment of the photocurrent and η. Finally, P3OT increases the hole transport and the photogenreation precess. As each material has advantages and disadvantages in very specific process in the cell, experiments were performed mixing the materials to obtain the better properties of each one. It was found that all multi-decorated films have higher η than TiO_2/CdSe QDs, TiO_2/P3OT or TiO_2/Au NPs films. During this study, a completely new solar cell architecture was proposed (TiO_2/Au/CdSe QDs/P3OT), where Au NPs and P3OT synergistically increase the photoconversion efficiency (600%) in comparison with TiO_2/CdSe QDs cells, being higher than the addition of the increase give by the Au NPs and P3OT separately.

Impedance studies were done to better understand the charge transport in this complex architecture. The RC model proposed to interpret the EIS measurements describes the electron transport process in the different interfaces between each sensitizer. These measurements in combination with other characterization techniques indicate that CdSe QDs are the principal photogenerator in TiO_2/Au/QDs/P3OT films. Au NPs considerably enhance the electron transfer process between CdSe QDs and TiO_2 resulting in an increase of FF. Furthermore, P3OT contributes with the photogeneration process by absorbing the photons that are not used by the CdSe QDs. This polymer also acts as a hole

conductor, increasing the collected charge carriers, and at the same time works as a passivation layer that reduce the superficial recombination sites strongly increasing the FF. All this combined with the strong photoabsorption of CdSe QDs and the improvemed electron transport by the Au NPs results in substantial increase in J_{sc}, FF and η. Demonstrating that this composite systems based in CdSe QDs, Au NPs, P3OT, and TiO_2 NCs is promising for photovoltaic an optoelectronic applications by optimizing the quality and configuration of the components of the devices.

In the case of PbS/CdS/ZnS SILAR sensitized TiO_2 films, it was found that the configurations with better performance is the one that has 3 deposits of TiO_2 compact layer, 4 of the transparent layer and 2 of the scattering layer, and is decorated with 1 cycle of PbS, 6 cycles of CdS and 2 cycles of CdS (η = 3.5%). IPCE analysis indicates that such efficiency is due to a high QE in the infrared region that results in high photocurrent. When PbS QDs are deposited by electrophoresis, the optimal conditions are reached with 60 min of EP deposit, 5 SILAR cycles of CdS and 2 cycles of ZnS (η = 3.75%). In this case, the efficiency is due to a small increment in the QE in the green to red region that increases the photocurrent. In comparison whit SILAR deposited PbS EP deposited PbS produce less photocurrent, but maintains a higher FF, resulting in a better cell performance.

In the studies for alternative photovoltaic applications, a tandem device based in a CdS SILAR sensitized TiO_2 film conected in series with a ruthenium based DSSC was developed. The DSSC considerably improves the unassisted solar to hydrogen conversion efficiency of the CdS sensitized films. The obtained STH (4.1%) is one of the highest reported for this kind of heterostructured systems.

Photovoltaic materials is a very rich research field, that needs knowledge in many different areas such as optics, photonics, quantum physics, soft chemistry, electrochemistry and electronics. It could be studied from the point of view of any or these areas; actually, research is normally done from more than one area at the same time. This research field has a lot of parameters and variables that could be

explored and that are strongly correlated. Then, every single material of study, each morphology and each device configuration will have a unique set of parameters that will give the best photovoltaic performance. That is the reason why the study of these parameters could provide not only a person but a large group of scientists all over the world, a life of very exiting research obtaining more efficient, cheaper and more durable photovoltaic devices.

As a result of this research work the next papers were written:

1. <u>Zarazúa, I.</u>, De la Rosa, E., Lopez-Luke, T., Reyes, J., & Ruiz, S. **Photovoltaic conversion enhancement of TiO$_2$ nanoparticles decorated with Au nanocrystals and sensitized with CdSe quantum dots and P3OT polymer.** In L. Tsakalakos (Ed.), (Vol. 7772, pp. 777217–777217–9). Presented at the SPIE Solar Energy + Technology, SPIE. doi:10.1117/12.861056 (2010)

2. <u>Zarazúa, I</u>., De la Rosa, E., López-Luke, T., Reyes-Gomezb, J., Ruiza, S., & Rodriguez, R. A. **Photovoltaic conversion of TiO$_2$ nanocrystals decorated with P3OT, Au nanocystal or CdSe quantum dots**. *Rev Mex Fis*, *57*, pp. 69–74. (2011)

3. <u>Zarazúa, I.</u>, De la Rosa, E., Lopez-Luke, T., Reyes-Gomez, J., Ruiz, S., Angeles Chavez, C., & Zhang, J. **Photovoltaic Conversion Enhancement of CdSe Quantum Dot-Sensitized TiO$_2$ Decorated with Au Nanoparticles and P3OT**. *The Journal of Physical Chemistry C, 115*, 23209–23220. (2011).

4. González-Pedro, V., <u>Zarazúa, I</u>., Maria Barea, E., Fabregat-Santiago, F., De la Rosa, E., Mora-Sero, I., & Giméneza, S. **High efficient solar to H$_2$ conversion by hybrid Quantum Dots Dye dual absorber tandem device**. (in revision).

5. <u>Zarazúa, I.</u> López-Luke, T. Reyes-Gómez, J. Torres-Castro, A. Zhang J. Z. and De la Rosa, E. **Impedance analysis of CdSe quantum dot-sensitized TiO₂ solar cells decorated with Au nanoparticles and P3OT** Journal Of the Electrochemical Society (accepted)

6. <u>Zarazúa, I.</u> López-Luke, González-Pedro, Mora-Sero, I. De la Rosa, E., **Efficiency Analysis of TiO₂ films sensitized with PbS/CdS/ZnS by SILAR and Electrophoresis Methods** (in process)

89

References

[1]   M.K. Hubbert, Energy from fossil fuels, Scince. 109 (1949) 103–109.

[2]   Forecasting Oil & Gas Production, Energy Files. (2010).

[3]   Energy Savings Potential of Solid-State Lighting in General Illumination Applications 2010 to 2030, 2010.

[4]   P.V. Kamat, Meeting the clean energy demand: nanostructure architectures for solar energy conversion, J. Phys. Chem. C. 111 (2007) 2834–2860.

[5]   M.A. Green, K. Emery, Y. Hishikawa, W. Warta, Solar cell efficiency tables (version 37), Prog. Photovolt: Res. Appl. 19 (2011) 84–92.

[6]   T. Soga, Nanostructured Materials for Solar Energy Conversion, Elsevier, Burlington, MA, 2007.

[7]   B. Gregg, Excitonic solar cells, J. Phys. Chem. B. 107 (2003) 4688–4698.

[8]   C.D. Lokhande, B.-O. Park, H.-S. Park, K.-D. Jung, O.-S. Joo, Electrodeposition of TiO_2 and RuO_2 thin films for morphology-dependent applications, Ultramicroscopy. 105 (2005) 267–274.

[9]   G.P. Smestad, S. Spiekermann, J. Kowalik, C.D. Grant, A.M. Schwartzberg, J. Zhang, et al., A technique to compare polythiophene solid-state dye sensitized TiO2 solar cells to liquid junction devices, Sol. Energy Mater. Sol. Cells. 76 (2003) 85–105.

[10]   B.R. Saunders, M.L. Turner, Nanoparticle–polymer photovoltaic cells, Adv. in Colloid and Interf. Science. 138 (2008) 1–23.

[11]   M.C. Scharber, D. Muhlbacher, M. Koppe, P. Denk, C. Waldauf, A.J. Heeger, et al., Design Rules for Donors in Bulk-Heterojunction Solar

Cells—Towards 10 % Energy-Conversion Efficiency, Adv. Mater. 18 (2006) 789–794.

[12] C.J. Brabec, A. Cravino, D. Meissner, N.S. Sariciftci, T. Fromherz, M.T. Rispens, et al., Origin of the Open Circuit Voltage of Plastic Solar Cells, Adv. Funct. Mater. 11 (2001) 374–380.

[13] S.W. Lee, H.J. Lee, J.H. Choi, W.G. Koh, J.M. Myoung, J.H. Hur, et al., Periodic Array of Polyelectrolyte-Gated Organic Transistors from Electrospun Poly(3-hexylthiophene) Nanofibers, Nano. Lett. 10 (2010) 347–351.

[14] W. Ma, C. Yang, X. Gong, K. Lee, A.J. Heeger, Thermally Stable, Efficient Polymer Solar Cells with Nanoscale Control of the Interpenetrating Network Morphology, Adv. Funct. Mater. 15 (2005) 1617–1622.

[15] J. Zhang, H. Zhu, S. Zheng, F. Pan, T. Wang, TiO_2 Film/Cu_2O Microgrid Heterojunction with Photocatalytic Activity under Solar Light Irradiation, App. Mat. & Interfaces. 1 (2009) 2111–2114.

[16] I. Robel, V. Subramanian, M. Kuno, P.V. Kamat, Quantum dot solar cells. Harvesting light energy with CdSe nanocrystals molecularly linked to mesoscopic TiO_2 films, J. Am. Chem. Soc. 128 (2006) 2385–2393.

[17] P.V. Kamat, Quantum Dot Solar Cells. Semiconductor Nanocrystals as Light Harvesters, J. Phys. Chem. C. 112 (2008) 18737–18753.

[18] P.V. Hal, M. Wienk, J. Kroon, W. Verhees, Photoinduced Electron Transfer and Photovoltaic Response of a MDMO-PPV: TiO_2 Bulk-Heterojunction, Adv. Mater. 15 (2003) 118–121.

[19] C.-Y. Li, T.-C. Wen, T.-H. Lee, T.-F. Guo, J.-C.-A. Huang, Y.-C. Lind, et al., An inverted polymer photovoltaic cell with increased air stability obtained by employing novel hole/electron collecting layers, J. Mater.

Chem. 19 (2009) 1643–1647.

[20] C. Goh, S. Scully, M. McGehee, Effects of molecular interface modification in hybrid organic-inorganic photovoltaic cells, J. Appl. Phys. 101 (2007) 114503.

[21] P. Hal, M. Wienk, J. Kroon, R. Janssen, TiO_2 sensitized with an oligo (p-phenylenevinylene) carboxylic acid: a new model compound for a hybrid solar cell, J. Mater. Chem. 13 (2003) 1054–1057.

[22] M. Mingkui Wang, High-Performance Liquid and Solid Dye-Sensitized Solar Cells Based on a Novel Metal-Free Organic Sensitizer, Adv. Mater. 20 (2008) 4460–4463.

[23] C. Kim, S. Lee, E. Gomez, J. Kim, Y. Loo, Transient photovoltaic behavior of air-stable, inverted organic solar cells with solution-processed electron transport layer, Appl. Phys. Lett. 94 (2009) 113302.

[24] M. Antoniadou, E. Stathatos, N. Boukos, A. Stefopoulos, Study of hybrid solar cells made of multilayer nanocrystalline titania and poly (3-octylthiophene) or poly-(3-(2-methylhex-2-yl)-oxy- carbonyldithiophene), Nanotech. 20 (2009) 495201.

[25] A. Arango, L. Johnson, V. Bliznyuk, Efficient Titanium Oxide/Conjugated Polymer Photovoltaics for Solar Energy Conversion, Adv. Mater. 12 (2000) 1689–1692.

[26] J. Luo, C. Liu, S. Yang, Y. Cao, Hybrid solar cells based on blends of poly(3-hexylthiophene) and surface dye-modified, ultrathin linear- and branched-TiO_2 nanorods, Sol. Energy Mater. Sol. Cells. 94 (2010) 501–508.

[27] A.L. Briseno, T.W. Holcombe, A.I. Boukai, E.C. Garnett, S.W. Shelton, J.J.M. Fréchet, et al., Oligo- and Polythiophene/ZnO Hybrid Nanowire Solar Cells, Nano. Lett. 10 (2010) 334–340.

[28]   A. Kongkanand, K. Tvrdy, K. Takechi, M. Kuno, P.V. Kamat, Quantum Dot Solar Cells. Tuning Photoresponse through Size and Shape Control of CdSe-TiO$_2$ Architecture, J. Am. Chem. Soc. 130 (2008) 4007–4015.

[29]   R. Beranek, H. Tsuchiya, T. Sugishima, J. Macak, L. Taveira, S. Fujimoto, et al., Enhancement and limits of the photoelectrochemical response from anodic TiO$_2$ nanotubes, Appl. Phys. Lett. 87 (2005) 243114.

[30]   G.K. Mor, K. Shankar, M. Paulose, O.K. Varghese, C.A. Grimes, Use of Highly-Ordered TiO$_2$ Nanotube

Arrays in Dye-Sensitized Solar Cells, Nano. Lett. 6 (2005) 215–218.

[31]   P. E Stathatos, Increase of the Efficiency of Quasi-Solid State Dye-Sensitized Solar Cells by a Synergy between Titania Nanocrystallites of Two Distinct Nanoparticle Sizes, Adv. Mater. 19 (2007) 3338–3341.

[32]   T. Chou, Q. Zhang, B. Russo, Titania Particle Size Effect on the Overall Performance of Dye-Sensitized Solar Cells, J. Phys. Chem. C. 111 (2007) 6296–6302.

[33]   J. Nelson, The physics of solar cells, Imperial college press, 2003.

[34]   M. Shur, Physics Of Semiconductor Devices (Rev.), Prentice Hall International, 1990.

[35]   C.D. Grant, A.M. Schwartzberg, G.P. Smestad, J. Kowalik, L.M. Tolbert, J.Z. Zhang, Optical and electrochemical characterization of poly(3-undecyl-2,2′-bithiophene) in thin film solid state TiO2 photovoltaic solar cells, Synthetic Metals. 132 (2003) 197–204.

[36]   P. Liska, K. Thampi, M. Gratzel, Nanocrystalline dye-sensitized solar cell/copper indium gallium selenide thin-film tandem showing greater than 15% conversion efficiency, Appl. Phys. Lett. 88 (2009) 203103.

[37]   L. Han, N. Koide, Y. Chiba, A. Islam, R. Komiya, Improvement of efficiency of dye-sensitized solar cells by reduction

of internal resistance, Appl. Phys. Lett. 86 (2005) 213501.

[38]   I. Mora-Seró, T. Dittrich, A. Susha, A. Rogach, J. Bisquert, Large improvement of electron extraction from CdSe quantum dots into a TiO_2 thin layer by N3 dye coabsorption, Thin Solid Films. 516 (2008) 6994–6998.

[39]   Y. Chiba, A. Islam, Y. Watanabe, R. Komiya, Dye-sensitized solar cells with conversion efficiency of 11.1 \%, J. J. Appl. Phys. 45 (2006) L638–L640.

[40]   C. Xu, P. Shin, L. Cao, D. Gao, Preferential Growth of Long ZnO Nanowire Array and Its Application in Dye-Sensitized

Solar Cells, J. Phys. Chem. C. 114 (2010) 125–129.

[41]   A. Mihi, F. Lopez-Alcaraz, H. Miguez, Full spectrum enhancement of the light harvesting efficiency of dye sensitized solar cells by including colloidal photonic crystal multilayers, Appl. Phys. Lett. 88 (2006) 193110.

[42]   A. Yella, H.W. Lee, H.N. Tsao, C. Yi, A.K. Chandiran, M.K. Nazeeruddin, et al., Porphyrin-Sensitized Solar Cells with Cobalt (II/III)-Based Redox Electrolyte Exceed 12 Percent Efficiency, Scince. 334 (2011) 629–634.

[43]   K. Hara, T. Horiguchi, T. Kinoshita, K. Sayama, Highly efficient photon-to-electron conversion with mercurochrome-sensitized nanoporous oxide semiconductor solar cells, Sol. Energy Mater. Sol. Cells. 64 (2000) 115–134.

[44]   T. Lopez-Luke, A. Wolcott, L. Xu, S. Chen, Z. Wen, J. Li, et al., Nitrogen-doped and CdSe quantum-dot-sensitized nanocrystalline TiO_2 films for solar energy conversion applications, J. Phys. Chem. C. 112 (2008)

1282–1292.

[45]   M. Sykora, M.A. Petruska, J. Alstrum-Acevedo, I. Bezel, T.J. Meyer, V.I. Klimov, Photoinduced Charge Transfer between CdSe Nanocrystal Quantum Dots and Ru-Polypyridine Complexes, J. Am. Chem. Soc. 128 (2006) 9984–9985.

[46]   T. Zeng, S. Liu, F. Hsu, K. Huang, H. Liao, Effects of bifunctional linker on the performance of P3HT/CdSe quantum dot-linker-ZnO nanocolumn photovoltaic device, Opt. Express. 18 (2010) 130137.

[47]   A. Franceschetti, J. An, A. Zunger, Impact ionization can explain carrier multiplication in PbSe quantum dots, Nano. Lett. 6 (2006) 2191–2195.

[48]   R. Loef, A.J. Houtepen, E. Talgorn, J. Schoonman, A. Goossens, Study of Electronic Defects in CdSe Quantum Dots and Their Involvement in Quantum Dot Solar Cells, Nano. Lett. 9 (2009) 956–859.

[49]   N. Guijarro, T. Lana-Villarreal, I. Mora-Sero, J. Bisquert, R. Gomez, CdSe Quantum Dot-Sensitized TiO_2 Electrodes: Effect of Quantum Dot Coverage and Mode of Attachment, J. Phys. Chem. C. 113 (2009) 4208–4214.

[50]   C. Wang, M. Shim, P. Guyot-Sionnest, Electrochromic nanocrystal quantum dots, Scince. 291 (2001) 2390–2392.

[51]   M. Grätzel, Photoelectrochemical cells, Nature. 414 (2001).

[52]   M. Sathish, B. Viswanathan, R.P. Viswanath, C.S. Gopinath, Synthesis, characterization, electronic structure, and photocatalytic activity of nitrogen-doped TiO_2 nanocatalyst, Chem. Mater. 17 (2005) 6349–6353.

[53]   R. Beraneka, B. Neumannb, S. Sakthivela, M. Janczarekc, T. Dittrichb, H. Tributschb, et al., Exploring the electronic structure of nitrogen-modified TiO_2 photocatalysts through photocurrent and surface photovoltage

studies, Chem. Phys. 339 (2007) 11–19.

[54]   N. Greenham, X. Peng, A. Alivisatos, Charge separation and transport in conjugated-polymer/semiconductor-nanocrystal composites studied by photoluminescence quenching and photoconductivity, Phys. Rev. B. 54 (1996) 17628–17637.

[55]   Z. Zheng, L. Zhao, M. Wang, M. Liu, M.S. Marcus, Y. Liu, High efficiency CdSe quantum-dot sensitized solar cells, Photovoltaic Specialist Conference (PVSC). (2010) 000461–000466.

[56]   L. Zeng, C.W. Tang, S.H. Chen, Effects of active layer thickness and thermal annealing on polythiophene: Fullerene bulk heterojunction photovoltaic devices, Appl. Phys. Lett. 97 (2010) 053305–053305–3.

[57]   M. Svensson, F. Zhang, S.C. Veenstra, W.J.H. Verhees, J.C. Hummelen, J.M. Kroon, et al., High-Performance Polymer Solar Cells of an Alternating Polyfluorene Copolymer and a Fullerene Derivative, Adv. Mater. 15 (2003) 988–991.

[58]   J. Peet, J.Y. Kim, N.E. Coates, W.L. Ma, D. Moses, A.J.H.G.C. Bazan, Efficiency enhancement in low-bandgap polymer solar cells by processing with alkane dithiols, Nature Mater. 6 (2007) 497–500.

[59]   A. Ballantyne, L. Chen, J. Nelson, D. Bradley, Y. Astuti, A. Maurano, et al., Studies of Highly Regioregular Poly (3-hexylselenophene) for Photovoltaic Applications, Adv. Mater. 19 (2007) 4544–4547.

[60]   M. Campoy-Quiles, T. Ferenczi, T. Agostinelli, P.G. Etchegoin, Y. Kim, T.D. Anthopoulos, et al., Morphology evolution via self-organization and lateral and vertical diffusion in polymer:fullerene solar cell blends, Nature Mater. 7 (2008) 158–164.

[61]   S. Günes, H. Neugebauer, N.S. Sariciftci, Conjugated Polymer-Based Organic Solar Cells, Chem. Rev. 107 (2007) 1324–1338.

[62]   G. Li, V. Shrotriya, J. Huang, Y. Yao, T. Moriarty, K. Emery, et al., High-efficiency solution processable polymer photovoltaic cells by self-organization of polymer blends, Nature Mater. 4 (2005) 864–868.

[63]   W.U. Huynh, Hybrid Nanorod-Polymer Solar Cells, Scince. 295 (2002) 2425–2427.

[64]   L. Liu, G. Wang, Y. Li, Y. Li, J.Z. Zhang, CdSe quantum dot-sensitized Au/TiO$_2$ hybrid mesoporous films and their enhanced photoelectrochemical performance, Nano Research. (2011) 1–10.

[65]   Y. Nakato, M. Shioji, Photoeffects on the potentials of thin metal films on a n-TiO2 crystal wafer. The mechanism of semiconductor photocatalysts, Chem. Phys. Lett. (1982).

[66]   G. Zhao, H. Kozuka, T. Yoko, Photoelectrochemical properties of dye-sensitized TiO2 films containing dispersed gold metal particles prepared by sol-gel method, Nippon Seramikkusu Kyokai Gakujutsu Ronbunshi. 104 (1996) 164–168.

[67]   N. Chandrasekharan, P.V. Kamat, Improving the Photoelectrochemical Performance of Nanostructured TiO$_2$ Films by Adsorption of Gold Nanoparticles†, J. Phys. Chem. B. 104 (2000) 10851.

[68]   Y. Tian, T. Tatsuma, Mechanisms and Applications of Plasmon-Induced Charge Separation at TiO$_2$ Films Loaded with Gold Nanoparticles, J. Am. Chem. Soc. 127 (2005) 7632–7637.

[69]   P.V. Kamat, Semiconductor− Metal Nanocomposites. Photoinduced Fusion and Photocatalysis of Gold-Capped TiO$_2$ (TiO$_2$/Gold) Nanoparticles, J. Phys. Chem. B. (2001).

[70]   V. Subramanian, E. Wolf, P.V. Kamat, Semiconductor-Metal Composite Nanostructures. To What Extent Do Metal Nanoparticles Improve the

Photocatalytic Activity of TiO$_2$ Films? J. Phys. Chem. B. 105 (2001) 11439–11446.

[71]   G. Burgeth, H. Kisch, Photocatalytic and photoelectrochemical properties of titania–chloroplatinate(IV), Coordination Chemistry Reviews. 230 (2002) 41–47.

[72]   Y. Tian, Plasmon-Induced Photoelectrochemistry at Metal Nanoparticles Supported on Nanoporous TiO$_2$ W, Chem. Comm. (2004).

[73]   D.M. Schaadt, B. Feng, E.T. Yu, Enhanced semiconductor optical absorption via surface plasmon excitation in metal nanoparticles, Appl. Phys. Lett. 86 (2005) 063106–063106–3.

[74]   S. Pillai, K.R. Catchpole, T. Trupke, G. Zhang, J. Zhao, M.A. Green, Enhanced emission from Si-based light-emitting diodes using surface plasmons, Appl. Phys. Lett. 88 (2006) 161102.

[75]   D. Derkacs, S. Lim, P. Matheu, W. Mar, Improved performance of amorphous silicon solar cells via scattering from surface plasmon polaritons in nearby metallic nanoparticles, Appl. Phys. Lett. (2006).

[76]   S. Pillai, K. Catchpole, T. Trupke, Surface plasmon enhanced silicon solar cells, J. Appl. Phys. (2007).

[77]   H.R. Stuart, D.G. Hall, Island size effects in nanoparticle-enhanced photodetectors, Appl. Phys. Lett. 73 (1998) 3815–3817.

[78]   Y. Nishijima, K. Ueno, Y. Yokota, Plasmon-Assisted Photocurrent Generation from Visible to Near-Infrared Wavelength Using a Au-Nanorods/TiO$_2$ Electrode, J. Phys. Chem. Lett. (2010).

[79]   I. Zarazúa, E. De La Rosa, T. López-Luke, J. Reyes-Gomezb, S. Ruiza, R.A. Rodriguez, Photovoltaic conversion of TiO$_2$ nanocrystals decorated with P3OT, Au nanocystal or CdSe quantum dots, Revista Méxicana De

Física. 57 (2011) 69–74.

[80]   Y. Djaoued, R. Brüning, D. Bersani, P.P. Lottici, S. Badilescu, Sol–gel
        nanocrystalline brookite-rich titania films, Materials Letters. 58 (2004)
        2618–2622.

[81]   J. Pérez-Juste, L.M. Liz-Marzán, S. Carnie, D.Y.C. Chan, P. Mulvaney,
        Electric-Field-Directed Growth of Gold Nanorods in Aqueous Surfactant
        Solutions, Adv. Funct. Mater. 14 (2004) 571–579.

[82]   H. Wang, D. He, Y. Wang, Z. Liu, H. Wu, J. Wang, Organic photovoltaic
        devices based on graphene as an electron-acceptor material and P3OT
        as a donor material, Phys. Status Solidi A. 208 (2011) 2339–2343.

[83]   T.Z. Markus, S. Itzhakov, Y.I. Alkotzer, D. Cahen, G. Hodes, D. Oron, et
        al., Energetics of CdSe Quantum Dots Adsorbed on TiO 2, J. Phys.
        Chem. C. 115 (2011) 13236–13241.

[84]   B. O'regan, M. Grätzel, A low-cost, high-efficiency solar cell based on
        dye-sensitized colloidal Ti02 films, Nature. 353 (1991) 737–740.

[85]   I. Mora-Sero, S. Giménez, F. Fabregat-Santiago, R. Gomez, Q. Shen, T.
        Toyoda, et al., Recombination in Quantum Dot Sensitized Solar Cells,
        Acc. Chem. Res. 42 (2009) 1848–1857.

[86]   M. Jung, Enhanced photo-conversion efficiency of CdSe–ZnS core–shell
        quantum dots with Au nanoparticles on TiO_2 electrodes, J. Mater. Chem.
        (2010).

[87]   J. Ondersma, T. Hamann, Impedance Investigation of Dye-Sensitized
        Solar Cells Employing Outer-Sphere Redox Shuttles, J. Phys. Chem. C.
        114 (2009) 638–645.

[88]   F. Fabregat-Santiago, G. Garcia-Belmonte, J. Bisquert, A. Zaban, P.
        Salvador, Decoupling of Transport, Charge Storage, and Interfacial

Charge Transfer in the Nanocrystalline TiO 2/Electrolyte System by Impedance Methods, J. Phys. Chem. B. 106 (2002) 334–339.

[89]   F. Fabregat-Santiago, J. Bisquert, G. Garcia-Belmonte, G. Boschloo, A. Hagfeldt, Influence of electrolyte in transport and recombination in dye-sensitized solar cells studied by impedance spectroscopy, Sol. Energy Mater. Sol. Cells. 87 (2005) 117–131.

[90]   P.P. Boix, G. Larramona, A. Jacob, B. Delatouche, I. Mora-Sero, J. Bisquert, Hole Transport and Recombination in All-Solid Sb 2S 3-Sensitized TiO 2Solar Cells Using CuSCN As Hole Transporter, J. Phys. Chem. C. 116 (2012) 1579–1587.

[91]   C. He, Z. Zheng, H. Tang, L. Zhao, Electrochemical impedance spectroscopy characterization of electron transport and recombination in ZnO nanorod dye-sensitized solar cells, J. Phys. Chem. C. 113 (2009) 10322–10325.

[92]   Y.Y. Proskuryakov, K. Durose, M.K. Al Turkestani, I. Mora-Seró, G. Garcia-Belmonte, F. Fabregat-Santiago, et al., Impedance spectroscopy of thin-film CdTe/CdS solar cells under varied illumination, J. Appl. Phys. 106 (2009) 044507.

[93]   I. Mora-Sero, Y. Luo, G. Garcia-Belmonte, J. Bisquert, D. Muñoz, C. Voz, et al., Recombination rates in heterojunction silicon solar cells analyzed by impedance spectroscopy at forward bias and under illumination, Sol. Energy Mater. Sol. Cells. 92 (2008) 505–509.

[94]   P. de Jongh, D. Vanmaekelbergh, Trap-Limited Electronic Transport in Assemblies of Nanometer-Size TiO2 Particles, Phys. Rev. Lett. 77 (1996) 3427–3430.

[95]   J. Nelson, Continuous-time random-walk model of electron transport in nanocrystalline TiO2 electrodes, Phys. Rev. B. 59 (1999) 15374–15380.

[96]   R. Könenkamp, Carrier transport in nanoporous TiO2 films, Phys. Rev. B. 61 (2000) 11057–11064.

[97]   J. van de Lagemaat, A.J. Frank, Effect of the Surface-State Distribution on Electron Transport in Dye-Sensitized TiO 2Solar Cells: Nonlinear Electron-Transport Kinetics, J. Phys. Chem. B. 104 (2000) 4292–4294.

[98]   A.C. Fisher, L.M. Peter, E.A. Ponomarev, A.B. Walker, K.G.U. Wijayantha, Intensity Dependence of the Back Reaction and Transport of Electrons in Dye-Sensitized Nanocrystalline TiO 2Solar Cells, J. Phys. Chem. B. 104 (2000) 949–958.

[99]   G. Franco, J. Gehring, L.M. Peter, E.A. Ponomarev, I. Uhlendorf, Frequency-Resolved Optical Detection of Photoinjected Electrons in Dye-Sensitized Nanocrystalline Photovoltaic Cells, J. Phys. Chem. B. 103 (1999) 692–698.

[100]   L. Han, N. Koide, Y. Chiba, T. Mitate, Modeling of an equivalent circuit for dye-sensitized solar cells, Appl. Phys. Lett. 84 (2004) 2433.

[101]   R. Kern, R. Sastrawan, J. Ferber, R. Stangl, J. Luther, Modeling and interpretation of electrical impedance spectra of dye solar cells operated under open-circuit conditions, Electrochimica Acta. 47 (2002) 4213–4225.

[102]   A. Hauch, A. Georg, Diffusion in the electrolyte and charge-transfer reaction at the platinum electrode in dye-sensitized solar cells, Electrochimica Acta. 46 (2001) 3457–3466.

[103]   G. Schlichthörl, S.Y. Huang, J. Sprague, A.J. Frank, Band edge movement and recombination kinetics in dye-sensitized nanocrystalline TiO2 solar cells: a study by intensity modulated photovoltage spectroscopy, The Journal of Physical Chemistry B. 101 (1997) 8141–8155.

[104]   I. Zarazúa, E. De La Rosa, T. Lopez-Luke, J. Reyes-Gomez, S. Ruiz, C.

Angeles Chavez, et al., Photovoltaic Conversion Enhancement of CdSe Quantum Dot-Sensitized TiO$_2$ Decorated with Au Nanoparticles and P3OT, J. Phys. Chem. C. 115 (2011) 23209–23220.

[105] M.C. Arenas, N. Mendoza, H. Cortina, M.E. Nicho, H. Hu, Influence of poly3-octylthiophene (P3OT) film thickness and preparation method on photovoltaic performance of hybrid ITO/CdS/P3OT/Au solar cells, Sol. Energy Mater. Sol. Cells. 94 (2009) 29–33.

[106] J. van de Lagemaat, N.G. Park, A.J. Frank, Influence of electrical potential distribution, charge transport, and recombination on the photopotential and photocurrent conversion efficiency of dye-sensitized nanocrystalline TiO2 solar cells: a study by electrical impedance and optical modulation techniques, The Journal of Physical Chemistry B. 104 (2000) 2044–2052.

[107] M.K. Hubbert, The world's evolving energy system, American Journal of Physics. 49 (1981) 1007–1029.

[108] N. Parsi Benehkohal, V. González-Pedro, P.P. Boix, S. Chavhan, R. Tena-Zaera, G.P. Demopoulos, et al., Colloidal PbS and PbSeS Quantum Dot Sensitized Solar Cells Prepared by Electrophoretic Deposition, J. Phys. Chem. C. 116 (2012) 16391–16397.

[109] H.K. Jun, M.A. Careem, A.K. Arof, A Suitable Polysulfide Electrolyte for CdSe Quantum Dot-Sensitized Solar Cells, International Journal of Photoenergy. 2013 (2013) 1–10.

[110] V. González-Pedro, C. Sima, G. Marzari, P.P. Boix, S. Giménez, Q. Shen, et al., High performance PbS Quantum Dot Sensitized Solar Cells exceeding 4% efficiency: the role of metal precursors in the electron injection and charge separation, Phys. Chem. Chem. Phys. 15 (2013) 13835.

[111]   A. Braga, S. Giménez, I. Concina, A. Vomiero, I. Mora-Sero, Panchromatic Sensitized Solar Cells Based on Metal Sulfide Quantum Dots Grown Directly on Nanostructured TiO_2 Electrodes, J. Phys. Chem. Lett. 2 (2011) 454–460.

[112]   J. Barber, Photosynthetic energy conversion: natural and artificial, Chem. Soc. Rev. 38 (2008) 185–196.

[113]   D. Gust, T.A. Moore, A.L. Moore, Solar Fuels via Artificial Photosynthesis, Acc. Chem. Res. 42 (2009) 1890–1898.

[114]   X. Chen, S. Shen, L. Guo, S.S. Mao, Semiconductor-based Photocatalytic Hydrogen Generation, Chem. Rev. 110 (2010) 6503–6570.

[115]   A.J. Bard, M.A. Fox, Artificial Photosynthesis: Solar Splitting of Water to Hydrogen and Oxygen, Acc. Chem. Res. 28 (1995) 141–145.

[116]   N.S. Lewis, Light work with water, Nature. 414 (2001) 589–590.

[117]   S.Y. Reece, J.A. Hamel, K. Sung, T.D. Jarvi, A.J. Esswein, J.J.H. Pijpers, et al., Wireless Solar Water Splitting Using Silicon-Based Semiconductors and Earth-Abundant Catalysts, Scince. 334 (2011) 645–648.

[118]   R.E. Rocheleau, E.L. Miller, A. Misra, High-Efficiency Photoelectrochemical Hydrogen Production Using Multijunction Amorphous Silicon Photoelectrodes, Energy Fuels. 12 (1998) 3–10.

[119]   M.F. Weber, M.J. Dignam, Efficiency of Splitting Water with Semiconducting Photoelectrodes, J. Electrochem. Soc. 131 (1984) 1258.

[120]   M. WEBER, M. DIGNAM, Splitting water with semiconducting photoelectrodes—Efficiency considerations, International Journal of Hydrogen Energy. 11 (1986) 225–232.

[121]   O. Khaselev, A Monolithic Photovoltaic-Photoelectrochemical Device for

Hydrogen Production via Water Splitting, Scince. 280 (1998) 425–427.

[122] R. van de Krol, Y. Liang, J. Schoonman, Solar hydrogen production with nanostructured metal oxides, J. Mater. Chem. 18 (2008) 2311.

[123] S. Caramori, V. Cristino, R. Argazzi, L. Meda, C.A. Bignozzi, Photoelectrochemical Behavior of Sensitized TiO2 Photoanodes in an Aqueous Environment: Application to Hydrogen Production, Inorg. Chem. 49 (2010) 3320–3328.

[124] W.J. Youngblood, S.-H.A. Lee, K. Maeda, T.E. Mallouk, Visible Light Water Splitting Using Dye-Sensitized Oxide Semiconductors, Acc. Chem. Res. 42 (2009) 1966–1973.

[125] J. Hensel, G. Wang, Y. Li, J.Z. Zhang, Synergistic Effect of CdSe Quantum Dot Sensitization and Nitrogen Doping of TiO 2Nanostructures for Photoelectrochemical Solar Hydrogen Generation, Nano. Lett. 10 (2010) 478–483.

[126] Y. Jin-nouchi, T. Akita, H. Tada, Ultrafast Photodeposition of Size-Controlled PbS Quantum Dots on TiO2, Chem. Eur. J. of Chem. Phys. 11 (2010) 2349–2352.

[127] P. Rodenas, T. Song, P. Sudhagar, G. Marzari, H. Han, L. Badia-Bou, et al., Quantum Dot Based Heterostructures for Unassisted Photoelectrochemical Hydrogen Generation, Adv. Energy Mater. 3 (2012) 176–182.

[128] R. Trevisan, P. Rodenas, V. González-Pedro, C. Sima, R.S. Sanchez, E.M. Barea, et al., Harnessing Infrared Photons for Photoelectrochemical Hydrogen Generation. A PbS Quantum Dot Based "Quasi-Artificial Leaf," J. Phys. Chem. Lett. 4 (2013) 141–146.

[129] J. Luo, S.K. Karuturi, L. Liu, L.T. Su, A.I.Y. Tok, H.J. Fan, Homogeneous Photosensitization of Complex TiO2 Nanostructures for Efficient Solar

Energy Conversion, Sci. Rep. 2 (2012) –.

[130]   V. González-Pedro, I. Zarazúa, E. Maria Barea, F. Fabregat-Santiago, E. De la Rosa, I. Mora-Sero, et al., High efficient solar to H_2 conversion by hybrid Quantum Dots Dye dual absorber tandem device, Chem. Comm. (2013) 1–16.

[131]   Z. Chen, T.F. Jaramillo, T.G. Deutsch, A. Kleiman-Shwarsctein, A.J. Forman, N. Gaillard, et al., Accelerating materials development for photoelectrochemical hydrogen production: Standards for methods, definitions, and reporting protocols, J. Mater. Res. 25 (2011) 3–16.

Appendix A. Snapshots of the CdS QDs film/DSSC tandem device during the H_2 Production and storage in an inverted burette.